

Assessing the Potential of Intervening MgII Absorbers for Cosmology

Alexia M Lopez

A THESIS SUBMITTED IN PARTIAL FULFILMENT
OF THE REQUIREMENTS FOR THE DEGREE OF
MASTER OF SCIENCE

Jeremiah Horrocks Institute for Maths, Physics and Astronomy
University of Central Lancashire

November 2019

Declaration

The work presented in this thesis was carried out at the Jeremiah Horrocks Institute for Maths, Physics and Astronomy, University of Central Lancashire.

I declare that while registered as a candidate for the research degree, I have not been a registered candidate or enrolled student for another award of the University or other academic or professional institution.

I declare that no material contained in the thesis has been used in any other submission for an academic award. Data and models used in this thesis that are not my own are clearly cited in the text.

Abstract

In this thesis I present a method of using intervening MgII absorbers as a way to probe the large scale structure (LSS) of the universe. In addition, I discuss the uses of intervening MgII absorbers as a tool for cosmology.

Due to the large amounts of telescope time required to observe faint and distant galaxies, it becomes increasingly difficult to map the LSS of the universe at high redshifts. With the intervening MgII method presented here it is possible, with an independent method, to map the LSS of the universe and begin to understand the early stages of formation and evolution of the LSS of the universe.

I use six known examples of high redshift structures to assess whether intervening MgII absorbers can highlight the LSS. In five of the six target fields, there are detections of dense regions of MgII absorbers which are believed to be in association with the target structures, while the sixth target remains less clear due to low completeness. In one particular case, a long, thin, dense arc of absorbers is found extending up to 1 Gpc at $z \sim 0.8$. A structure of such size could potentially challenge the standard model of cosmology. In addition, further similar structures may exist, awaiting to be detected with the MgII method presented here. For the final target, I use the MgII method to refine the redshift measurement of a known chain of galaxy clusters in association with a large quasar group.

The aim of this thesis was to assess the potential of using intervening MgII absorbers as a tool for cosmology and LSS. The conclusion is this new method does indeed have considerable potential for cosmological investigations.

Contents

Declaration	ii
Abstract	iii
Acknowledgements	xii
List of Abbreviations	xiv
1 Introduction	1
2 MgII Absorbers	4
2.1 Absorption Lines	7
2.2 Equivalent Width	10
2.3 Cosmological Applications of MgII	14
3 Method: Constructing MgII Images	16
3.1 Sloan Digital Sky Survey	16
3.2 Night Sky Lines	18
3.3 The Databases	28
3.4 The Software	39
3.4.1 Bootstrapping	43
3.5 Cluster and Supercluster Candidates	45

4	MgII Analysis for Known High z Structures	47
4.1	Target 1: COSMOS field at $z = 1.12$	53
4.2	Target 2: COSMOS field at $z = 1.27$	60
4.3	Target 3: Supercluster at $z = 0.9$	73
4.4	Target 4: Lynx Field at $z = 1.26$	87
4.5	Target 5: SZ Cluster at $z = 0.763$	102
4.6	Target 6: Galaxy Cluster associated with LQG at $z = 1.1$	123
5	Discussion	135

List of Tables

3.1	Main instrumental differences between SDSS I-II and SDSS III. . . .	17
3.2	Table of databases used in the software.	29
3.3	Total number of QSOs in the object databases.	30
3.4	The percentage split of classes of equivalent widths in the different MgII databases.	30
3.5	Number of duplicate absorbers in the paired databases.	31
3.6	The six cluster candidates selected for MgII analysis.	46
4.1	Table of information on the two S12 supercluster candidates investi- gated.	53
4.2	Summary of the five data sets used for the spectroscopic analysis on Cl 1604.	77
4.3	Table of information for the telescopes and instruments used in ob- taining optical information on the B18 cluster candidates.	103
4.4	Statistical comparisons of the whole field and rectangular selection of absorbers in the field containing the Giant Arc.	122
4.5	Number of red galaxies and expected number of star-forming blue galaxies of each of the identified galaxy clusters in T01.	128

List of Figures

1	Snowy proofreading my thesis.	xiii
2.1	QSO intervening with mass along the LOS.	5
2.2	Typical QSO spectrum with the MgII doublet feature labelled.	5
2.3	The natural line width of a spectral line.	8
2.4	The 3s orbital and the two states of the 3p orbitals in MgII.	10
2.5	Equivalent width compared with the absorption line.	11
2.6	The curve of growth of the energy in a spectral line.	12
2.7	Classes of absorbers with radial distance from the centre of a galaxy.	13
3.1	Zenith sky brightness at the Mount Hopkins observatory in 1998 and the Kitt Peak observatory in 1999.	20
3.2	Number of MgII absorbers across redshift in the Z&M DR7 and DR12 MgII databases.	23
3.3	Number of MgII absorbers across redshift in the R16 DR7 and DR12 MgII databases.	24
3.4	Completeness in the Z&M DR7 database.	25
3.5	MgII counts in the R16 DR12 database as a function of wavelength.	27
3.6	Database comparisons – R-dr7.	32
3.7	Database comparisons – R-dr12.	32
3.8	Database comparisons – ZM-dr7.	33
3.9	Database comparisons – ZM-dr12.	33

3.10 Database comparisons – R-comb.	34
3.11 Database comparisons – ZM-comb.	34
3.12 Database comparisons – R-field-all.	35
3.13 Database comparisons – ZM-field-all.	35
3.14 QSO distribution across the whole sky in the Z&M databases.	36
3.15 QSO distribution across the whole sky in R16 databases.	36
3.16 Comparison of MgII absorption plots produced from the old and new script.	38
4.1 Distribution of I-band coverage as a function of redshift.	48
4.2 Redshift distribution of the groups and clusters in S12.	50
4.3 Richness distribution of the groups and clusters throughout redshift in S12.	51
4.4 Contour map of the density distribution of member galaxies in S12.	52
4.5 MgII images centred on the COSMOS field in the redshift interval $z = 1.12 \pm 0.1$ created using ZM-comb.	55
4.6 The throughput of the red and blue spectrographs used in the Legacy Survey (DR7)	56
4.7 MgII images centred on the COSMOS field in the redshift interval $z = 1.12 \pm 0.06$	58
4.8 MgII images centred on the COSMOS field in the redshift interval $z = 1.12 \pm 0.1$ created using ZM-comb.	59
4.9 Histograms of the number of absorbers in redshift for the MgII image centred on the COSMOS field at $z = 1.27 \pm 0.08$ in the ZM-comb database.	61
4.10 The redshift distribution of MgII absorbers in each of the five ran- domly selected fields in the redshift interval $z = 1.27 \pm 0.08$	63
4.11 Supercluster candidate at $z = 1.27$ from S12.	64

4.12	MgII images centred on the COSMOS field in the redshift interval $z = 1.27 \pm 0.08$	66
4.13	MgII images centred on the COSMOS field in the redshift interval $z = 1.27 \pm 0.08$ with north and south offset values adjusted.	67
4.14	TOPCAT plot of the absorbers in the MgII field from Figure 4.13.	68
4.15	Histogram of the number of absorbers as a function of redshift for the MgII image centred on the COSMOS field at $z = 1.27 \pm 0.08$ in the ZM-comb database (from Figure 4.13.	70
4.16	Number 59 of the shuffled plots.	72
4.17	Density map of the colour-selected member galaxies of Cl 1604 in G08.	76
4.18	Face-on view of Cl 1604 taken from G08.	79
4.19	Side-on view of Cl 1604 taken from G08.	80
4.20	MgII image centred on Cluster C from G08 at redshift $z = 0.9 \pm 0.1$ produced using the ZM-comb database.	81
4.21	MgII images centred on Cluster C from G08 at redshift $z = 0.9 \pm 0.053$	83
4.22	Very strong MgII absorbers ($W_\lambda > 1.0$ for the $\lambda\lambda 2796$ line) in the field centred on Cluster C from G08 at redshift $z = 0.9 \pm 0.053$	84
4.23	MgII images centred on Cluster C from G08 at redshift $z = 0.9 \pm$ 0.053 , produced using the ZM-field-all database.	85
4.24	The distribution of the X-ray sources, QSOs and galaxies relative to the two known clusters from O-03.	90
4.25	Distribution of the red and blue galaxy candidates in the Lynx field containing the two known clusters labelled c11 and c12 from N05.	92
4.26	MgII absorbers in the field centred on the Lynx field at the midpoint between the two known clusters at redshift $z = 1.27 \pm 0.1$ using ZM- comb.	94

4.27	Density image of the available background probes in the MgII field centred on the Lynx field at redshift $z = 1.27$	96
4.28	MgII absorbers in the field centred on the Lynx field at the midpoint between the two known clusters at redshift $z = 1.27 \pm 0.08$ in ZM-comb.	97
4.29	MgII absorbers with equivalent width $W_\lambda \geq 0.3$ in the field centred on the Lynx field at the midpoint between the two known clusters at redshift $z = 1.27 \pm 0.08$	99
4.30	MgII absorbers with equivalent width $W_\lambda \geq 1.0$ in the field centred on the Lynx field at the midpoint between the two known clusters at redshift $z = 1.27 \pm 0.08$	101
4.31	WISE and optical images of the B18 cluster candidate G069.39+68.05 at redshift $z = 0.763$	104
4.32	Spectra of the brightest galaxy in the B18 cluster candidate PSZ2 G069.39+68.05.	105
4.33	Optical image of the B18 cluster candidate.	106
4.34	MgII images centred on the B18 cluster candidate created using ZM-comb.	107
4.35	MgII images centred on the B18 cluster candidate at various redshifts created using ZM-comb.	109
4.36	MgII images centred on the Giant Arc in the redshift interval $z = 0.812 \pm 0.049$ created using ZM-comb.	110
4.37	MgII image centred on the Giant Arc in the redshift interval $z = 0.812 \pm 0.049$ created using ZM-field-all.	112
4.38	MgII images centred on the Giant Arc, in a FOV with double the usual RA and Dec offsets.	114
4.39	Strong MgII absorbers ($W_\lambda > 0.6$) centred on the Giant Arc	115

4.40	Histogram of the frequency of absorbers across tp-y coordinates in the field centred on the Giant Arc.	117
4.41	Histogram of the frequency of available background probes across tp-y coordinates in the field centred on the Giant Arc.	119
4.42	TOPCAT image of the MgII absorbers in the field containing the Giant Arc with a visual selection of the MgII absorbers in the Giant Arc.	120
4.43	TOPCAT image of the MgII absorbers in the field containing the Giant Arc with a rectangular box selection around the MgII absorbers in the Giant Arc.	121
4.44	Projection of the 23 QSOs on the sky from C89.	125
4.45	Field 1338+27 with a small rectangle encompassing the selection of five QSOs that are investigated in T01.	126
4.46	Position of the galaxies in scan region A from T01 and the contour map of the density amplitude in the scan region.	127
4.47	MgII image centred on the T01 galaxy clusters in the redshift interval $z = 1.1 \pm 0.1$ created using ZM-comb.	130
4.48	MgII images centred on the T01 galaxy clusters in various redshift intervals created using ZM-comb.	132
4.49	MgII images centred on the T01 galaxy clusters in a smaller redshift range.	133

Acknowledgements

I remember being just weeks from becoming a University graduate. For many of us this is exciting, for others, terrifying; I was in the latter category. I found my passion for cosmology in my final year of University when I worked under the supervision of Dr Roger Clowes, on a literature review project of the alternative theories to the Standard Model of Cosmology. The terrifying part of graduating, in my opinion, is discovering exactly what you want to do, but not knowing whether you have that capability. Therefore, I would like to give my first thanks to Dr Roger Clowes, for believing in me as an aspiring cosmologist, and for his constant encouragement, wisdom and kind words. In addition, Dr Roger Clowes has been a dedicated supervisor and his advice and guidance throughout this year has been truly appreciated. I would also like to thank my second supervisors, Dr Srinivasan Raghunathan and Dr Gerard Williger, for their support and valuable critiques in my research work.

I am grateful for the support from my family who have always provided strength, focus and inspiration, particularly my father who has always stood by my side and been a strong, supportive coach in all academic studies throughout my life.

I would like to thank my partner, Jack, for his patience, confidence in me, and enthusiasm about my work which often reminds me why I am so grateful to be in this position.

I would like to express my gratitude to the University of Central Lancashire and the Jeremiah Horrocks Institute for allowing me the opportunity to pursue a Masters by Research.



Figure 1. Snowy proofreading my thesis.

Lastly, this section would be incomplete had I not included a special thanks to my friendly, feathery companion, Snowy (Figure 1), who, on one occasion, even helped proofread my thesis with me.

Please enjoy!

List of Abbreviations

B18	Burenin et al. (2018)
B17	Burenin (2017)
C89	Crampton et al. (1989)
G08	Gal et al. (2008)
ISM	Interstellar Medium
KPO	Kitt Peak Observatory
LQG	Large Quasar Group
LSS	Large Scale Structure
MHO	Mount Hopkins Observatory
N05	Nakata et al. (2005)
O-03	Ohta et al. (2003)
R16	Raghunathan et al. (2016)
S12	Söchting et al. (2012)
T01	Tanaka et al. (2001)
tp-x	Tangent-Plane x
tp-y	Tangent-Plane y
Z&M	Zhu & Ménard (2013)

Chapter 1

Introduction

The standard model of cosmology – also known as the Concordance model or Λ CDM – consists of several cosmological parameters describing the matter, radiation and vacuum energies, as well as the expansion rate of the universe. In addition, the standard model of cosmology is founded upon two assumptions which originate from the Copernican principle, which states that our place in the universe is not special. That is, the universe should be homogeneous and isotropic on large scales. Homogeneity can be tested by looking at the large scale structure (LSS) of matter in the universe (and isotropy has been tested using the CMB maps). It has been suggested by Yadav et al. (2010) that the scale of homogeneity may be around $260 h^{-1}$ Mpc. However, it is well known that there are several structures that exceed scales of $260 h^{-1}$ Mpc such as the Clowes-Campusano Large Quasar group (CC-LQG), the Sloan Great Wall (SGW), the Huge Large Quasar Group (Huge-LQG), and the Giant Gamma Ray Burst Ring (Giant GRB ring) – see the following papers for further details respectively: Clowes & Campusano (1991); Gott et al. (2005); Clowes et al. (2013); and Balázs et al. (2015). In particular, it is becoming necessary to probe the high redshift universe to understand the structure-formation of matter at a younger stage of evolution. Due to telescope limitations, observing matter at high redshifts becomes increasingly difficult. For this reason, QSOs and other

CHAPTER 1

active galactic nuclei (AGNs) are generally used to map the LSS at high redshifts. A natural bias is introduced when such a selection criterion is made however, i.e., only the high mass, high luminosity objects are traced. A map of the non-luminous matter at high redshifts would complement the current sky surveys that map the high redshift luminous matter, and low redshift non-luminous matter, and ultimately provide the skeleton upon which LSS in the universe builds.

In this thesis I present a method of using intervening MgII absorbers as probes to the LSS of the universe and assess the potential of intervening MgII absorbers for cosmology. MgII is present in the low-ionised gas around galaxies and when light from background QSOs passes through this gas, the MgII can leave a prominent absorption feature. Searching for the MgII doublet in the spectra of QSOs can reveal where the mass along the line of sight (LOS) is located. With over 200, 000 QSO spectra available in SDSS DR7 and DR12 QSO catalogues from Schneider et al. (2010) and Pâris et al. (2017), and approximately 500 000 QSO spectra available in SDSS DR14 QSO database from Pâris et al. (2018), it is now possible to take advantage of the QSO catalogues for detecting the MgII distribution in the universe and thus outlining how and where structure forms.

Two independent authors, Zhu & Ménard (2013) and Raghunathan et al. (2016), present unique methods for detecting MgII in QSO spectra and create separate MgII databases from both DR7 and DR12 QSO catalogues. Software, developed by my supervisor, Dr R. Clowes, uses the MgII databases to create images which can be used for analysis and evaluation of LSS.

The aim of this thesis is to assess the potential of using intervening MgII absorbers as a probe to the large scale environment, and the use of intervening MgII absorbers in cosmology. Chapter 2 will be an introduction to MgII absorbers; the physics of the absorption doublet, and how MgII has been used in cosmology so far. Chapter 3 will review the methods used for this work such as: obtaining the

CHAPTER 1

MgII databases; how the software creates the MgII images; and the cluster and supercluster candidates selected for MgII analysis. Chapter 4 will be the results of each selected cluster candidate analysed in MgII. Chapter 5 will be a discussion on the work presented in this thesis. It will review and assess the potential for MgII in cosmology as well as discuss how the MgII method can be improved upon and used in future work. In this thesis the cosmological values according to concordance cosmology are used, with $H_0 = 70 \text{ kms}^{-1}\text{Mpc}^{-1}$, $\Omega_M = 0.27$ and $\Omega_\Lambda = 0.73$.

Chapter 2

MgII Absorbers

This Chapter will review the physics of MgII absorption and discuss some of the practical uses of MgII in astrophysics and cosmology.

MgII is a tracer of the low-ionised gas around galaxies. It has been proposed by Kacprzak et al. (2008) that the average radius at which MgII is present around a galaxy falls within a spherical shell roughly of size $43 \leq R \leq 88$ kpc. High energy electromagnetic (EM) radiation produced from a background quasar (QSO) can interact with the gas that falls along the line of sight (LOS) between Earth and the QSO. For instance, if the light from a background QSO were to pass through the halo of a galaxy where MgII was present, some energy would be absorbed by the MgII leaving an absorption feature in the spectrum of the QSO. The spectra obtained from background QSOs reveals information on the intervening mass along the LOS. Figure 2.1 is a diagram illustrating the process of light from a background QSO undergoing absorption from intervening gas along the LOS. The MgII absorption feature, seen in Figure 2.2, produces a very prominent doublet with rest wavelengths $\lambda 2796, \lambda 2803$, which can be seen in the optical wavelengths for a broad range of redshifts, $0.3 \leq z \leq 2.2$, Churchill et al. (2005). However, MgII can also be detected up to redshifts $z = 6.3$ in longer wavelength measurements, Barnes et al. (2014).

CHAPTER 2

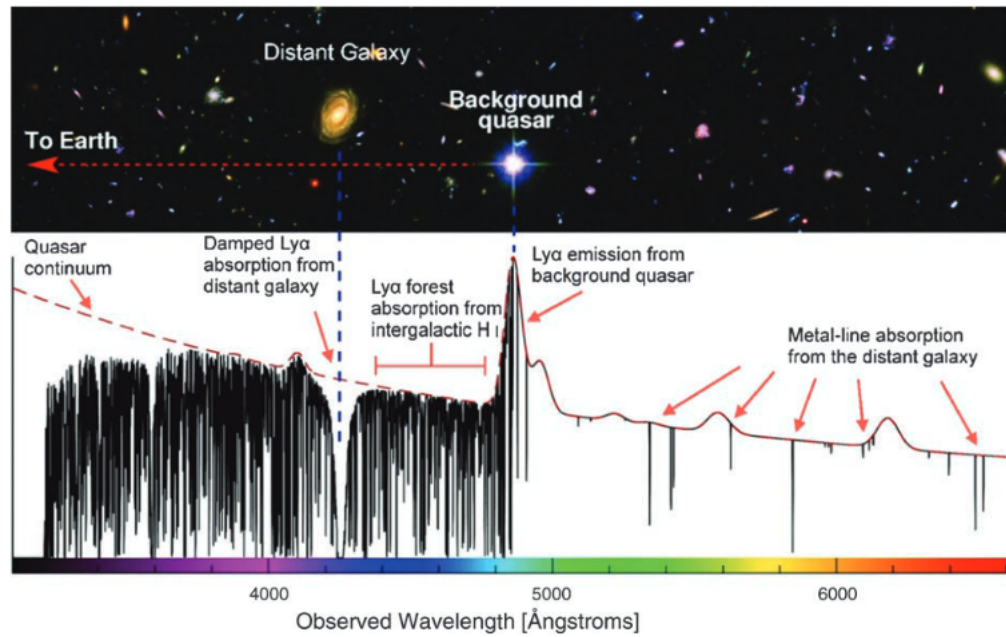


Figure 2.1. Diagram taken from Barnes et al. (2014) representing a QSO intervening with mass along the LOS leading to absorption and emission features in the spectra.

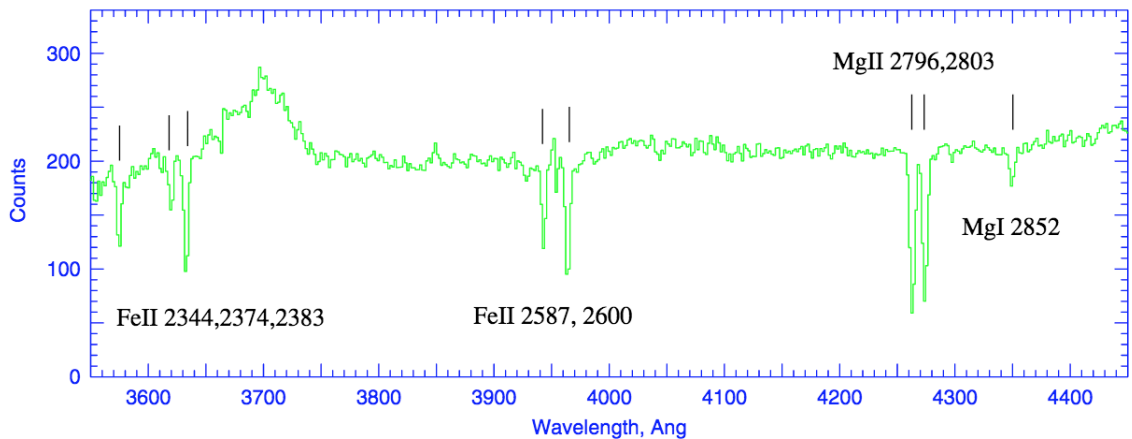


Figure 2.2. Image taken from Churchill et al. (2005) showing a typical QSO spectrum with the MgII doublet feature labelled. Note here that the FeII doublet feature looks quite similar to the MgII doublet, although the wavelength ratio of the FeII doublet is different to the MgII doublet.

CHAPTER 2

MgII is one of the strongest metal line absorbers that can be seen in the optical wavelengths at high redshifts ($z \sim 2.2$) and it can also be used to trace the neutral hydrogen at high redshifts where the 21 cm emission line can no longer be observed. The physics of galaxy formation and evolution can be further understood through the use of MgII absorption studies in high redshift galaxies – see, for example, Steidel & Sargent (1992), Evans et al. (2013) and Williger et al. (2002).

Recently, many redshift sky surveys have managed to cover a wide area of sky in low to intermediate redshifts – Canadian Network of Observational Cosmology (CNOC2) $0.1 < z < 0.6$, Galaxy and Mass Assembly (GAMA) $z \lesssim 0.5$, AGN and Galaxy Evolution Sky Survey (AGES) $0.085 < z < 0.66$, and many more. For more information on the listed redshift sky surveys see the following papers respectively: Yee et al. (2000), Baldry et al. (2010) and Kochanek et al. (2012). These sky surveys tend to be biased towards the high mass, high luminosity galaxies since they are easier (brighter) to observe with the current telescopes available. Observing the galaxy formation, structure and evolution of galaxies at high redshifts proves more difficult as the general completeness reduces. Photometric redshifts can be used instead of spectroscopic redshifts and provide a faster way of observing distant galaxies. However, photometric redshifts also lead to larger errors. Therefore, spectroscopic surveys are ideal for revealing the true nature of galaxy structure at high redshifts. Due to the nature of the MgII doublet feature – prominent and visible in the optical wavelengths up to redshift $z = 2.2$ – it is an ideal candidate for understanding the mass distribution at high redshifts. MgII is unbiased to the luminosity of a galaxy as the background QSO is the tool that highlights the faint galaxies along the LOS. Additionally, MgII is a strong tracer of the neutral hydrogen which is in association with star formation regions.

In the following Sections I will discuss the physical understanding of the MgII doublet and then I will review a small portion of the literature that has made use

CHAPTER 2

of MgII in Astrophysics and Cosmology.

2.1 Absorption Lines

The spectra obtained from distant QSOs can tell us a lot about intervening galaxies along the line of sight, such as: kinematics, chemical makeup, distance, redshift and age. Firstly, however, the general case for all spectral line measurements will be discussed.

The natural line width of a spectral transition line is characterised by the following equation:

$$\delta\omega = 2\pi\delta\nu = \frac{\delta\mathcal{E}_i - \delta\mathcal{E}_k}{\hbar} \equiv \gamma \quad (2.1)$$

where ν is the total frequency width of the line and \mathcal{E}_i and \mathcal{E}_k are the energies of states i and k between which the transition occurs. The corresponding line distribution known as the Breit-Wigner distribution (or Lorentz profile), is described by the following equation:

$$I(\omega) = I_0 \frac{\gamma}{2\pi} \frac{1}{(\omega - \omega_0)^2 + \gamma^2/4} \quad (2.2)$$

which generates a line profile as seen in Figure 2.3. Natural line broadening occurs due to the Uncertainty Principle which states that the uncertainty in the time spent by an atom in an excited energy state, and the uncertainty in the energy of the excited state, cannot be known with greater accuracy than $\delta\mathcal{E} \cdot \delta t \geq \hbar$.

In astrophysical observations there are a number of additional factors that contribute to the line profile of a spectral line; these are all broadening effects. Depending on the type of broadening present, astronomers can deduce properties of the source that the spectral line originates from. The two main causes of broadening are Doppler broadening and collisional broadening. Doppler broadening arises from the random motions of atoms and molecules in the source being observed. The random motions are the result of both thermal velocities of the atoms in the gas

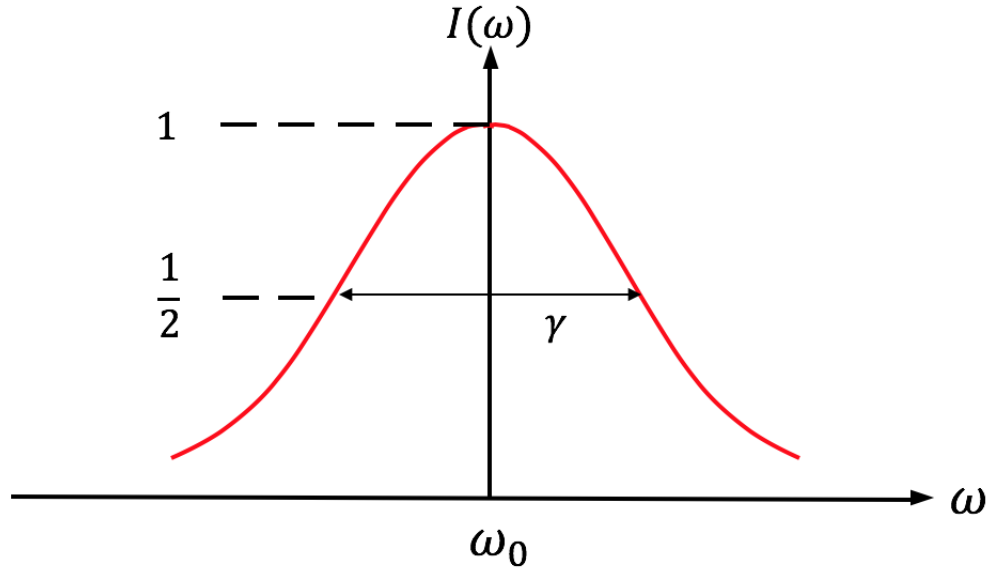


Figure 2.3. Figure adopted from Harwit (2006) showing the natural line width of a spectral line.

and the turbulent velocities within the gas.

For Doppler broadening effects, the full width at half the maximum intensity (FWHM) of a spectral line can be described by the following equation.

$$\delta = \omega_0 \left[\frac{2kT(\ln 2)}{mc^2} \right]^{\frac{1}{2}} \quad (2.3)$$

The line profile produced by Doppler broadening generally has a larger FWHM than the natural line width profile, but is narrower at the tails. This means that the tail ends of a spectral line are likely representative of either the natural line width or of other broadening effects which will be discussed next.

Collisional broadening occurs because the motions of particles lead to collisions between excited atoms, and when excited atoms collide they can lose energy and go back to the de-excited state. Therefore, collisions have the effect of increasing the probability of transitions occurring between atoms, as seen in Equation 2.4:

$$\frac{\delta\mathcal{E}}{\hbar} = \gamma + \gamma_c, \quad (2.4)$$

CHAPTER 2

where γ represents the spontaneous transition rate and γ_c represents the transition rate due to collisions. By comparison of Equations 2.1 and 2.4, one may notice that the general line profiles are the same with the only difference being that γ is replaced with $\gamma + \gamma_c$.

The atomic structure of MgII is similar to that of sodium, with an electron configuration: [Ne], 3s¹. The unpaired outer electron in the 3s orbital (where $\ell = 0$) may be excited to the 3p orbital (where $\ell = 1$) by absorbing light of a specific frequency. Due to magnetic interaction between the orbital angular momentum ℓ and the spin angular momentum s , the 3p orbital is split into two states with total angular momentum ($j = \ell \pm s$) equal to $j = \frac{1}{2}$ and $\frac{3}{2}$. The statistical weight corresponding to the total angular momentum for both states in the 3p orbital are calculated using the following equation.

$$g = 2J + 1 \tag{2.5}$$

Therefore the energy level with total angular momentum $j = \frac{1}{2}$ corresponds to a statistical weight of $g = 2$ and the energy level with total angular momentum $j = \frac{3}{2}$ corresponds to a statistical weight of $g = 4$. The energy level with slightly higher total angular momentum (and also an overall higher energy) corresponds to the higher energy wavelength in the MgII doublet at 2796 Å, and the lower energy level corresponds to the 2803 Å absorption line. Figure 2.4 is a diagram showing the fine splitting in the 3p orbital of MgII.

The statistical weight in the higher energy level is twice as large as the statistical weight in the lower energy level, so the number of sub-levels is doubled. In the MgII doublet, the 2796 Å absorption line is nominally twice as strong as the 2803 Å absorption line and the reason for this is due to the number of sub-levels being doubled. However, not unusually, the two wavelengths can be equally strong due to saturation (discussed in Section 2.2).

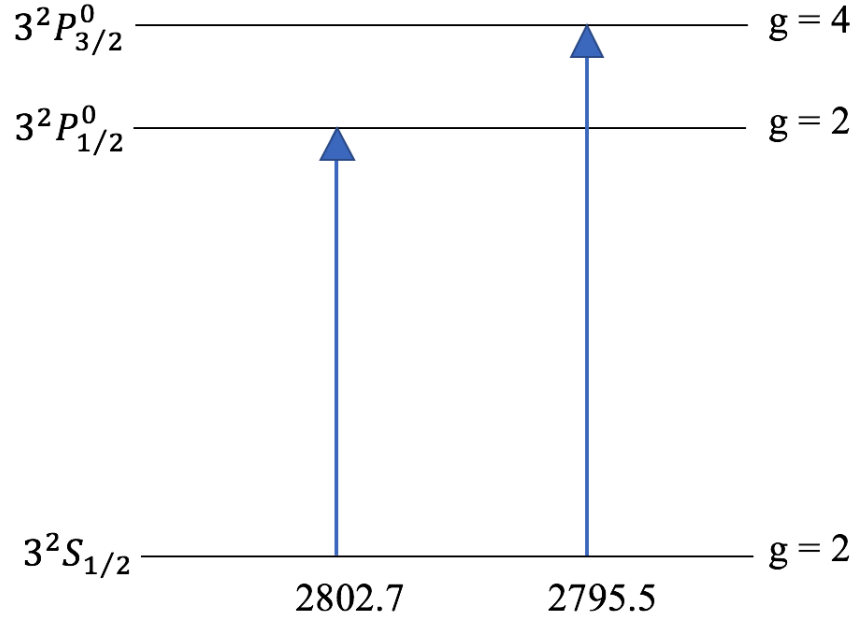


Figure 2.4. Figure adopted from Tennyson (2005) showing the 3s orbital and the two states of the 3p orbitals in MgII with their statistical weights labelled.

2.2 Equivalent Width

In absorption line studies the strength of an absorption line, defined by equivalent width W_λ , determines the fraction of energy of the line compared with the continuum, Spitzer (1978). Unlike line width and most other astronomical measurements, equivalent width is not affected by dust or Doppler broadening, which makes it an ideal parameter for galaxy observations. Equivalent width is characterised by the following equation:

$$W_\lambda = \int \left(1 - \frac{f_\lambda}{f_0}\right) d\lambda \quad (2.6)$$

where f_λ is the flux density across the wavelength region of interest and f_0 is the continuum flux density. Qualitatively, equivalent width is the width of a rectangle whose area is equal to the area of the absorption line and the height is equal to the value of the continuum flux density. Figure 2.5 illustrates how equivalent width

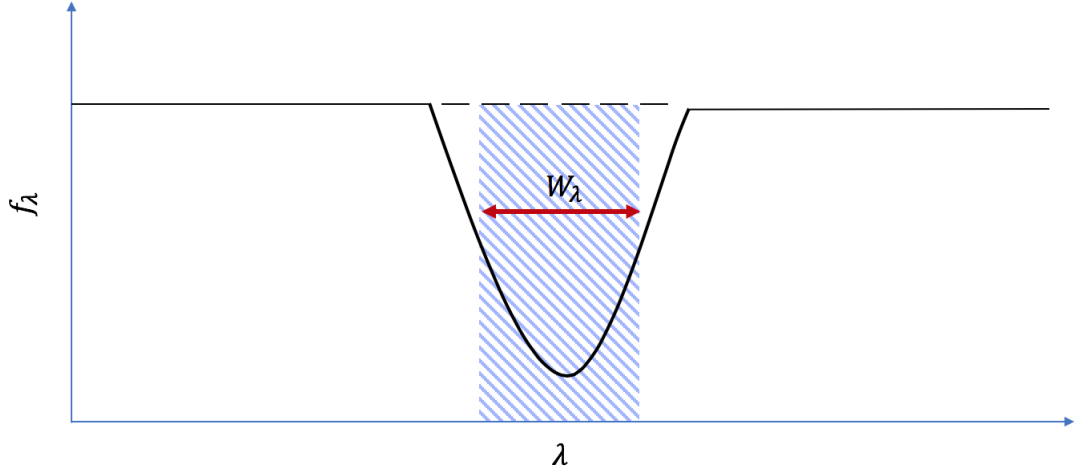


Figure 2.5. Diagram representing equivalent width compared with the absorption line. The area of the shaded rectangle is equal to the area between the continuum level and the absorption line.

corresponds to the absorption line. The larger the equivalent width the stronger the absorption line and therefore the greater the fraction of energy absorbed by (or emitted from) the spectrum. The energy of a spectral line, and hence the equivalent width, is proportional to the number density n_i , in a specific energy state i with multiplying coefficients of statistical weight, g , and the frequency of the oscillator strength of the energy state, f . This is until the absorption line reaches saturation, at which point the relationship between W_λ and gfn_i flattens. As the energy of the spectral line increases, the relationship between W_λ and gfn_i begins to rise again following a square-root law. The change in shape of the relationship between the energy of a spectral line and the number density is called the curve of growth – see Figure 2.6.

MgII absorption lines can be divided into two groups: strong and weak. Strong MgII absorption is sometimes defined as having an equivalent width $W_\lambda \geq 1.0 \text{ \AA}$. However in other texts one may find as well strong MgII absorption defined as $W_\lambda \geq 0.3 \text{ \AA}$, or $W_\lambda \geq 0.6$ – for example, Evans et al. (2013); Dutta et al. (2017);

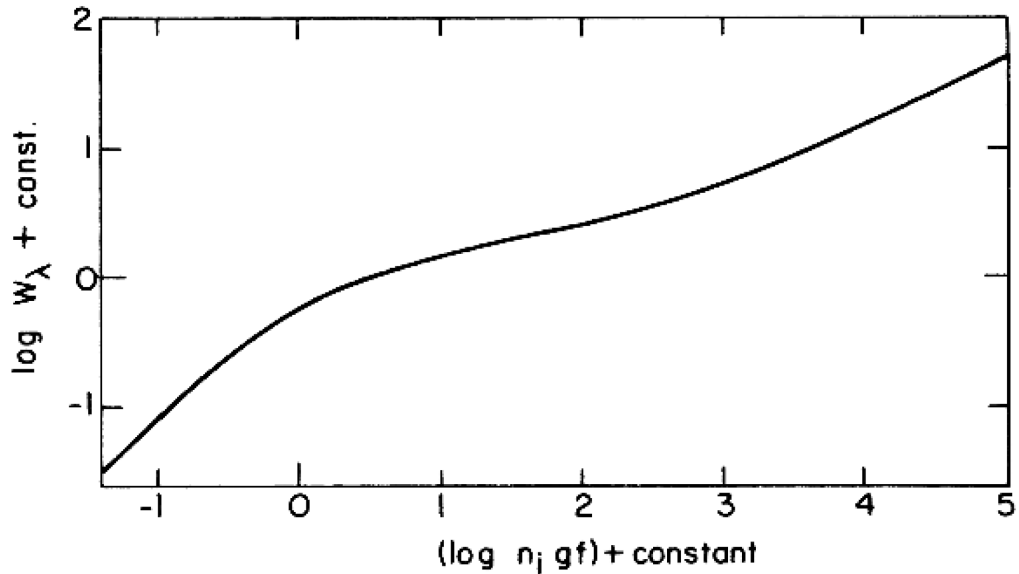


Figure 2.6. Figure taken from Harwit (2006) showing the curve of growth of the energy in a spectral line.

Churchill et al. (2005); Williger et al. (2002). Weak MgII absorption is usually defined as $W_\lambda < 0.3 \text{ \AA}$.

In a study by Churchill et al. (2005) an apparent connection between the distance from the centre of a galaxy and the strength of MgII absorption is discussed. In this study it is shown that there is also a relationship between the Strong MgII with Lyman Limit Systems (LLS), and the Weak MgII with Sub-Lyman Limit Systems. See Figure 2.7 for an illustration of the classes of absorbers, and where they occur with respect to the radial distance from the centre of the galaxy.

Due to the varying definitions of strong MgII absorption, I adopt my own definitions for weak, medium and strong absorbers with equivalent widths $W_\lambda < 0.3$, $0.3 \leq W_\lambda \leq 0.6$, and $W_\lambda > 0.6$ respectively, that will be used throughout this thesis.

CHAPTER 2

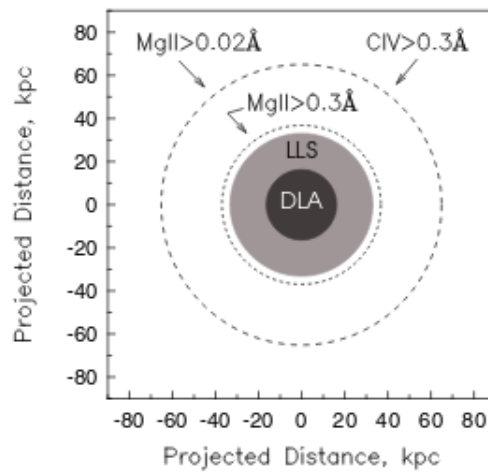


Figure 2.7. Diagram taken from Churchill et al. (2005) showing the preference of different classes of absorbers with radial distance from the centre of the galaxy. Notice how strong MgII and Lyman-limit systems (LLS) occur within similar regions. DLA refers to Damped Ly α systems which is when the MgII absorption profiles are fully saturated due to high column densities.

2.3 Cosmological Applications of MgII

Understanding MgII absorption systems in an astrophysical sense has been a topic of interest for over five decades and, as a result, there is much information available in the literature. A few examples include: Bates et al. (1970); Steidel & Sargent (1992); Lynch et al. (2004); Churchill et al. (2005); Evans et al. (2013); and Codoreanu et al. (2017). However, the cosmological applications of MgII, i.e, using MgII specifically for observing LSS, measuring cosmological parameters and understanding the formation, structure and evolution of the universe, are less common in the literature. A few examples are: Williger et al. (2002); Haines et al. (2004); and Clowes et al. (2013).

A study done by Williger et al. (2002) sought to understand the relationship between large QSO groups (LQG) and the galaxy distribution. The spectra of background QSOs can be used to illuminate the low-ionised gas around foreground galaxies as certain ions abundant in the gas, such as MgII and CIV, leave prominent absorption features in QSO spectra. Therefore, previously unregistered galaxies at high redshifts, that are too faint to see using spectroscopy, and even imaging, with the current tools available in astronomy, can be detected through the process of absorption from much brighter QSO spectra. In the study done by Williger et al. (2002) the spectra of 23 QSOs were obtained in a $2.5^\circ \times 2.5^\circ$ field centred on the Clowes & Campusano LQG (CC-LQG), Clowes & Campusano (1991), in the redshift region $1.23 < z < 2.68$. Overall, 42 MgII systems were detected in the selected QSOs, of which the weak MgII systems ($W_\lambda < 0.3$) represented a 2.4σ overdensity, based on the calculated redshift distribution of MgII systems from Steidel & Sargent (1992). Additionally, Williger et al. (2002) applied a minimal spanning tree (MST) algorithm and found clustering in ten of the weak MgII systems. The presence of MgII clustering in the study described above gives reason to suspect that observing the clustering of MgII absorbers may be used to highlight LSS and even trace the

CHAPTER 2

cosmic web. In doing so, an alternative means to map LSS of the Universe at high redshifts is presented.

The work presented in this thesis relies on the fundamental properties of MgII being a good tracer of the low ionised gas around galaxies that can be seen as strong, and even weak, absorption features in the spectra of distant QSOs.

Chapter 3

Method: Constructing MgII

Images

This Chapter will discuss different aspects of the steps taken that allows one to use intervening MgII absorbers for studying LSS.

3.1 Sloan Digital Sky Survey

The Sloan Digital Sky Survey (SDSS) comprises three telescopes: the Sloan Foundation 2.5 m Telescope located at Apache Point Observatory (APO) in New Mexico; the 2.5m Irénée du Pont Telescope at Las Campanas Observatory in Chile; and the New Mexico State University (NMSU) 1m Telescope at APO. Since SDSS began taking observations in 1998, there have been several surveys designed for various tasks, from studying the Milky Way (SEGUE-1) to surveying galaxies and QSOs in the high redshift universe (eBOSS). For the work that will be described in this thesis, there are two QSO databases, DR7QSO and DR12Q, presented by Schneider et al. (2010) and Pâris et al. (2017) respectively, from which the MgII databases were created. All of the QSO data used for the MgII analysis in this thesis originate from observations taken using the Sloan Foundation 2.5m telescope. A description

CHAPTER 3

	SDSS I-II	SDSS III
Number of Spectrographs	2	2*
Number of Fibres	640	1000
Fibre Diameter (")	3	2
Wavelength coverage (Å)	3800 - 9100	3600 - 9400

Table 3.1. Main instrumental differences between SDSS I-II (Legacy, DR7) and SDSS III (BOSS, DR12). * There are the same number of spectrographs in SDSS I-II and SDSS III, however, improvements in sensitivity were made to the new spectrographs in SDSS III and the number of fibres per spectrograph was increased (640 to 1000). Information provided by the SDSS website.

of the MgII databases is presented in Section 3.3.

DR7QSO mostly comprises data collected from the Legacy survey in SDSS I-II. The Legacy survey ran from 2000 to 2008, providing spectroscopic and photometric images of over 7500 deg² of the northern galactic sky and three stripes in the southern galactic cap. All of the data for DR12Q were taken from the Baryon Oscillation Spectroscopic Survey (BOSS) in SDSS III, which ran from 2009 to 2014. Some key changes from SDSS I-II to SDSS III are listed in Table 3.1.

The fourteenth data release (DR14) QSO catalogue (DR14Q) presented by Pâris et al. (2018) obtains its data from eBOSS in SDSS IV. The MgII catalogue, available online from Dr S. Raghunathan, was originally included in the MgII databases for MgII analysis. However, it was decided to omit the DR14Q MgII catalogue from the MgII analysis because the rate of detection of MgII absorbers seemed lower than expected, given the generally improved SNR. This anomaly will be investigated further.

In SDSS DR7QSO there were 105,783 QSOs spectroscopically observed in the redshift range $0.065 < z < 5.46$ with a typical redshift error $\Delta z < 0.004$. All QSO

CHAPTER 3

luminosities in DR7QSO have $M_i < -22.0$. The position of each QSO in the QSO catalogue is known with accuracies greater than $0.1''$; see Schneider et al. (2010) for more information. In SDSS DR12Q a total of 297 301 QSOs were detected by BOSS, of which 272 026 were new discoveries. QSOs below redshift $z < 2.0$ have luminosities larger than $M_i < -20$. For further information of the cleaning, reduction and selection processes of both QSO catalogues, DR7QSO and DR12Q, see Schneider et al. (2010) and Pâris et al. (2017) papers, respectively.

3.2 Night Sky Lines

Night sky lines often complicate spectroscopic observations. The MgII databases used for the purpose of this work originate from spectroscopic observations taken by SDSS. Therefore, a short discussion of night sky lines is included here as they become important later for understanding and evaluating the completeness of the MgII databases.

A study done by Massey & Foltz (2000) compares the night sky at two different sites, Kitt Peak and Mount Hopkins in southern Arizona, in 1988, 1998 and 1999 to understand the effect of night sky emissions and sky brightness, and how that changed over a 10 year period. The results for absolute spectrophotometry of the night sky at Kitt Peak Observatory (KPO) taken in 1988 is described in Massey et al. (1990). In addition, independent observations were made by C. Foltz at the Mount Hopkins Observatory (MHO) in 1988. The two studies, despite being originally independent of each other were carried out by very similar methods and so the studies were combined. The observations of the 1998 MHO night sky spectrophotometry were obtained by P. Berlind. I will present a short review of the results and conclusions of the Massey & Foltz (2000) paper, but for further information on the details of the observations see Massey et al. (1990) and Massey & Foltz (2000).

Both independent authors of the original MHO and KPO observations make

CHAPTER 3

measurements of the sky at the zenith and at large zenith angles, up to 60° . Additionally, measurements were made at angles at least 15° away from the galactic plane to avoid complications with galactic plane absorption features. The spectra were cleaned with a median filter and any resolved stars were removed. The follow up 10-11 year measurements at MHO and KPO were carried out in a similar manner.

Figure 3.1 is taken from Massey & Foltz (2000) and shows the comparison of the zenith sky brightness as measured from MHO (dotted line) and KPO (solid line) in 1998 and 1999 respectively. The two independent measurements agree and have an absolute error of approximately $0.03 - 0.06 \text{ mag arcsec}^{-2}$. Present in the spectrum of both observations is a strong and broad emission feature in the wavelength range $5600-6300 \text{ \AA}$ which is a result of the high-pressure sodium (HPS) street lamps, which contributes approximately $0.17 \text{ mag arcsec}^{-2}$. Another noticeable contribution to the night sky emissions is the OI $\lambda 5577$ atmospheric line, or auroral line. This particular emission arises due to solar activity and therefore its contribution to night sky emission varied from each observation. The average contribution of the auroral line was $0.16 \text{ mag arcsec}^{-2}$ with variations of $\sim 0.1 \text{ mag arcsec}^{-2}$. It is worth noting that, not entirely coincidentally, the separation time for observations, 10-11 years, is the same for that of the solar activity cycle (11 years), meaning all observations were taken at a similar time of solar activity. The observations discussed in this paper were taken during high solar activity. It has been suggested by Pilachowski et al. (1989) and Massey & Foltz (2000) that the night sky may be several tenths brighter in magnitude relative to solar minimum.

The re-observations taken 10-11 years later highlighted an increase in HPS emission and UV for both sites. This is likely due to the approximate 26% population increase in the nearby city Tucson and the 29% population increase in eastern Pima County which in turn increases the demand for street lighting and other sources of light pollution. That being said, the increase in population in the 10 years is much

CHAPTER 3

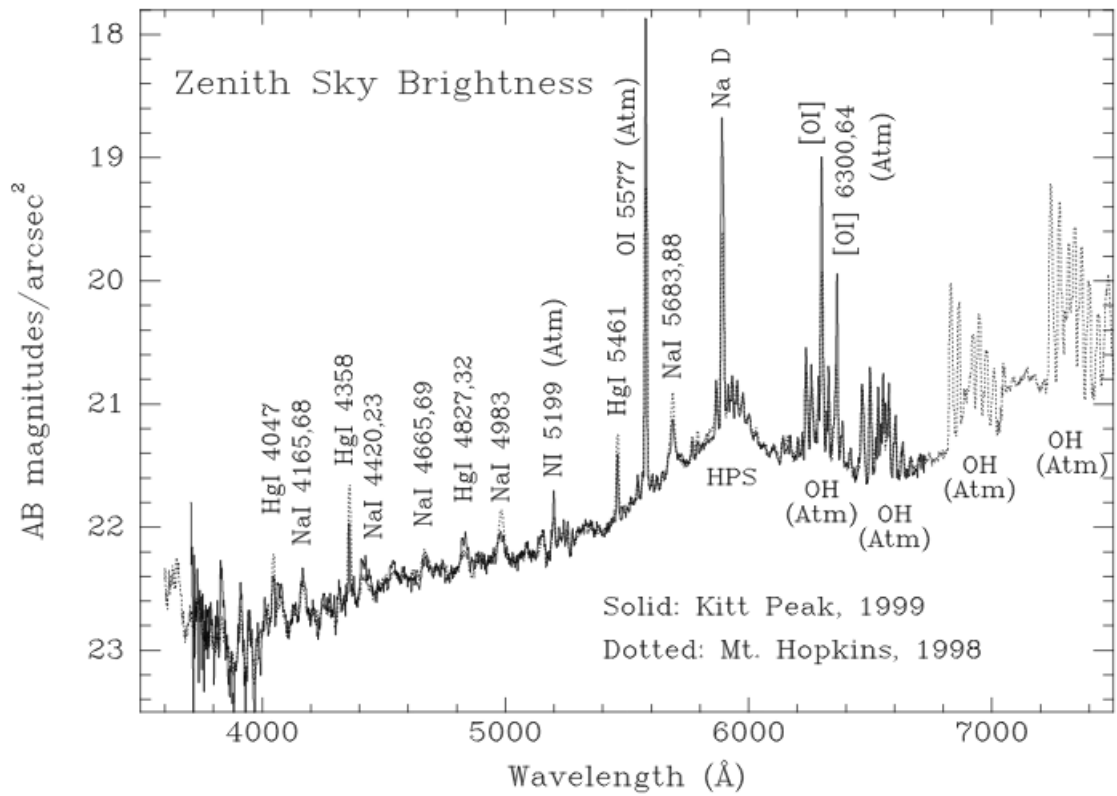


Figure 3.1. Figure taken from Massey & Foltz (2000). Zenith sky brightness at the Mount Hopkins observatory in 1998 (dotted line) and the Kitt Peak observatory in 1999 (solid line) superimposed, emphasising the good agreement between the two separate observations. Note the strong OI $\lambda 5577$ and broad HPS features.

CHAPTER 3

more severe than the increase in HPS emission suggesting that night sky brightness rate of increase is considerably lagging behind the population growth. Also, the 1998 - 1999 night sky brightness is comparable to the Palomar observatory in the 1970s which was believed to be the pinnacle of good quality observing conditions. Additionally, the overall increase in brightness across the night sky was marginal, approximately $0.1 \text{ mag arcsec}^{-2}$.

Finally, the comparison of spectra obtained at angles facing Tucson and facing the zenith for both observing sites highlights the additional contribution of HPS in populated areas. In fact, the position facing Tucson is found to have the greatest increase in night sky emissions compared with any other angle. Although, in general, the brightness increase at large zenith angles is often due to natural airglow.

I made use of two independent sources of MgII detection databases: Zhu & Ménard (2013) and Raghunathan et al. (2016), from here on referred to as Z&M and R16 respectively. Both authors obtained their data from the QSO SDSS seventh and twelfth data releases (DR7 and DR12 respectively), presented by Schneider et al. (2010) and Pâris et al. (2017), respectively. From plotting a histogram of the MgII absorbers across redshift for all four MgII databases (Z&M: DR7 and DR12, and R16: DR7 and DR12, Figures 3.2 and 3.3), one can see that the graphs produced by R16 (Figure 3.3) features troughs and peaks throughout, especially so in DR12 (bottom panel of Figure 3.3) towards the higher redshift end of the spectrum (corresponding to longer wavelengths). The peaks and troughs at the high redshift end of the MgII distribution indicates a selection process made by R16 as opposed to a naturally occurring feature. The omission of absorbers in certain redshift slices reduces the chance of selecting false absorbers which are likely either the result of under-subtracting sky lines (explained later in this text) or galactic absorption. The two sets of databases presented by Z&M and R16 adopt different approaches to coping with the night sky lines. Note that the night sky line observations made

CHAPTER 3

at Apache Point Observatory can be found in Law et al. (2016).

Z&M started their selection process by making cuts to the SDSS QSO database. The first cut, and the largest cut, removing 16 705 QSO spectra, was made to avoid the complicated continuum estimation from QSOs containing broad absorption lines (BALs) or spectroscopic artefacts. Next, QSO spectra with inadequate pixel information in the wavelength ranges used for flux normalisation were rejected, reducing the total number of viable QSOs by 55. QSOs lying outside the redshift range $0.4 < z < 4.7$ were cut from the sample as MgII cannot be detected in this range, totalling a further reduction of 5901 QSOs. Altogether a sample of 84 533 QSOs remain which were suitable for narrow absorption line detection.

A search window criterion was applied to the remaining sample of QSOs to avoid problematic sky lines and false detections. Firstly, wavelengths blueward of the CIV emission line were excluded as any absorption features in this range are more likely to be CIV absorption lines than MgII absorption lines. Similarly, wavelengths redward of the MgII emission line were excluded, meaning the final search window covered wavelengths in the SDSS range $3800 \leq \lambda \leq 9200 \text{ \AA}$. Inside the search window the CaII absorption feature can often be confused with a MgII doublet at redshift $z = 0.4$, therefore the CaII $\lambda\lambda 3934, 3969\text{\AA}$ lines are masked out to avoid false positive detections. After this, Z&M follow a three-step method for the final MgII detection catalogue.

The overall completeness of Z&M MgII catalogue fluctuates across the whole redshift range and this is largely to do with the various sky lines, such as HPS at 5900 \AA and atmospheric OH lines in the red end of the spectrum – see Figure 3.4 taken from Z&M.

R16 made two cuts in their data to eradicate the problem of night sky lines and galactic absorption. Firstly, the CaII absorption line ($\lambda\lambda 3934, 3969\text{\AA}$) present in the ISM of the Milky Way can lead to absorption that often mimics a MgII doublet at

CHAPTER 3

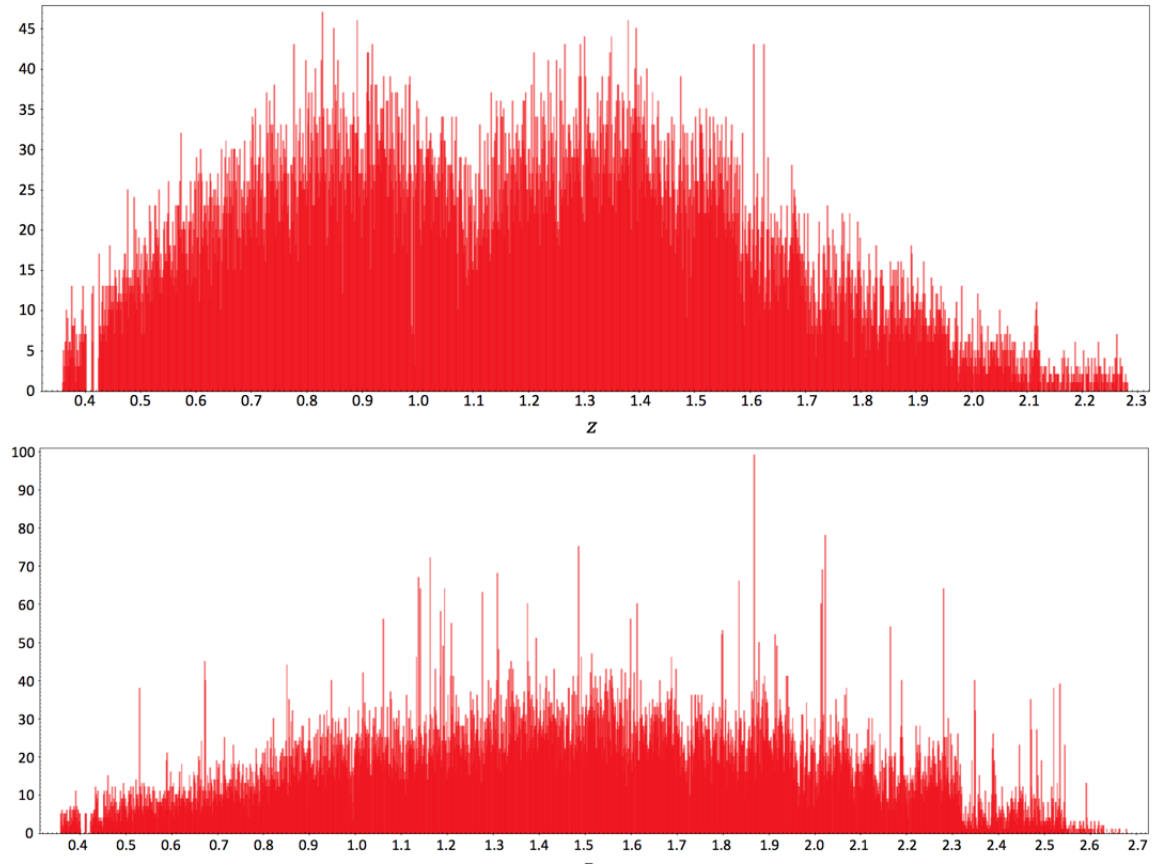


Figure 3.2. Number of MgII absorbers across redshift in the Z&M DR7 (top) and DR12 (bottom) MgII databases. Bin width = 0.001. Note the omission of absorbers at redshift $z \sim 0.4$ which corresponds to the CaII lines present in the ISM of the Milky Way. Also, note in the top panel, DR7, the broad dip in absorbers centred at redshift $z \sim 1.1$. This is where HPS features are present and also the redshift at which the SDSS blue spectrograph is superseded by the red spectrograph. This feature is not apparent in the bottom panel, DR12, because of the improvements made to the sensitivity of the spectrographs in SDSS III.

CHAPTER 3

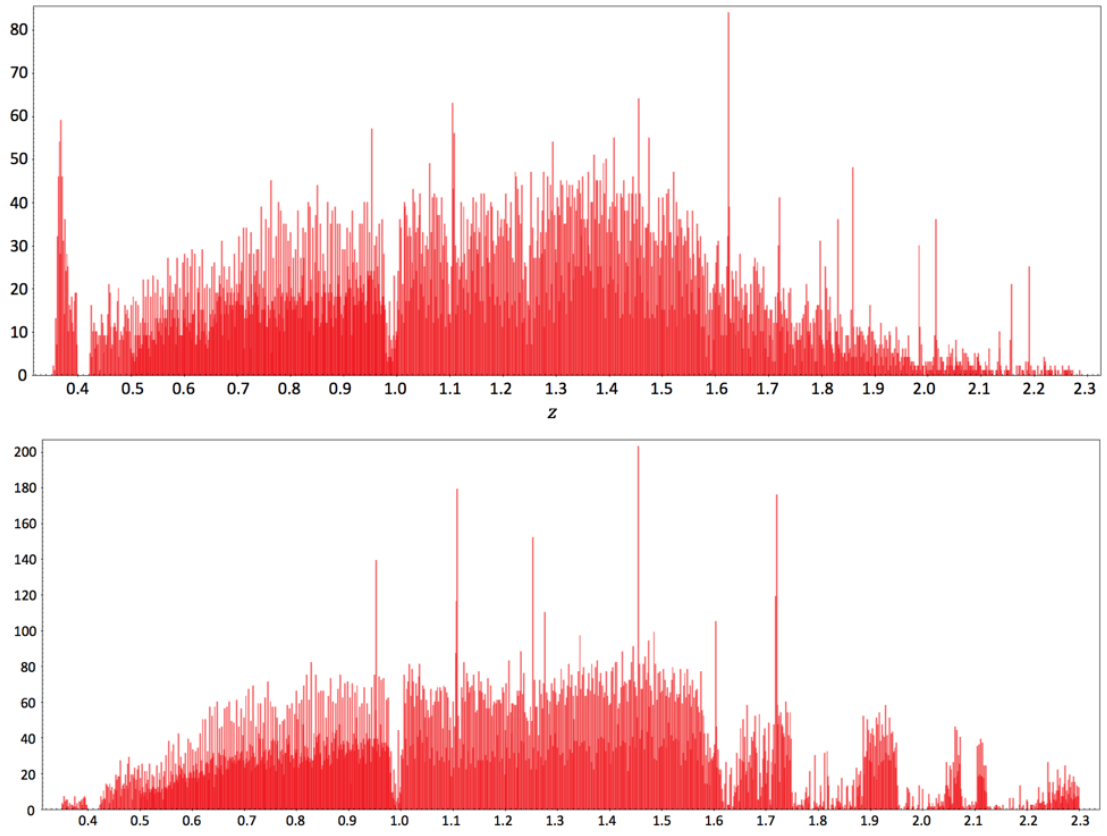


Figure 3.3. Number of MgII absorbers across redshift in the R16 DR7 (top) and DR12 (bottom) MgII databases. Bin width = 0.001. Note the omission of absorbers at redshift $z \sim 0.4$ which corresponds to the CaII lines present in the ISM of the Milky Way, along with several additional cuts of data at $z \sim 1.0$, $z \sim 1.1$ and $z \sim 1.25$. Note in the bottom panel, R16 DR12, the broad peaks and troughs redward of redshift $z \sim 1.6$

CHAPTER 3

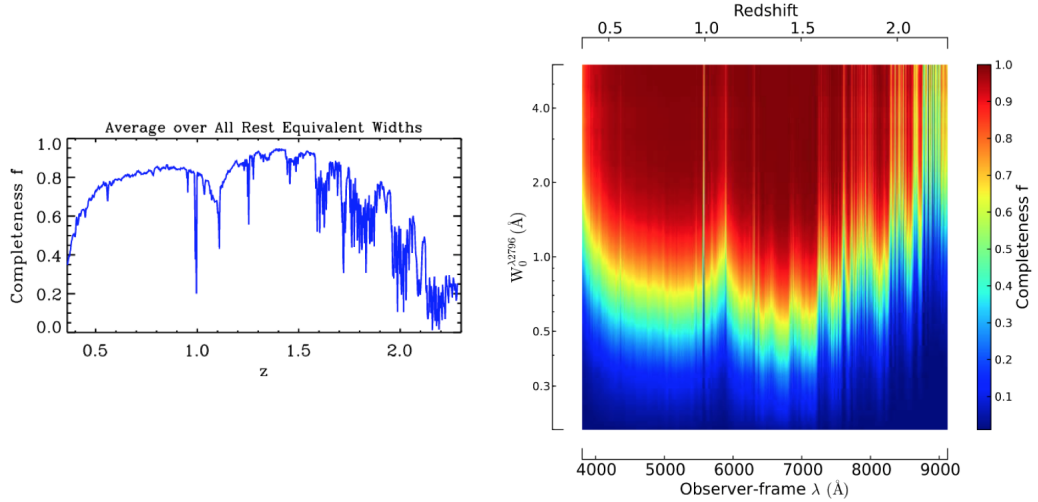


Figure 3.4. Figures taken from Z&M. Left panel: average completeness over all rest equivalent widths as a function of redshift. Right panel: completeness as a function of redshift and equivalent width.

redshift 0.4. Therefore, a 60 \AA mask was applied in the wavelength range $3920\text{--}3980 \text{ \AA}$ to avoid false positive detections arising from this complication, similar to how Z&M deal with this particular sky line. Also, the difficulty in sky subtraction at the longer wavelengths, where OH atmospheric emission lines ($\lambda \gtrsim 6900 \text{ \AA}$) become very complicated, can result in absorption-like features that mimic the MgII doublet. To address this problem, SDSS bitmasks were applied and a threshold was set such that any detections that were within 4 \AA of a masked pixel were removed. Figure 3.5 shows the comparison of the MgII counts before sky lines and other non-MgII features were removed (black) and after the sky lines and non-MgII features have been either removed or masked (green). By comparing the two overlaying histograms in the OH line region, one can see the mass reduction of MgII counts after the bitmasks are applied (green) which highlights the severity with which atmospheric sky lines complicate the process of detecting MgII in this region.

Whereas Z&M set their search window to begin redwards of the CIV emission line to avoid confusion of CIV absorption features mimicking the MgII doublet, R16

CHAPTER 3

simply flagged all systems (21% in total) that could potentially confuse CIV for MgII blueward ($\Delta z = 0.03$) of the CIV emission feature.

Next, the strong sky emission lines were managed with a sky line finder (SF) developed by R16. The strong sky lines, [OI] (5577 Å, 6300 Å, 6364 Å), and Na (5890, 5896 Å) can be seen as strong black peaks in Figure 3.5 at their corresponding wavelengths. Note, some of the cuts made by R16 could be eliminating some real MgII absorbers. SF works via the following steps.

1. SF scans each QSO spectrum and applies masks comprising three windows on each of the sky lines.
2. The central window is adjusted to cover the sky line (ranging from 5 – 20 pixels) and the two remaining windows – the control windows – are set either side of the central window covering 5 pixels each.
3. The scatter in the flux in all three windows is calculated.
4. If the condition $\sigma_{central} \geq \sigma_{control}$ is met, the mask then removes all systems within the windows corresponding to the sky line.

In total, 2.5% of the systems near sky lines were removed.

By comparison of the techniques utilised by Z&M and R16, one may notice that in general Z&M make much fewer cuts to the data than R16. For this reason it is now more clear why Figure 3.3 feature broad peaks and troughs, especially so towards the higher redshift region (longer wavelengths corresponding to the OH lines) in the bottom panel of Figure 3.3. Therefore, it is natural to assume that R16 has a much lower completeness in their data simply due to the number of cuts made in processing the sky lines. For this reason I assign higher priority to the Z&M databases in my work, which will be discussed further in Section 3.3.

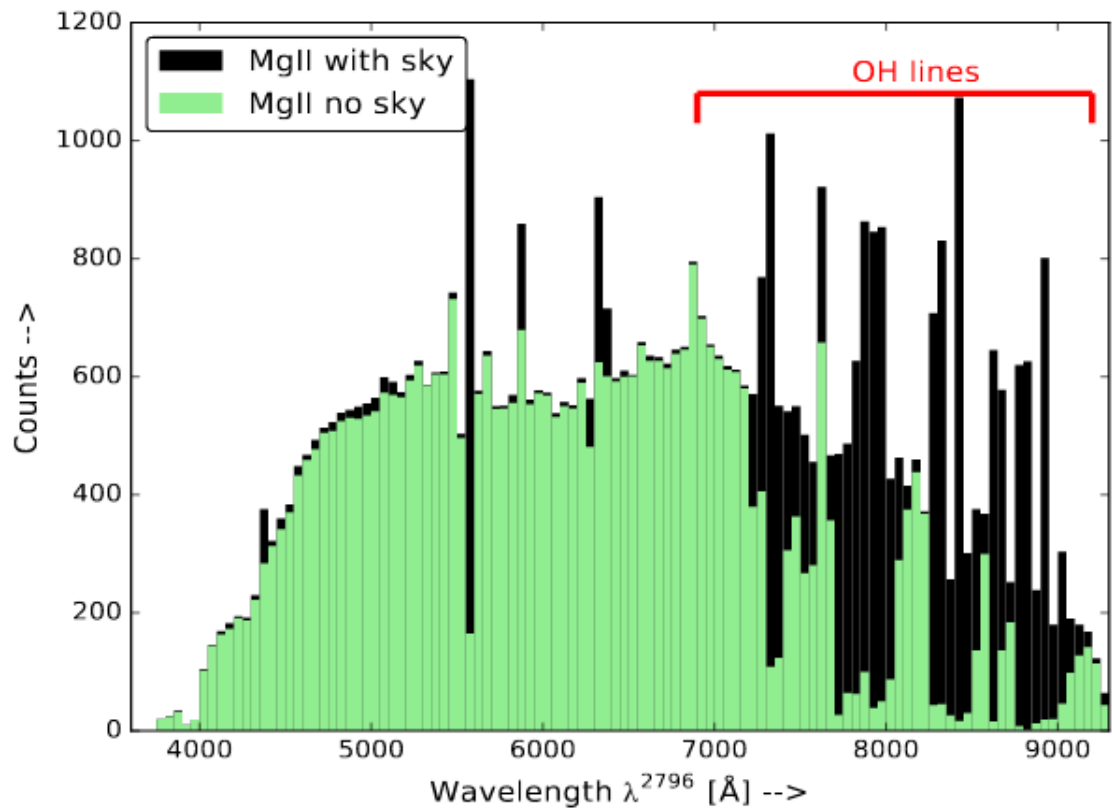


Figure 3.5. Figure taken from R16. MgII counts in the database as a function of wavelength before applying techniques dealing with sky lines and galactic absorption (black) and after the techniques were applied (green). The OH line region is marked.

3.3 The Databases

Z&M and R16 present separate MgII databases from SDSS DR7 and DR12 which were generated using independent detection procedures. Both authors provide two MgII databases each totalling four unique MgII databases. The four unique databases have been combined in different ways to produce additional MgII databases which are described in Table 3.2 and in the following text. Tables 3.3, 3.4 and 3.5 provide additional information on the object databases, the percentage distribution of the different classes of absorbers in each of the databases and the number of duplicated absorbers in the paired databases.

The following text refers to the information provided in Table 3.2. R-dr7 and R-dr12 refer to the databases produced by R16 which have been paired with the object databases DR7QSO from Schneider et al. (2010) and DR12Q from Pâris et al. (2017), respectively. Likewise, ZM-dr7 and ZM-dr12 are the databases created by Z&M which have been paired with the object databases DR7QSO from Schneider et al. (2010) and DR12Q from Pâris et al. (2017), respectively. R-comb is the combined absorbers from databases R-dr7 and R-dr12 with duplicate absorbers removed, just as ZM-comb is the combined absorbers from databases ZM-dr7 and ZM-dr12 with duplicate absorbers removed. R-field-all has paired absorbers from both authors' combined databases, with duplicate absorbers removed and calculated using R16 fields, and ZM-field-all has paired absorbers from both authors' combined databases, with duplicate absorbers removed and calculated using Z&M fields only. Note, R16 uses the raw redshift calculations from the basic SDSS Data Release (Z_PIPE) for their DR12 MgII database, a small percentage of which are incorrect. Therefore, included in the software is a condition that finds the subset of redshifts in DR12 that match the corrected version of redshifts (Z_VI) within ± 0.1 . This was not necessary for Z&M redshifts since they use the corrected redshifts from Hewett & Wild (2010) for their DR7 MgII database and the visually corrected redshifts for their DR12

CHAPTER 3

Database	Object Database	no of abs	abs per deg ²
R-dr7	DR7QSO	21 854	2.41
R-dr12	DR12Q	39 694	3.98
ZM-dr7	DR7QSO	35 752	3.77
ZM-dr12	DR12Q	41 895	3.94
R-comb	DR7QSO, DR12Q	57 249	5.51
ZM-comb	DR7QSO, DR12Q	63 876	6.55
R-field-all	DR7QSO, DR12Q	27 505	2.86
ZM-field-all	DR7QSO, DR12Q	27 505	2.83

Table 3.2. Table of databases used in the software. More information for each database is provided in the following text. Note the following: the first column is the reference name given to the databases, the second column is the object database from which the corresponding MgII database originates, the third column refers to the total number of MgII absorbers in the relevant database and the last column is the average number of MgII absorption systems per square degree across the whole redshift range.

MgII database.

The paired, combined databases, R-field-all and ZM-field-all, are the most reliable MgII databases as these have absorbers in common to both authors. That is, the MgII absorbers present in the paired, combined databases are less likely to be random or the result of a false positive if they were found by both authors via independent detection procedures. However, note that even though the MgII absorbers

CHAPTER 3

Object Database	Total	Notes
DR7QSO	105 783	Details found in Schneider et al. (2010)
DR12Q	297 310	Details found in Pâris et al. (2017)
DR7QSO + DR12Q	377 806	Duplicates removed

Table 3.3. Total number of QSOs in the object databases.

Database	Weak	Medium	Strong	V. Strong(> 1.0)	$W_{\lambda max}$	$W_{\lambda min}$
R-dr7	0.0411	10.1	89.9	61.1	6.40	0.236
R-dr12	0.0428	8.05	91.9	67.9	6.27	0.229
ZM-dr7	2.72	18.8	78.4	49.4	8.42	0.00174
ZM-dr12	4.58	20.7	74.7	47.7	9.10	0.00173
R-comb	0.0437	8.71	91.2	65.7	6.40	0.288
ZM-comb	3.55	19.6	76.9	48.9	9.10	0.00173
R-field-all	0.0109	9.29	90.7	61.3	4.49	0.280
ZM-field-all	1.46	15.9	82.7	54.9	6.70	0.00335

Table 3.4. Table of the percentage split of classes of equivalent widths in the different MgII databases. Columns 2 to 5 are percentages of the number of MgII systems in the corresponding database (see Table 3.2). Weak, medium and strong equivalent widths are defined in Chapter 2.2. Note, all equivalent width values are determined from the 2796 Å line. Also note that four of the absorbers in ZM-dr12 were ignored and not included in any of the above calculations as they have equivalent widths of the order $\times 10^{-11}$ which suggested they were spurious absorbers. Similarly, eight of the absorbers in ZM-comb were ignored for the same reason.

present in both paired, combined databases are the same, the estimated equivalent widths differ noticeably (see Table 3.4) due to the fact that the equivalent widths are estimated differently by each author. As is expected, pairing the combined

CHAPTER 3

Pairing	Database	Duplicate abs.
R-dr7 and R-dr12	R-comb	625
ZM-dr7 and ZM-dr12	ZM-comb	237
R-comb and ZM-comb	R-field-all	8 309

Table 3.5. Number of duplicate absorbers in the paired databases.

databases from two separate authors and removing all the MgII absorbers not in common to both combined databases reduces the overall number of MgII absorbers present with respect to the remaining databases, as can be seen in Table 3.2 (with the exception of R-dr7 which has the lowest number of MgII absorbers present). Often the reduced signal can make it difficult to assess the LSS. However, if a structure is detected in the paired, combined databases then the signal can quite often stand as there is less noise in the background from spurious/random absorbers. Using the paired, combined databases is useful for assigning confidence to the absorbers and potential structures in the MgII images. I have created plots to visually compare the differences in each of the databases. A selection of sky has been chosen arbitrarily at RA = 190° and Dec = 35°, as has the redshift ($z = 1.4$), redshift thickness (± 0.1) and smoothing scale (17 Mpc). The parameters have been set the same for all of the databases to allow for a fair comparison; see Figure 3.6 to 3.13 for these.

The number of MgII absorbers in each database varies across the whole sky. Figure 3.14 and 3.15 are the TOPCAT (version 4.6-3), Taylor (2005), all sky images of the QSO distribution in databases which highlight the non-uniformity in some areas of the sky, i.e., the dark and light patches. In the all sky image of R-7, left panel of Figure 3.15, there are multiple gaps in the data. Where there are no background QSOs, potential MgII absorbers go undetected which emphasises the need for more coverage/databases.

The largest database is ZM-comb with 63 876 MgII absorption systems detected

CHAPTER 3

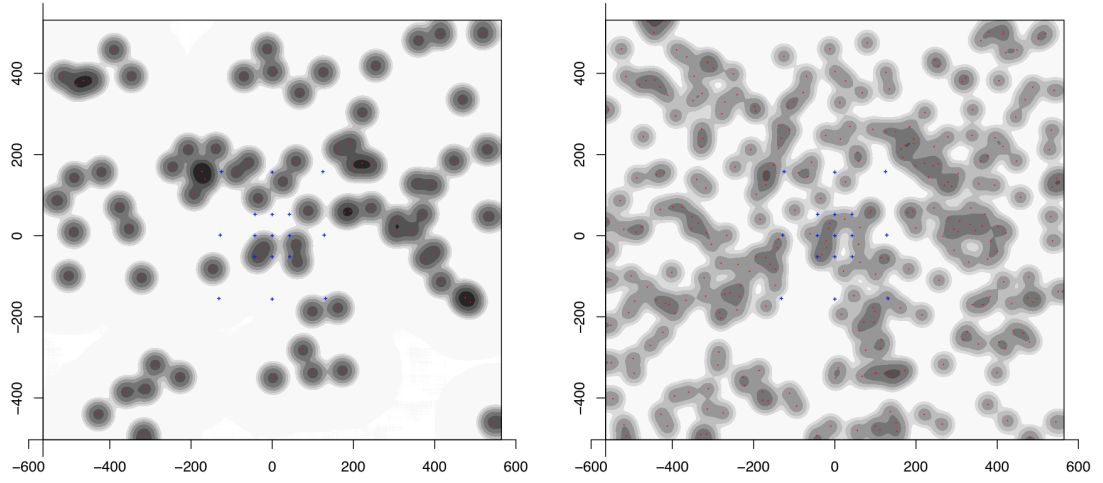


Figure 3.6. Database comparisons – R-dr7. Left panel: MgII absorbers represented by red dots. Right panel: Available background probes represented by red dots. In both images grey contours represent the density distribution using a Gaussian kernel (17 Mpc), and blue dots mark out a reference grid.

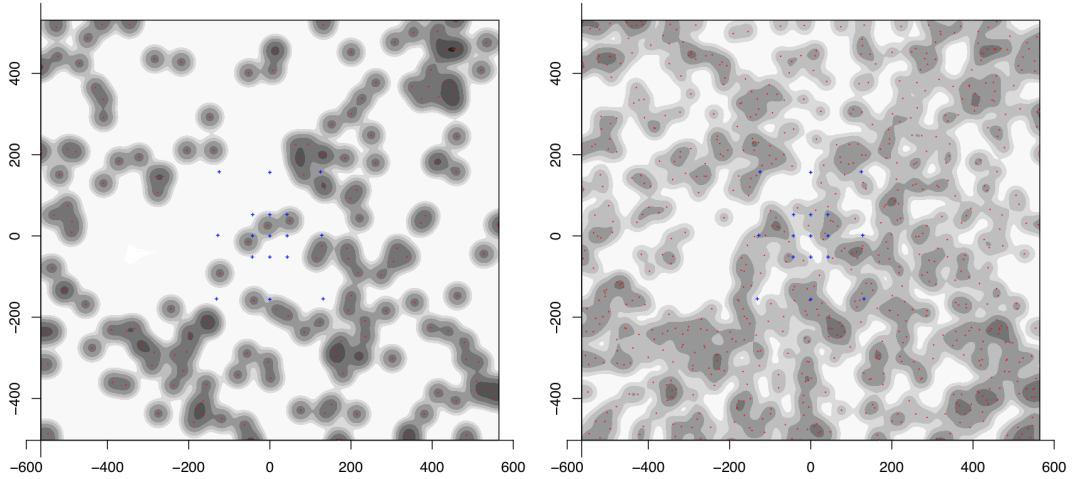


Figure 3.7. Database comparisons – R-dr12. Left panel: MgII absorbers represented by red dots. Right panel: Available background probes represented by red dots. In both images grey contours represent the density distribution using a Gaussian kernel (17 Mpc), and blue dots mark out a reference grid.

CHAPTER 3

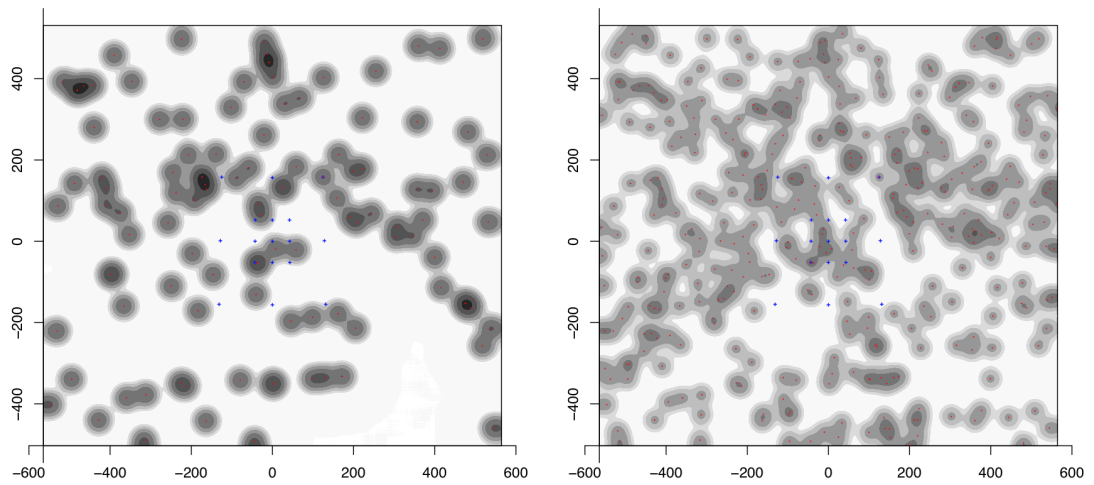


Figure 3.8. Database comparisons – ZM-dr7. Left panel: MgII absorbers represented by red dots. Right panel: Available background probes represented by red dots. In both images grey contours represent the density distribution using a Gaussian kernel (17 Mpc), and blue dots marks out a reference grid.

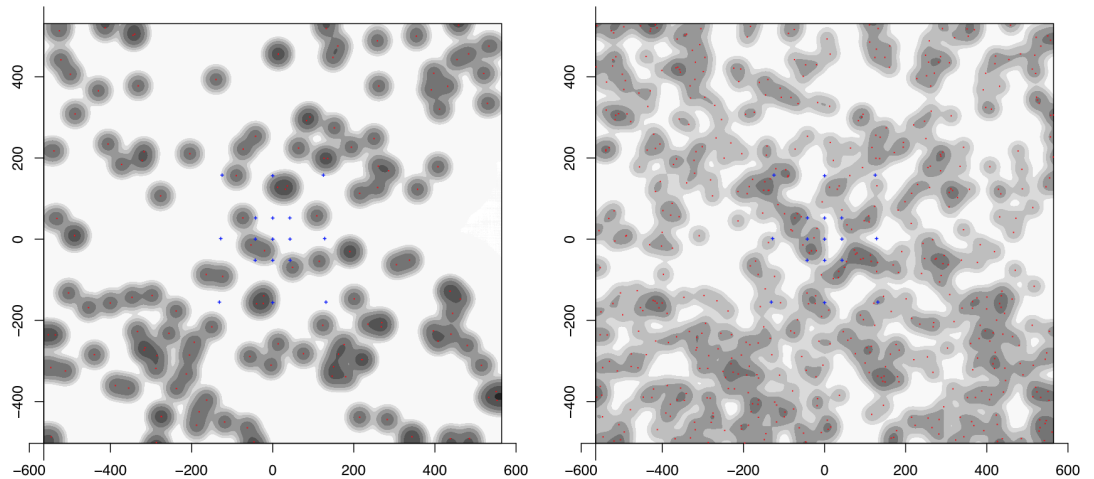


Figure 3.9. Database comparisons – ZM-dr12. Left panel: MgII absorbers represented by red dots. Right panel: Available background probes represented by red dots. In both images grey contours represent the density distribution of the MgII absorbers smoothed with a Gaussian kernel (17 Mpc), and blue dots marks out a reference grid.

CHAPTER 3

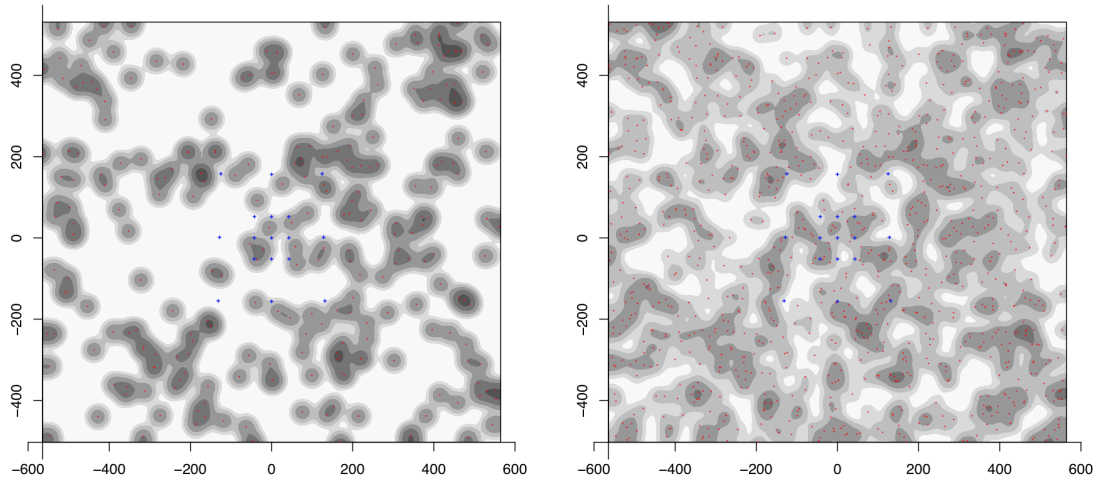


Figure 3.10. Database comparisons – R-comb. Left panel: MgII absorbers represented by red dots. Right panel: Available background probes represented by red dots. In both images grey contours represent the density distribution of the MgII absorbers smoothed with a Gaussian kernel (17 Mpc), and blue dots marks out a reference grid.

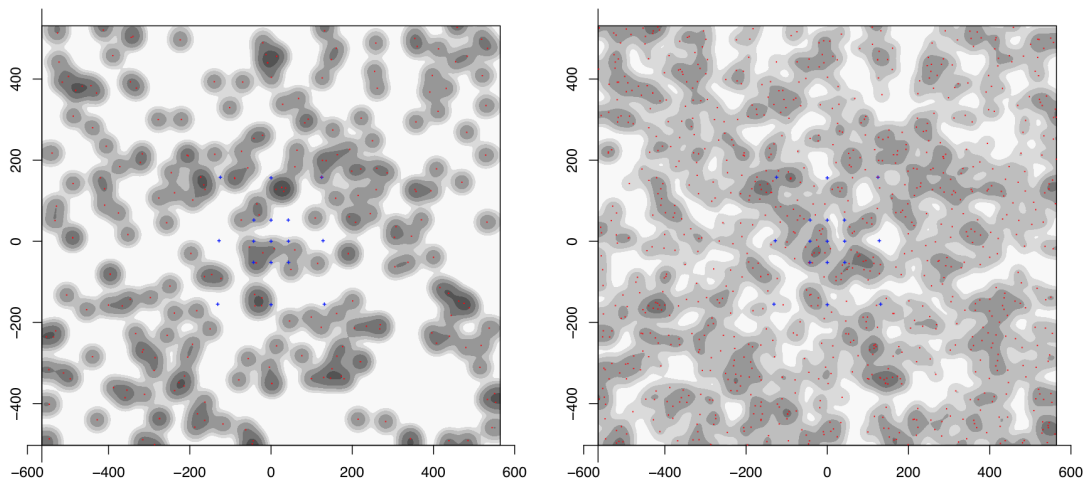


Figure 3.11. Database comparisons – ZM-comb. Left panel: MgII absorbers represented by red dots. Right panel: Available background probes represented by red dots. In both images grey contours represent the density distribution of the MgII absorbers smoothed with a Gaussian kernel (17 Mpc), and blue dots marks out a reference grid.

CHAPTER 3

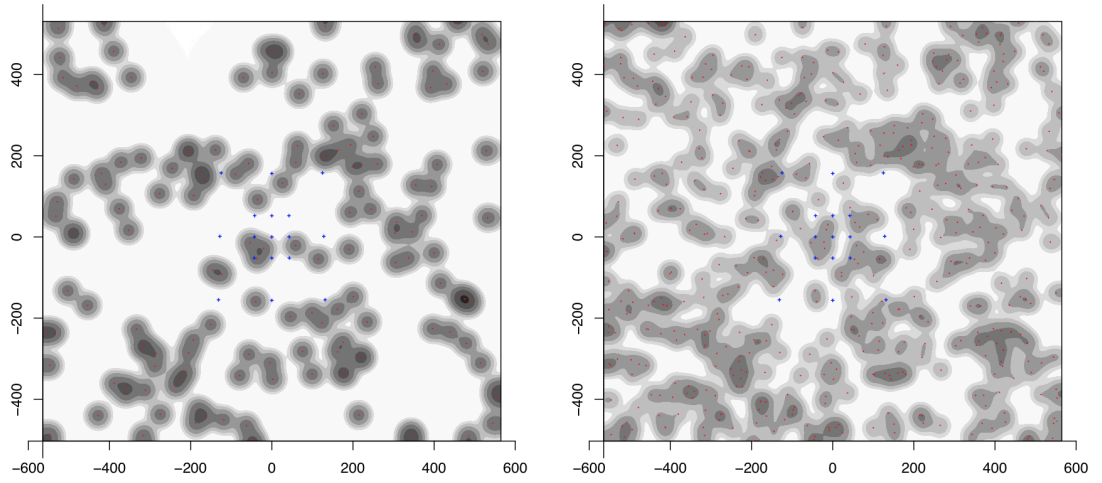


Figure 3.12. Database comparisons – R-field-all. Left panel: MgII absorbers represented by red dots. Right panel: Available background probes represented by red dots. In both images grey contours represent the density distribution of the MgII absorbers smoothed with a Gaussian kernel (17 Mpc), and blue dots marks out a reference grid.

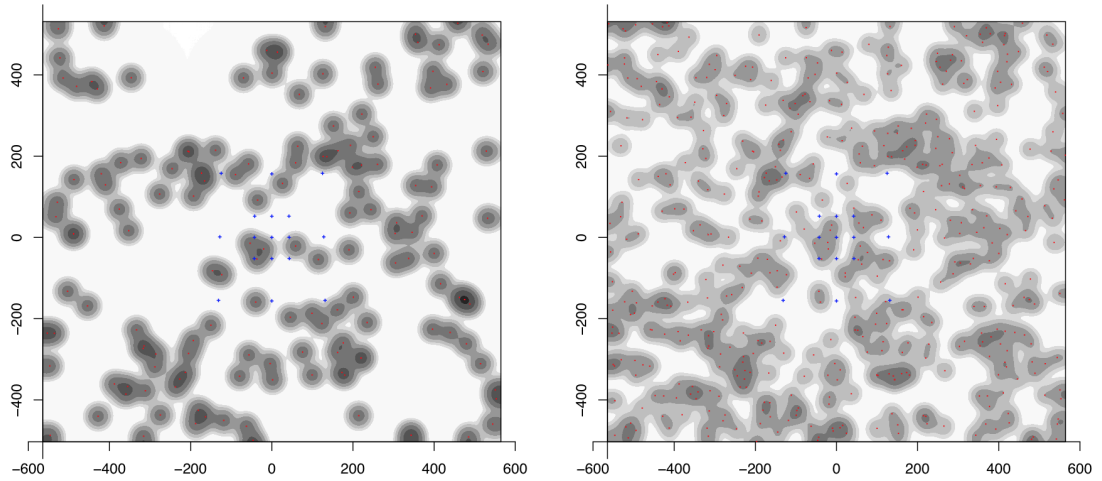


Figure 3.13. Database comparisons – ZM-field-all. Left panel: MgII absorbers represented by red dots. Right panel: Available background probes represented by red dots. In both images grey contours represent the density distribution of the MgII absorbers smoothed with a Gaussian kernel (17 Mpc), and blue dots marks out a reference grid.

CHAPTER 3

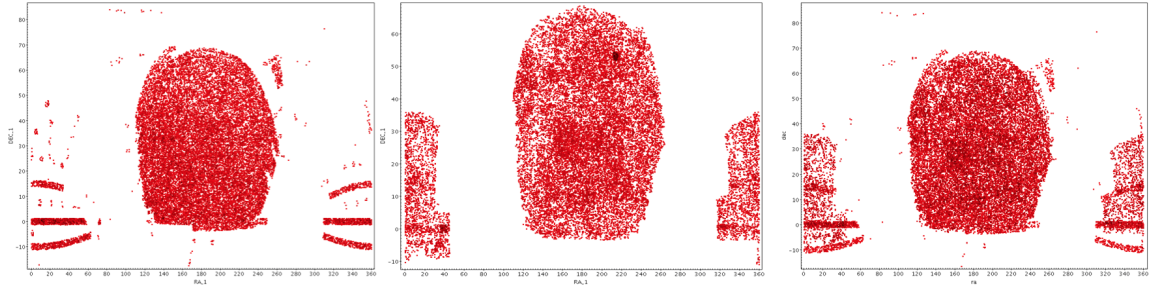


Figure 3.14. Topcat plots of the QSO distribution across the whole sky in the Z&M databases. Left panel: ZM-dr7. Middle panel: ZM-dr12. Right panel: ZM-comb. The dark and light patches indicated the non-uniformity in the databases.

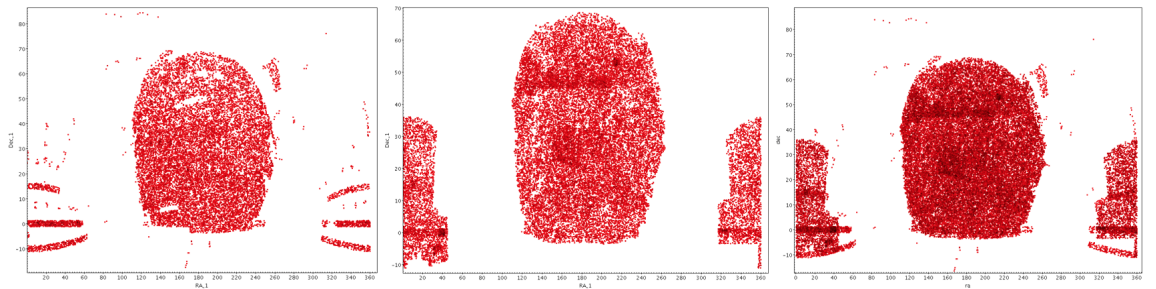


Figure 3.15. Topcat plots of the QSO distribution across the whole sky in R16 databases. Left panel: R-dr7. Middle panel: R-dr12. Right panel: R-comb. The dark and light patches indicated the non-uniformity in the databases. Note the large gaps in R-dr7 in particular.

CHAPTER 3

and because of this it is used preferentially to the other MgII databases. In fact, a slight preference is given in general for the Z&M databases, and this is because they are, in general, more complete than the R16 databases. One reason for this is that Z&M probe to much lower signal to noise ratios (SNR) of four and two for the $\lambda\lambda 2796, 2803\text{\AA}$ MgII lines, respectively. Whereas R16 only probe to a SNR of six and three for the $\lambda\lambda 2796, 2803\text{\AA}$ MgII lines, respectively. Also, R16 make more cuts to the data than Z&M to avoid the sky lines, explained in Section 3.2. Databases R-field-all and ZM-field-all show no difference in the MgII absorbers, which is to be expected since the same selection of paired absorbers is made for both databases. ZM-field-all will regularly be used as a second step in analysis of LSS in the MgII images and will be used to test how convincing the absorbers are in the other, larger, databases.

Part way through the course of this work, a minor problem was discovered concerning the DR12 databases. It appears that the R code had been dealing with long integer identifications of individual objects by splitting the long integer into two halves and treating a single object as two separate ones, essentially duplicating the number of objects. The problem was dealt with by using a `unique()` command in the MgII software and any MgII absorption plots previously made have been reproduced using the revised version of the software. Figure 3.16 provides a visual comparison of the difference between the old MgII absorption plots, with twice as many absorbers, and the new MgII absorption plots that use the revised version of the MgII software.

It should be noted that there are an additional two MgII databases provided by Dr S. Raghunathan which are generated from the new DR14 release from SDSS. These have not been included in this thesis as an initial inspection raised some concerns about the properties of these databases, and consequently more detailed work is being delayed until these concerns have been investigated thoroughly.

CHAPTER 3

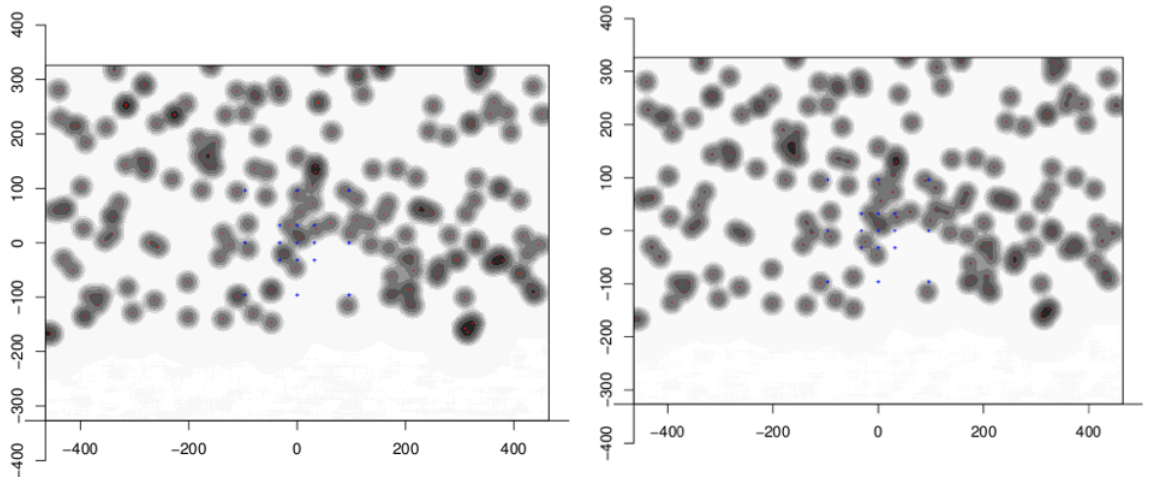


Figure 3.16. Comparison of MgII absorption plots produced from the old script, where the software generates twice the number of objects (left), and the new script with the duplication problem fixed (right). The visual difference is practically unnoticeable as suspected. Here, coordinates centred on the COSMOS field at $z = 0.73 \pm 0.1$ have been chosen. Red dots represent the MgII absorbers and grey contours represent the density distribution of the MgII absorbers, with contours increasing by a factor of two, smoothed using a Gaussian kernel (10 Mpc). The blue dots outline a reference grid, see Chapter 3.4 for further details of producing the MgII images.

3.4 The Software

The software used throughout the course of my work this year was provided by my supervisor Dr R. Clowes. It is written in R, R Core Team (2019). The software is responsible for producing all of the MgII plots that are used in the main body of analysis, and providing information on the background probes and the MgII absorbers in the images. I will outline the main steps of the software and elaborate on important aspects of the software such as kernel smoothing and flat-fielding.

Reading in the files Six separate software files are read into the main MgII software which are responsible for: converting RA and Dec values into tangent plane coordinates; converting tangent plane RA and Dec coordinates to approximate proper coordinates (units in Mpc) using only the central redshift of the slice; dividing a density image by its mean; reading in all of the MgII databases; defining the field for MgII analysis; and loading the SMICA CMB data.

Databases The databases which are described in Section 3.3 are read into the software. Combined databases are defined here, as well as standardised field names. Note, a problem that was encountered part way through the course of this year was that one of the R functions (`readFrameFromFITS`) was splitting up individual long integer entries into two separate entries – essentially duplicating the data. This problem was subsequently avoided by creating a final subset that only allows for unique entries of the MgII absorbers.

Smoothing and contours A Gaussian kernel is used to smooth the MgII absorbers in the images produced by the software to highlight the connectivity between points making it easier to make visual judgements on the results. The kernel smoothing essentially produces the density image by smoothing and adding. Each MgII point is smeared out by the kernel and then at each

CHAPTER 3

pixel the separate contributions are summed. The contour levels increase by factors of two. The raw MgII data simply comprises specific point locations of background probes and the MgII absorbers. Note, a single background QSO may contain more than one MgII absorber. In order to create an image that can be used for analysis, the Gaussian kernel smoothing scale is applied to the MgII absorbers to highlight connectivity between points. Since the images are scaled up to present epoch, proper distance values, the smoothing scale is affected by the redshift of the image. Through trial-and-error it was found that following a simple criterion for smoothing scale as a function of redshift was sufficient for allowing images in varying redshifts to have similar visual effects from smoothing:

$$\sigma = 10z + 3 \quad (\text{Mpc}) \quad (3.1)$$

As this is only a linear relationship it could not be used for large values of z . However, it does produce images that are sufficiently consistent for the requirements in this work since the redshifts dealt with do not exceed large values (in this work $z < 1.5$).

Offsets The offsets are what define the image size; they are used to extend the specified field location by a specified amount (in degrees). The standardised offset values for (N, E, S, W) are (5, 8, 5, 8)°. Quite regularly these values may be doubled or even tripled in order to achieve a greater FOV, but it is important to note that this is not the same as doubling or tripling the actual FOV as projection effects on a sphere will distort the image, especially so in larger images and towards large values of Dec.

Defining field and reference grids A separate file which defines the field location is read into the main software. In it, the RA and Dec coordinates are specified, the redshift is specified, as are the near and far values of the redshift slice, and the parameters of the two blue, dotted reference grids are

CHAPTER 3

defined. All of the parameters within the file are adjustable. The two blue, dotted reference grids were originally defined such that the small, dotted, blue square roughly covers 2 deg^2 (approximately the same size as the COSMOS field) and the larger, dotted, square roughly three times this size. However, as just mentioned, varying values of declination will mean that the reference grid will not necessarily always be 2 deg^2 . In fact, at higher declination the reference grids will be smaller since the scaling is proportional to $\cos(\delta)$.

Tangent-plane coordinates The points taken from the sphere in RA and Dec coordinates are converted to tangent-plane coordinates, and then limited to a rectangle. Plotting tangent-plane coordinates has the effect of slightly distorting the real image but on small enough scales the effect is negligible. For the large MgII fields, when offset values are doubled or tripled, the effect of warping may be a little more problematic.

Scaling to proper size The aim of the work presented here is to assess the potential of MgII absorbers as a tool for cosmology, and in particular the LSS at early epochs. Since many of the structures that will be looked at with the MgII method will be non-gravitationally bound (continuing to expand at a rate corresponding to less than or equal to the expansion of the universe), it is beneficial to scale the images to present epoch values to indicate how large the structures would be at the present time, given free expansion, and to allow comparison with other structures at different redshifts that are also freely expanding.

Determine background probes and corresponding MgII absorbers

The background probes which are selected must fall within the field boundary specified in the software and have redshifts greater than the far value redshift chosen to look for MgII. This also ensures the QSOs are in fact background

CHAPTER 3

QSOs and not field QSOs. Additionally, all QSOs that are known to be broad absorption line QSOs (BALs) are excluded. Next, a series of conditions are applied to the MgII absorbers so that the features blueward Ly- α are avoided, as well as the CIV emission line and sky lines. These conditions may already have been dealt with within the databases themselves but a cautionary step is taken to be certain. Within the MgII absorption selection process are adjustable settings on the equivalent width limits which are particularly useful for comparing results in strong and weak absorbers. The standardised values for the limit on rest-frame equivalent widths are $0 \leq W_\lambda \leq 10 \text{ \AA}$.

Flat-fielding The ability to assess LSS of the universe is fundamentally reliant on the availability of background QSOs. Since the distribution of QSOs in the universe is not uniform, where there is an excess of QSOs in a particular area, compared with the mean, it is more likely that MgII absorbers will be found here, than in a region of low QSO density. One way to deal with this is to use flat-fielding, which works by dividing the MgII density image by the background probes density image.

Creating the images The MgII software produces six images altogether. These are: the smoothed image of the available background probes represented by red dots and grey density contours; the smoothed image of MgII absorbers represented by red dots and grey density contours; the smoothed and flat-fielded image of MgII absorbers represented by grey density contours and available background probes represented by red dots; an image of the CMB data from SMICA; an image of the CMB data overlaid onto the smoothed image of MgII absorbers represented by red dots and grey density contours; and an image of the CMB data overlaid onto the smoothed and flat-fielded image of MgII absorbers represented by grey density contours and the available probes represented by red dots. Each image is scaled to proper distance,

present epoch values. The CMB plots are very interesting as they have the potential to highlight links or correlations of temperature with LSS. In fact, this is one of the goals for future application of the MgII method. In all images east is right and north is up.

3.4.1 Bootstrapping

Bootstrapping is a common method for assessing the properties of a given sample, and can be used to assign levels of significance to the original data. For the purpose of this work, a type of bootstrapping method, a ‘shuffling’ algorithm, has been created to be used for qualitative assessment of the MgII images. The bootstrapping/shuffling algorithm works via the following steps. Firstly, following the same steps in the main software, the MgII databases are read into the shuffling file and the specified FOV is defined. Each MgII absorber has a specified RA and Dec, and those absorbers that belong to the same background probe (multiple absorbers per probe) will share RA and Dec values. A sequence is produced using the `seq()` function in R which generates a set of numbers that increase in integer values from 1 to N , where N is the number of unique positions (RA, Dec) values, i.e, multiple absorbers belonging to the same background probe remain as a single unit. The `sample()` function in R is then used to shuffle the numbers in the generated sequence. The new, shuffled, sequence reassigns the RA and Dec values of the MgII absorbers within the specified field while retaining RA and Dec as a unit. This has the effect of assigning a MgII absorber, or a unit of MgII absorbers, to the position of a different background probe. The RA and Dec values are then assigned present epoch, proper distance, tangent-plane coordinates, as usual.

Since the shuffling method used here generates the MgII images, assessing the shuffled images has the same shortcoming as assessing all MgII images, this being, they are only qualitative, by eye, assessments. For the future it will become more

CHAPTER 3

important to investigate ways in which to assess the MgII images quantitatively, and draw meaningful statistical inferences from the MgII method. Another shortcoming is the shuffling algorithm only shuffles in RA and Dec, not redshift, which means the shuffling potential is restricted and it may make it difficult to fully erase large structures. Also, multiple absorbers were kept as a unit to avoid the appearance of more absorbers in the shuffled images. However, an improved method would allow for absorbers to be paired differently which would increase the shuffling potential. Finally, a shortcoming not just of the shuffling algorithm but of the published MgII databases on the whole, is that the total potential background probes for MgII systems are not kept in the MgII databases. Over 100 000 QSOs were tested for MgII in the DR7 databases and over 200 000 in the DR12 databases, yet the number of background probes remaining in the MgII databases, subject to SNR criteria, is between 20 000 - 65 000. Therefore, if all the potential QSOs were kept in the MgII databases then the overall shuffling potential would be increased as the number of potential background probes is increased. Furthermore, the shuffling algorithm would be more realistic as it would take into consideration the overall number of potential, available background probes.

The shuffling algorithm created in R is used to make qualitative assessments of the likelihood of producing an image that has similar properties to a specific result obtained from the MgII software. For example, if real data produces a MgII image with a large, dense region of MgII absorbers, the shuffling algorithm can be used to test if a large, dense region of MgII absorbers can be reproduced, or whether the feature can be erased. The assessment of MgII images is done by eye, but in due course ways will be investigated to assess the MgII images objectively. See Chapter 5 for a discussion on the future plans for the MgII method and the potential improvements to the shuffling method.

3.5 Cluster and Supercluster Candidates

Extensive work has been done in the Cosmic Evolution Sky Survey (COSMOS) field to reveal the precise structure of galaxies and clusters in fine detail, see Guzzo et al. (2007), Söchting et al. (2012), Iovino et al. (2016), from here on-wards referred to as G07, S12 and I16. In particular, the work done by S12 provides a substantial catalogue of nine galaxy structures in the COSMOS field at intermediate to high redshifts. Two of these structures have been selected for further study with MgII analysis based on their appropriate redshift.

The COSMOS field is a 2-deg² field located in the northern hemisphere centred on the celestial coordinates: RA +150.11°, Dec +2.21° (J2000). A huge collaboration of more than 200 researchers provide multi-wavelength measurements across the whole range of the COSMOS field and up to $\sim 75\%$ of the age of the universe. Observations are collected from ground-based and space-based telescopes from all over the the world, making the COSMOS field one of the most well-studied areas across the entire sky. The purpose of COSMOS is to probe the galaxy content, understand the structure and evolution of galaxy formation from small kpc to orders of Mpc scales, and to make predictions about the greater picture of our Universe and perhaps even constrain the values of the cosmological parameters.

In addition to the two cluster candidates selected from S12, we also aim to run the MgII analysis on four more candidates (making six in total) chosen from the literature. Candidates were prioritised based on a set of criteria including: redshift (preferably between the limits $0.3 < z < 2.2$ from MgII-redshift relation, but in particular, redshifts > 0.6 since we are primarily interested in the higher redshift regions); data available; images; opinion on the quality of data and information available on the structure (this is a vague criterion which required a general judgement on a particular paper as to whether the structure candidate seemed worth investigating); abundance of information (for instance, are there additional papers

CHAPTER 3

or follow-ups from the first discovery?) and interesting additional features that may make the structure worth investigating. Table 3.6 lists the six structure candidates chosen for MgII analysis, along with some general information about each one.

Target	Survey	RA (J2000)	Dec (J2000)	z_{mean}	Notes
1	COSMOS	150.12	2.21	1.12	Double Layered
2	COSMOS	150.12	2.21	1.27	*
3	ORELSE	241.01	43.32	0.90	Associated QSOs
4	Lynx	132.27	44.54	1.27	Associated QSOs
4	Planck SZ	215.41	38.35	0.76	SZ Cluster
6	CFHT Grens	204.50	28.10	1.10	Associated cluster

Table 3.6. The six cluster candidates selected for MgII analysis. * This particular redshift appears in various literature beyond the COSMOS field, Nakata et al. (2005), Clowes & Campusano (1991) and Clowes et al. (2013) which potentially makes it an interesting structure to study. Note, Target 6 was originally detected as a QSO group and then later more work was done by an independent author who found a chain of associated clusters, apparently within the QSO group.

Chapter 4

MgII Analysis for Known High z Structures

This Chapter presents the MgII analysis of the six selected target clusters/superclusters. For each target a small literature review will be provided and then MgII analysis will follow. The first two supercluster candidates that will be reviewed in this Chapter are those from Söchting et al. (2012) (hereafter S12) located in the COSMOS field. Here, I will briefly outline the details of this paper to be used in reference to the following Sections.

Background

S12 used the COSMOS LSS data presented by Scoville et al. (2007) combined with the multiwavelength COSMOS catalogue providing accurate photometric redshifts from Ilbert et al. (2009) to generate a cluster catalogue of 1780 structures, with $0.2 < z < 3.0$. Note, a lower redshift limit was set to ensure that the full structure is visible in the COSMOS field, otherwise, structures would extend well beyond the walls of the COSMOS field at low redshifts.

The distribution of i band magnitudes in the COSMOS catalogue highlights a depth coverage bias in the data, i.e., low redshift galaxies present a much greater

CHAPTER 4

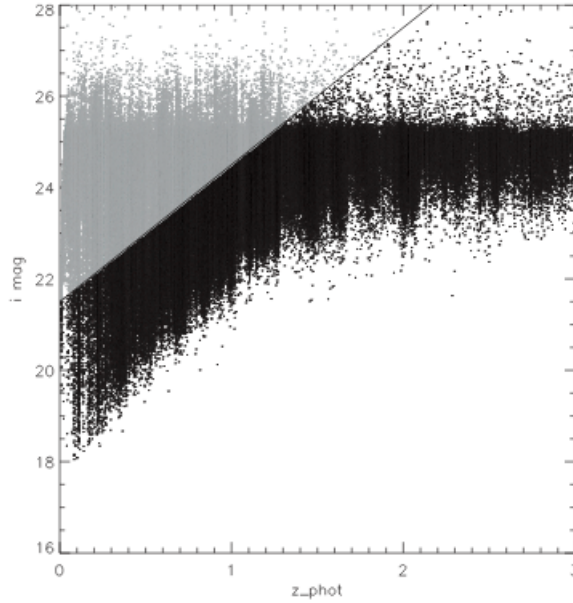


Figure 4.1. Figure taken from S12. Distribution of I-band coverage as a function of redshift. All objects beyond the cutoff limit (marked by a solid line) are coloured grey.

depth of coverage than the high redshift galaxies. To compensate for this, S12 restricted the data in magnitude via the following function limit.

$$i_{AB} < 21.5 + 3.0 \times z_{phot} \quad (4.1)$$

Thus, after equation 4.1 was applied, the input data was essentially homogeneous, as demonstrated in Figure 4.1. Beyond redshift of ~ 1.3 the depth of the coverage is declining, likely due to the magnitude limit of the COSMOS data, and so the function limit becomes inconsequential.

S12 divided the data into overlapping (by 50%) narrow photometric redshift slices; $\Delta z = 0.02(1+z)$. The overlap is to account for structures that may sit on the border of two neighbouring redshift slices. Then, Voronoi tessellation was applied to the data in each redshift slice which essentially provides information on the number density at each particular point corresponding to a galaxy. A limit was set such that the algorithm detects density peaks in the data greater than twice that of the mean

CHAPTER 4

density and, in addition, connected to a minimum of eight other cells exceeding the density limit. Structures attaining to the algorithm's requirements were then categorised into cluster candidates. Cluster candidates from each redshift slice were merged together if there is a minimum of eight common members between them. In a way, this method represents a hierarchical process of locating superclusters and has the effect of avoiding the situation in which a group is considered a member of a rich cluster when it is in fact just a close neighbour. Additionally, S12 showed that this method of detecting superclusters also generally avoids any severe fragmentation of supercluster candidates. Nine supercluster candidates were found using this technique, three of which were already documented superclusters.

I will briefly outline some of the main conclusions regarding the characteristics of the group and cluster sample data investigated by S12. As may be expected, the redshift distribution of groups and clusters indicates LSS throughout, even in the high redshift end where there is a steep reduction of data at $z \sim 1.3$ due to the limiting depth coverage of COSMOS, see Figure 4.2. An investigation of richness distribution across redshift also indicates the same property of a strong decline at a redshift of $z \sim 1.3$. In the case of the richness distribution, the data could imply that the richness of clusters decreases with redshift, i.e., strong clusters and LSS are almost negligible at early epochs. However, this would likely be a false conclusion as the richness of clusters is increasingly underestimated with increasing redshift. Unfortunately, the magnitude limit of COSMOS makes it difficult to draw firm conclusions regarding the LSS at redshifts beyond $z \sim 1.3$. Until further spectroscopic masses of groups and clusters are measured at higher redshift there is no certainty given here on how the LSS changes in redshift. It is clear that the dominating feature in the richness distribution across redshift is the abundance of small groups and poor clusters throughout all redshifts in accordance with the standard cosmological model, see Figure 4.3.

CHAPTER 4

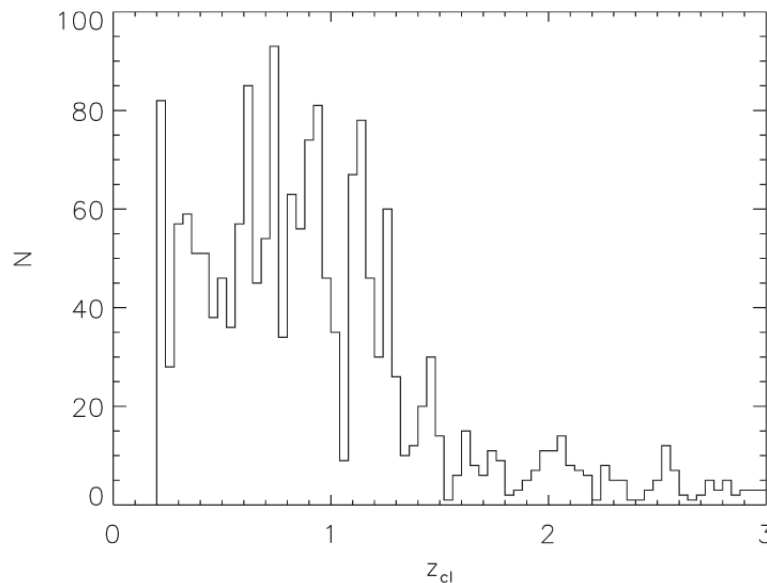


Figure 4.2. Figure taken from S12 showing the redshift distribution of the groups and clusters. The fluctuations of peaks indicates LSS throughout the full area of the COSMOS field.

While investigating the luminosity distribution of the groups/clusters in the data set, S12 recognised that, similar to the richness distribution, the luminosity distribution can be biased beyond $z \sim 1.3$. A common method of calculating a cluster luminosity is to simply add together cumulatively the luminosity of the individual galaxies. However, as mentioned earlier, clusters at high redshifts are likely to be underestimated in their richness since the smaller, fainter galaxies within are missed. Therefore a different method is incorporated here: S12 selected the four brightest galaxies in a cluster as a tracer of the total luminosity in terms of the K-band luminosity, denoted L_4 . The distribution of cluster luminosity produces a curve that peaks at $L_4 = 5 \times 10^{11} L_{\odot}$ and spans three orders of magnitude. Despite the limiting coverage of COSMOS, S12 were able to conclude that, since the peak luminosity of the groups/clusters in their catalogue remains almost constant with redshift, formation of the most luminous cluster galaxies must have taken place early on in the

CHAPTER 4

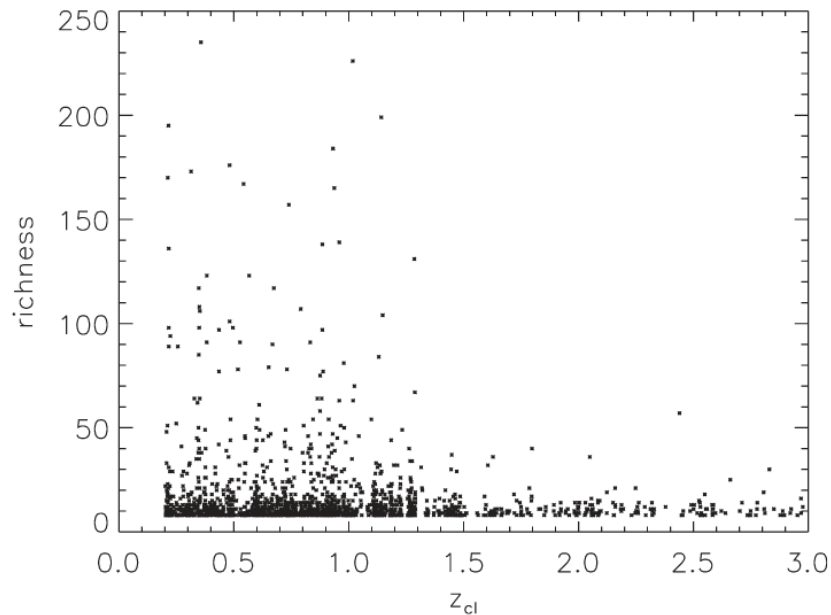


Figure 4.3. Figure taken from S12 showing the richness distribution of the groups and clusters throughout redshift. There is a strong drop off at $z \sim 1.3$ indicative of the magnitude limit of COSMOS.

evolutionary stages. Similarly, the distribution of the luminosity of groups/clusters with respect to their richness indicates that the most massive cluster galaxies form early on in the evolutionary stages. Finally, S12 went on to explore how the redshift distribution of groups and clusters is affected if a selection of only the brightest structures is made: two supercluster candidates at $z = 0.22$ and $z = 0.6$ disappear, indicating that these two pseudo-superclusters comprise a large quantity of faint galaxies.

In addition to studying richness and luminosity characteristics of the group and cluster catalogue, S12 discovered some peculiarities relating to the density distribution of the structures. Firstly, some of the highest recorded densities belong to those whose richness is at the lower end. Ninety percent of these high-density-poor structures belong to the redshift peak $z = 0.21$, and those remaining are associated

CHAPTER 4

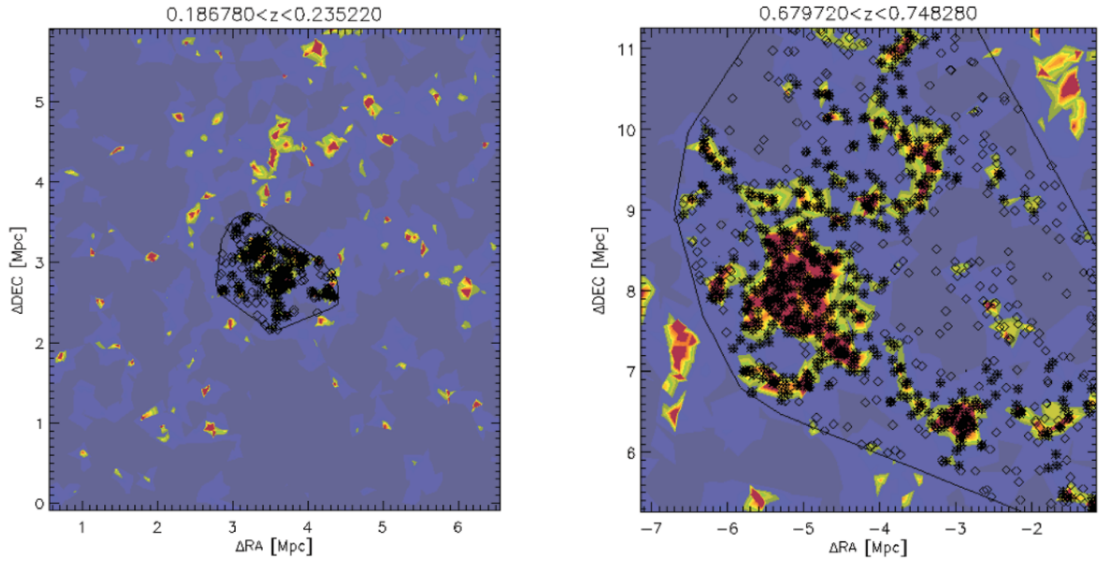


Figure 4.4. Figures from S12. The asterisks mark the member galaxies and the polygon outlines the subsequent cluster. Coloured contours map the density distribution. Left panel: a dense, compact, evolved cluster sample. Right panel: a cluster sample with strong filamentary substructure, likely still undergoing formation.

with the $z = 0.29$ and $z = 0.69$ peaks. In general, the high-density-poor structures consist of faint galaxies at low redshifts with evolved structures. Similarly, the rich structures almost all occupy the low-density region and coincide with the high redshift peaks. These high redshift, low-density-rich structures tend to inherit strong filamentary features and substructures and the low redshift, high-density-poor structures appear more compact; almost no internal structures apparent. This clear distinction between the two types of groups and clusters illustrates, almost, a ‘motion picture’ of the evolution of structure formation in the universe travelling through redshift. See Figure 4.4 for an example of a high redshift cluster sample compared with a low redshift cluster sample.

I have included a general table of information on the two S12 cluster candidates that will be investigated here, see Table 4.1.

CHAPTER 4

z	Δz	Δz (Mpc)	RA 150+	Dec	Cluster Members	$\sum R$	\bar{n} (Mpc^{-2})
1.12	1.08 - 1.15	165.434	0.12869	2.23449	128	1989	21.6
1.27	1.25 - 1.30	108.310	0.10923	2.21829	84.0	1230	15.2

Table 4.1. Table of information on the two S12 supercluster candidates investigated. The first column, z , is the peak redshift of clustering. The second column, Δz , gives the redshift range in which the galaxy clusters are located, and the third column is the redshift range scaled to proper distance, present epoch Mpc. The fourth and fifth columns are the central coordinates of the cluster calculated from the midpoint in RA and Dec. The sixth column is the number of cluster members in the redshift range of the supercluster candidate. $\sum R$ is the cumulative richness of all the clusters in the supercluster candidate, i.e., the number of member galaxies in the supercluster. The last column, \bar{n} , is the mean number density of cluster members.

4.1 Target 1: COSMOS field at $z = 1.12$

S12 found a double-layered cluster concentrated on the redshift $z = 1.12$. The layers of the cluster are separated by only $\Delta z = 0.02$ which gives reason to believe that the layers are part of the same supercluster.

MgII Analysis

For the double-layered supercluster candidate in the COSMOS field documented by S12, we find that in our first test of MgII absorption detection centred on the COSMOS field, with a redshift thickness of $\Delta z = \pm 0.1$, there is a null detection, Figure 4.5. Notice that there are clearly background QSOs available, indicated by the red dots, in the COSMOS field, indicated by the smaller blue dotted square.

CHAPTER 4

Potential reasons for the null detection will be discussed here.

In Chapter 3.2 the effect of night sky emissions on the detection of MgII is described, including how both independent authors of the MgII databases, Z&M and R16, deal with this problem. Both Z&M and R16 find that galactic absorption from our galaxy, complicated sky line subtraction at long wavelengths, strong sky line emissions and the confusion between other metal line absorbers that mimic the MgII doublet (in particular, CIV doublet), all have the effect of reducing the ability to detect MgII absorbers. Massey & Foltz (2000) tested the effect of external emission/absorption features while obtaining spectra and they found at redshift $z = 1.12$, where the wavelength of the MgII doublet is approximately 5900 \AA , there is a broad, high-pressure sodium bump observed in the spectrum of the night sky. This feature is also seen in Figure 3.4 by Z&M where between 5500 \AA and 6100 \AA (corresponding to the MgII doublet at $1.0 \lesssim z \lesssim 1.2$) there is a broad, steep drop in completeness of around 50% from the average rate of completeness at the blue end to the most severe point in the drop. In addition to the high-pressure sodium, Z&M state that the reduction in sensitivity at the point at which the two SDSS spectrographs overlap can also be affecting the low level of completeness.

SDSS use two spectrographs – blue and red – that function at either end of the visible spectrum and join together at 6000 \AA . In SDSS I-II (Legacy survey, DR7) the red and blue spectrographs were less sensitive than in phase three of SDSS, where new spectrographs replaced the old ones. In Figure 4.6, taken from the SDSS website, the spectrograph throughput is plotted as a function of wavelength for both red and blue spectrographs. Notice at $\sim 6000 \text{ \AA}$ a visible dip in throughput is seen and this corresponds to the same type of dip seen in the redshift distribution of absorbers in the ZM-dr7 database (included in Figure 4.6 for comparison). The new red and blue spectrographs used in BOSS (DR12) were designed to be more sensitive to their corresponding wavelength so that the transition from red wavelengths to

CHAPTER 4

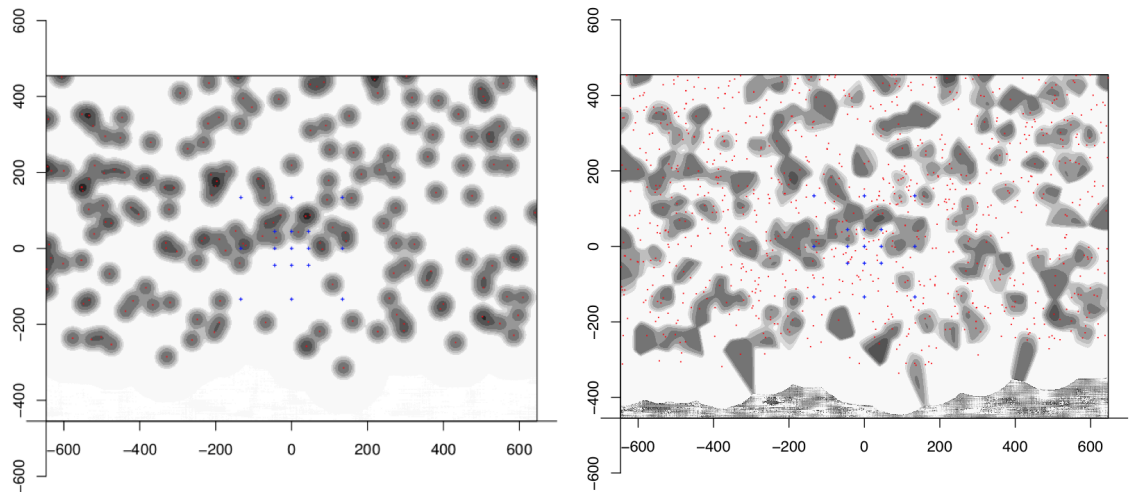


Figure 4.5. MgII images centred on the COSMOS field in the redshift interval $z = 1.12 \pm 0.1$ created using ZM-comb and smoothed using a Gaussian kernel (13 Mpc). Left-hand panel: red dots and grey contours represent the MgII absorbers. Right-hand panel: grey contours represent the flat-fielded MgII absorbers and red dots represent the background QSOs. In both plots the blue dotted squares outline a reference grid and the grey contours are increasing by a factor of two. Axes are measured in proper size Mpc scaled to the present epoch. Note the structure in an arc to the north of the COSMOS field.

CHAPTER 4

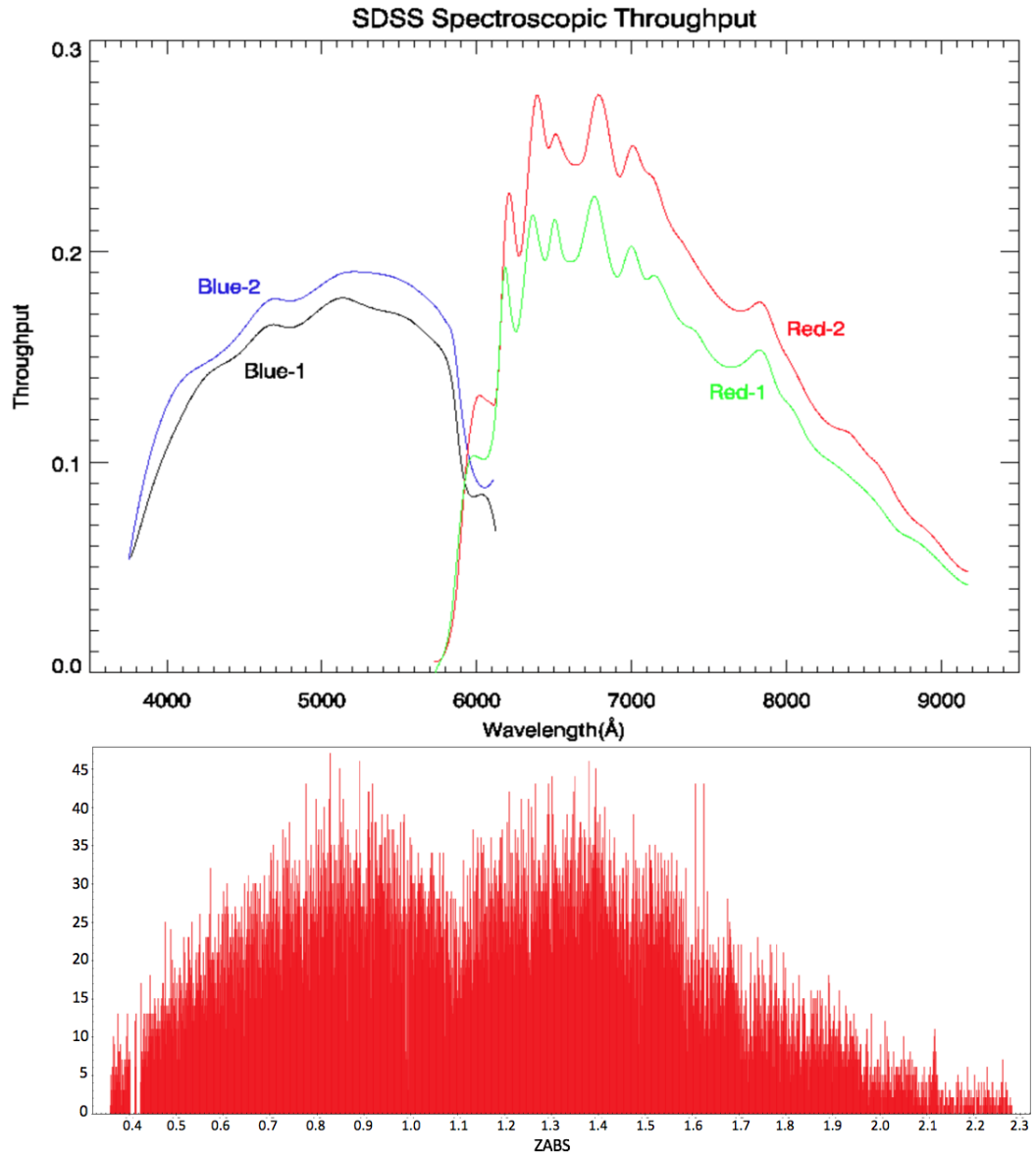


Figure 4.6. Top panel: figure taken from the SDSS website showing the throughput of the red and blue spectrographs used in the Legacy Survey (DR7). Bottom panel: redshift distribution of the MgII absorbers in ZM-dr7. Notice the broad dip in both plots that occurs at $\sim 6000 \text{ \AA}$ or at redshift ~ 1.1 .

CHAPTER 4

blue wavelengths does not cause a dip in completeness. Refer back to Figures 3.2 and 3.3 in Section 3.2 to see the difference in the redshift distribution of MgII absorbers in each of the databases. This means that when observing at redshift ~ 1.1 (or at 6000 \AA) the drop in the completeness, due to the low sensitivity of the spectrographs when they are working in their most extreme wavelength region, will make it harder to detect MgII absorbers. In conclusion, observing MgII absorbers in the redshift region $1.0 \lesssim z \lesssim 1.2$ will decrease the number of detections due to both the effects of the high-pressure sodium bump masking the spectrum and low sensitivity of the spectrographs. It is probably a redshift which should be cautioned for both of these reasons. Despite what has been mentioned, there are clearly still some absorbers detected. However, the reduction in absorbers makes it more difficult to assess the overall LSS in the redshift interval $z \approx 1.0 - 1.2$. Furthermore, the images that are produced by the software may be less secure if the sensitivity has already been reduced and there is masking from sky line emissions. In the case of the double-layered supercluster in the COSMOS field at $z = 1.12$, the results will remain less clear.

It may still be of interest to note the structure of absorbers arcing over the COSMOS field in the north (Figure 4.5). The concentration of absorbers here seems particularly dense. In addition, the absorbers in the arc arise in all of the combined databases (R-comb, ZM-comb, R-field-all and ZM-field-all from Table 3.2) and within the narrower redshift slice ($\Delta z = 0.12$) corresponding to 282 Mpc, see Figure 4.7.

The majority of the absorbers in the MgII field centred on the COSMOS field at redshift $z = 1.12$ have equivalent widths greater than $W_\lambda = 0.3 \text{ \AA}$. This, however, is to be expected since such a large fraction of the absorbers in the Z&M databases have equivalent width $W_\lambda > 0.3 \text{ \AA}$. The chain of MgII absorbers arcing over the small, blue, dotted reference grid corresponding to the COSMOS field could be

CHAPTER 4

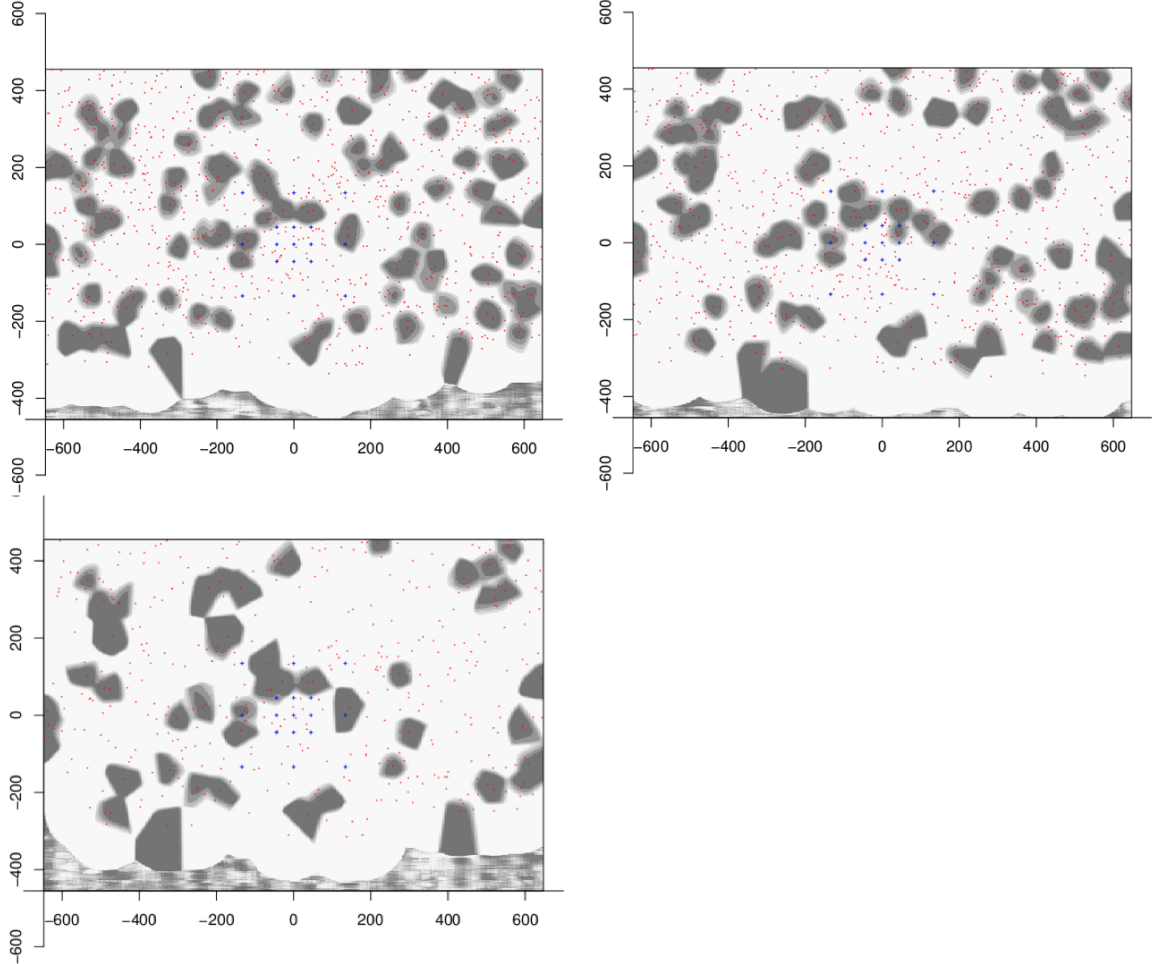


Figure 4.7. MgII images centred on the COSMOS field in the redshift interval $z = 1.12 \pm 0.06$. Grey contours increase by a factor of two and represent the density distribution of flat-fielded MgII absorbers, smoothed with a Gaussian kernel (14 Mpc). Red dots represent the background QSOs and blue dotted squares outline a reference grid. Axes are measured in proper size (Mpc) scaled to the present epoch. Top-left panel: created using ZM-comb. Top-right panel: created using R-comb. Bottom-left: created using ZM-field-all. Note the arc of absorbers to the north of the COSMOS field is present in all three combined databases.

CHAPTER 4

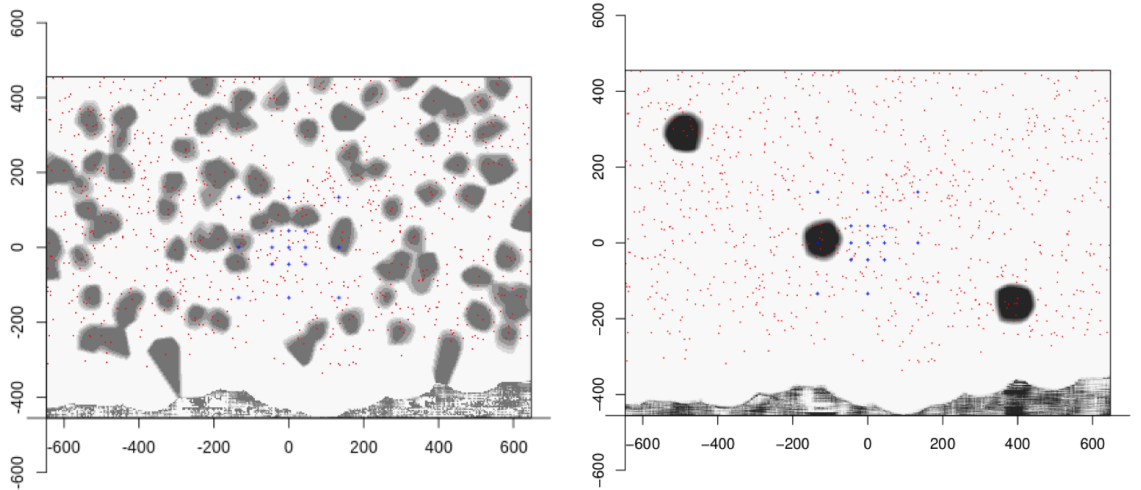


Figure 4.8. MgII images centred on the COSMOS field in the redshift interval $z = 1.12 \pm 0.1$ created using ZM-comb and smoothed with a Gaussian kernel (13 Mpc). Grey contours increase by a factor of two and represent the density distribution of the flat-fielded MgII absorbers. Red dots represent the background QSOs and blue dotted squares outline a reference grid defined in Section 3.4. Axes are measured in proper size (Mpc) scaled to the present epoch. Left panel: medium and strong absorbers in the field with equivalent widths $W_\lambda > 0.3$. Right panel: weak absorbers in the field with equivalent widths $W_\lambda < 0.3$. Almost all of the absorbers have equivalent widths greater than $W_\lambda = 0.3$.

CHAPTER 4

a real structure that is in association with the S12 cluster candidate. However, at present, it is unclear whether the chain of MgII absorbers to the north of the COSMOS field is in association with the S12 cluster candidate at redshift $z = 1.12$.

Lastly, the null detection in the COSMOS field at redshift $z = 1.12$ could be highlighting a false detection made by S12, or perhaps a misidentification of the redshift at which the cluster candidate is located. This early into testing the MgII method for LSS, it is difficult to be certain about the results obtained here.

4.2 Target 2: COSMOS field at $z = 1.27$

The supercluster candidate in the COSMOS field at redshift 1.27 documented by S12 is of particular interest since there are a number of additional structures documented at this same redshift: Clowes & Campusano (1991); Ohta et al. (2003); Nakata et al. (2005); and Clowes et al. (2013). In the future it will be interesting to explore the implications of having many documented structures at the same redshift and it could be investigated whether there is something special or significant about this specific epoch. Also, the possibility of connectivity between individual supercluster candidates at this redshift could be explored.

MgII Analysis

S12 found the supercluster candidate at $z = 1.27$ to span a very narrow redshift range, $1.25 < z < 1.30$. However, photometric redshift measurements often lead to uncertainty broadening, meaning that the confinement of this structure, and its substructure is not fully resolved. The MgII method provides accurate spectroscopic redshifts which can be used to provide finer detail of the substructure of superclusters. For target 2, the histogram of MgII absorbers across redshift in the field centred on the COSMOS field at $z = 1.27$, covering a FOV approximately 16 deg in RA and 10 deg in Dec, displays two distinct peaks, see Figure 4.9. The redshift range within

CHAPTER 4

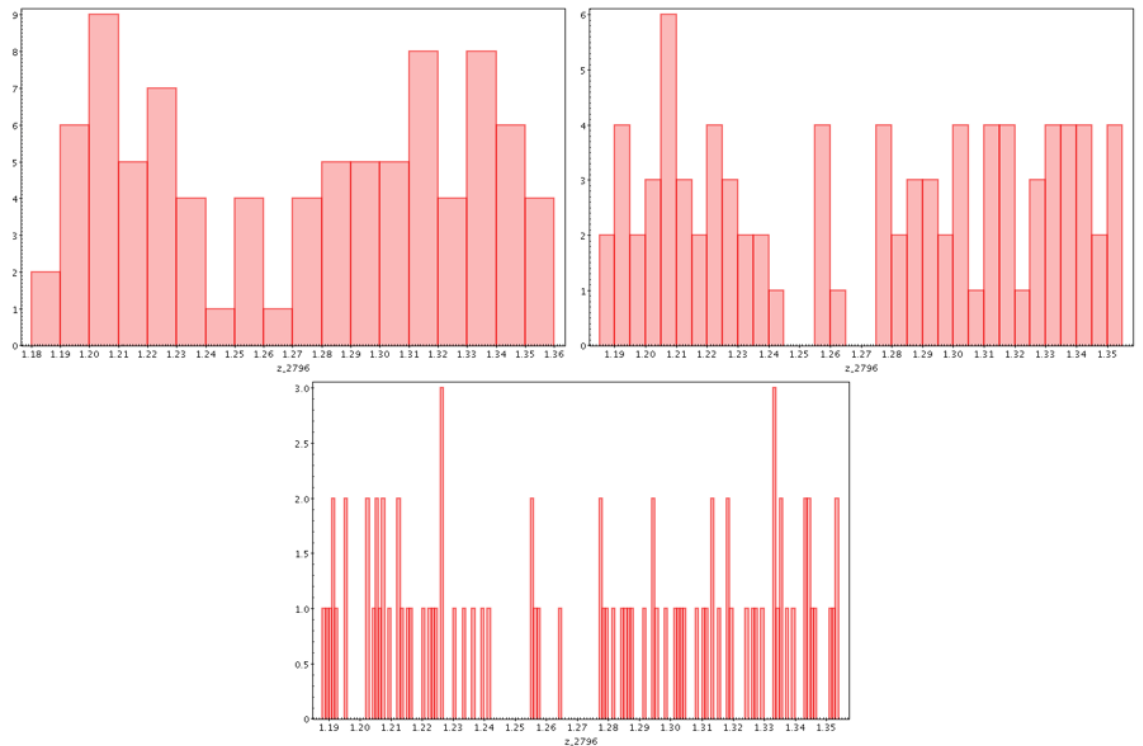


Figure 4.9. Histograms of the number of absorbers in redshift for the MgII image centred on the COSMOS field at $z = 1.27 \pm 0.08$ in the ZM-comb database. Note the bimodal distribution in all three images, reaching a minimum value around the central redshift. Top left panel: bin size of 0.01. Top right panel: bin size of 0.005. Bottom panel: bin size of 0.001.

CHAPTER 4

which this supercluster candidate is contained, according to S12, corresponds to a redshift ‘thickness’ of ~ 108 Mpc at the present epoch. However, here it is found that the distribution of absorbers in the MgII field drops to a minimum in the central redshift 1.27 and peaks either side at approximately $z = 1.21$ and $z = 1.33$. The histogram of MgII absorbers in redshift suggests that there are two main sheets of overdensity either side of a small, ~ 50 Mpc void. It is improbable that the supercluster candidate documented by S12 is contained at the exact redshift where the MgII finds the void, so perhaps the uncertainty broadening of the photometric redshift slices has the effect of blurring the two peaks into one density peak at the average redshift between $z = 1.21$ and $z = 1.33$. It has also been considered that the drop in MgII absorbers in the central redshift could be the result of a drop in completeness in the Z&M MgII databases which can be seen in Figure 3.4 in Section 3.2. Here, the completeness drops slightly between redshift 1.2 and 1.3, indicating it could coincide with the central redshift of this target at $z = 1.27$. By producing the same histograms for randomly selected areas of sky at the same central redshift it can be shown whether the distribution of MgII absorbers also creates the same bimodal feature as seen in the three histograms in Figure 4.9. Five fields were tested in the redshift range $z = 1.27 \pm 0.08$, corresponding to a redshift thickness of 282 Mpc in proper distance, present epoch values, and five histograms of the redshift distribution of MgII absorbers were produced to test whether the frequency of MgII absorbers dropped at the central redshift. Figure 4.10 shows the five histograms produced using randomly chosen test fields centred on redshift $z = 1.27$. Since none of the five randomly selected fields centred at redshift $z = 1.27$ showed any sign of a drop in completeness at the central redshift, then the distribution of MgII absorbers in the COSMOS field centred on redshift $z = 1.27$ is more likely to be a real result rather than a systematic error due to a drop in completeness from the Z&M databases.

CHAPTER 4

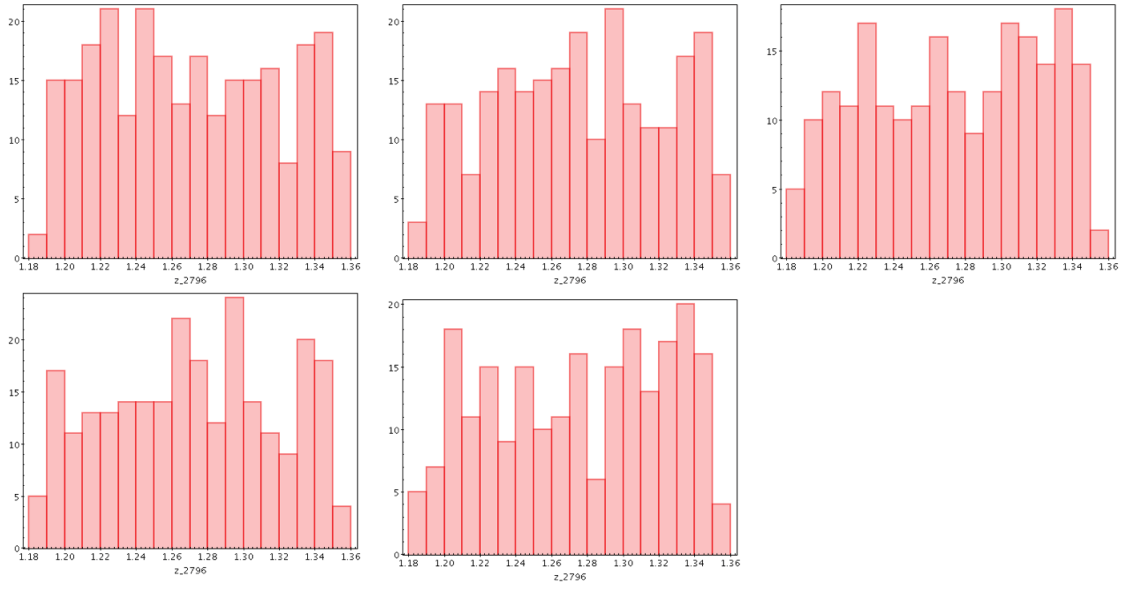


Figure 4.10. The redshift distribution of MgII absorbers in each of the five randomly selected fields in the redshift interval $z = 1.27 \pm 0.08$. In all of the fields there is no sign of a drop in MgII absorbers in the central redshift. All five fields were created using ZM-comb database.

CHAPTER 4

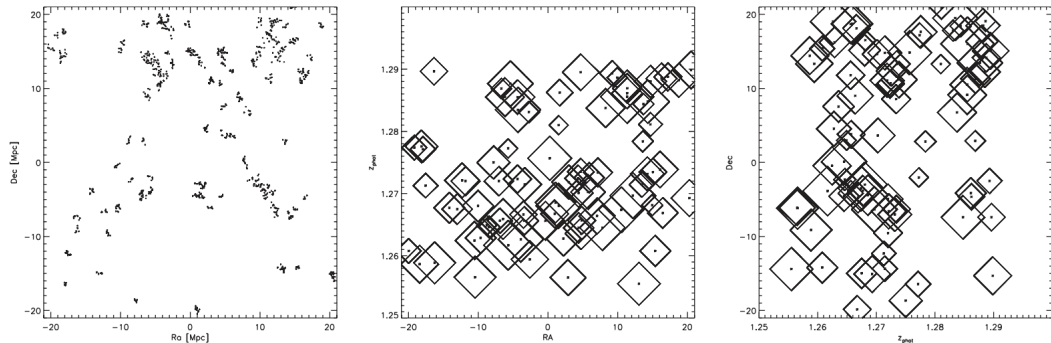


Figure 4.11. Supercluster candidate at $z = 1.27$ from S12. The left-hand panel shows the distribution of galaxies in the supercluster candidate. The middle and right-hand panels show the groups and clusters plotted against RA and Dec respectively. S12 did not classify this supercluster candidate as double-layered, however, there does seem to be some indication of a gap in the middle of the groups and clusters along the redshift axes.

S12 plotted the distribution of galaxies that are members of groups and clusters in the supercluster candidate and found there is significant filamentary substructure feeding into a common point, see Figure 4.11. The longest axis of the structure in RA and Dec extends up to 1.91° on the sky (267 Mpc at the present epoch) which is almost the full extent of the COSMOS field of view at the present epoch. The left-hand panel in Figure 4.11 shows the member galaxies in RA and Dec. Here, the filamentary substructure is clear: lines of galaxies feed into a common point. The longest axis travels from the south-west to the north-east, passing through the common point. In the middle and right-hand panel the structure is clearly confined to a thin slice of redshift. The empty regions above and below in the middle panel, and to the left and right of the right-hand panel, emphasise the confinement of the structure.

It is possible that the S12 cluster candidate could extend further; many large clusters form on scales 20 – 100 Mpc, see Einasto et al. (2011), but in other cases

CHAPTER 4

there have been documented structures on scales greater than 400 Mpc – e.g. Gott et al. (2005), Clowes et al. (2013) and Balázs et al. (2015). In fact, structures on these scales may be more common than previously thought. Due to the finite size of the COSMOS field, some supercluster candidates cannot be fully exposed, therefore, it is not only of interest, but of importance, to see if these structures do extend. The MgII plots centred on the COSMOS field at $z = 1.27 \pm 0.08$ with a field of view spanning $\sim 16^\circ$ in the RA and $\sim 10^\circ$ in the Dec, with a 15 Mpc smoothing scale, using databases ZM-comb, R-comb and ZM-field-all are shown in Figure 4.12. In each of the MgII plots in Figure 4.12 there are absorbers that cross through the COSMOS field indicating the the MgII method has detected the supercluster candidate that S12 found. The top two figures from Figure 4.12 show a visible overdense, clumpy region to the left of the COSMOS field which spans approximately 400 – 500 Mpc across RA and 200 – 400 Mpc in Dec (depending on which database is used). In the combined databases, leaving only absorbers in common to both independent authors, this clumpy structure is more refined and stands out against the sparse background, see Figure 4.12 (bottom-left panel).

Selecting absorbers using the box selection tool in TOPCAT (version 4.6-3), Taylor (2005), allows one to calculate a basic approximation to the density in the overdense region as compared with the density in the whole field. Firstly, the north and south offset values in the software were adjusted so that the size of the field of view remains the same but the field is shifted upwards to avoid the area where the SDSS data runs out – see Figure 4.13 and note that the COSMOS field centre appears much lower down. The rectangle selection was done by eye in TOPCAT; see Figure 4.14 for the image of absorbers showing the smaller rectangle selection of the overdense region. The overdensity inside the small rectangle contained 25 out of the 117 absorbers in the whole field. The rectangle covered an area of 0.115×10^6 Mpc² giving an average density of 216×10^{-6} Mpc⁻². The whole field covered an

CHAPTER 4

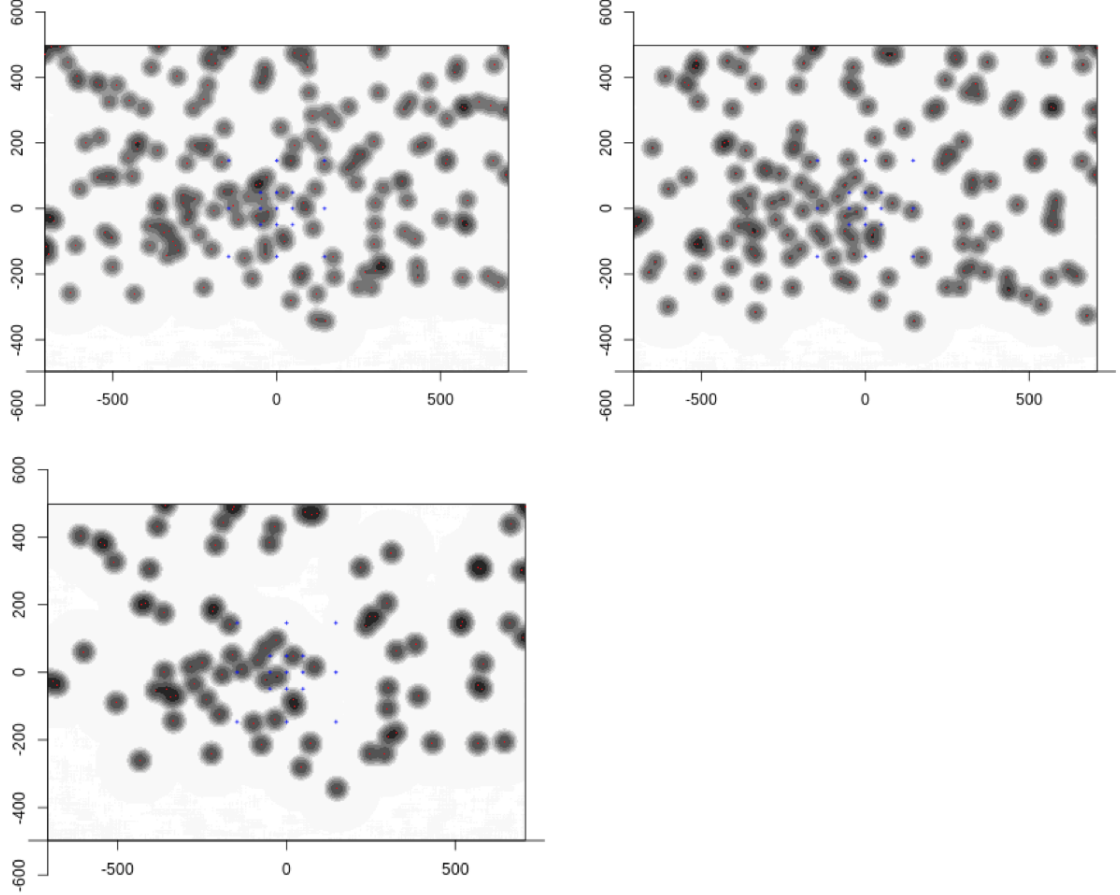


Figure 4.12. MgII images centred on the COSMOS field in the redshift interval $z = 1.27 \pm 0.08$ corresponding to a redshift thickness of 282 Mpc, scaled to the present epoch. Red dots represent the MgII absorbers and the grey contours, increasing by a factor of two, represent the MgII absorbers smoothed with a Gaussian kernel (16 Mpc). Blue dotted squares outline a reference grid. Axes are measured in proper size (Mpc) scaled to the present epoch. Top-left panel: MgII image created with ZM-comb. Top-right panel: MgII image created with R-comb. Bottom-left panel: MgII image created with ZM-field-all. The dense region of MgII absorbers to the left of the COSMOS field is present in all three combined databases.

CHAPTER 4

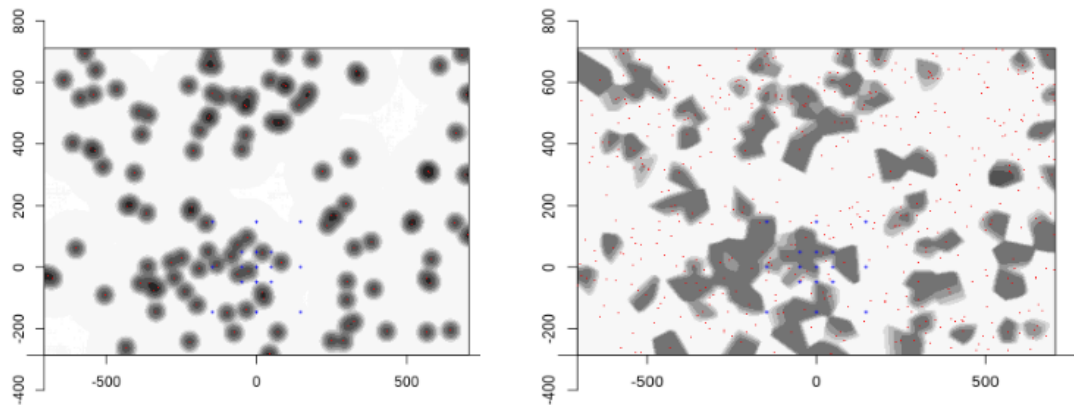


Figure 4.13. MgII images centred on the COSMOS field in the redshift interval $z = 1.27 \pm 0.08$, corresponding to 282 Mpc in the present epoch, created using ZM-comb and smoothed using a Gaussian kernel (16 Mpc). Left: red dots and grey contours represent the MgII absorbers. Right: grey contours represent the flat-fielded MgII absorbers and red dots represent the background QSOs. In both plots the blue dotted squares outline a reference grid and the grey contours are increasing by a factor of two. North and south offsets were adjusted to avoid the part of the field where SDSS runs out of data. Axes are measured in proper size (Mpc) scaled to the present epoch.

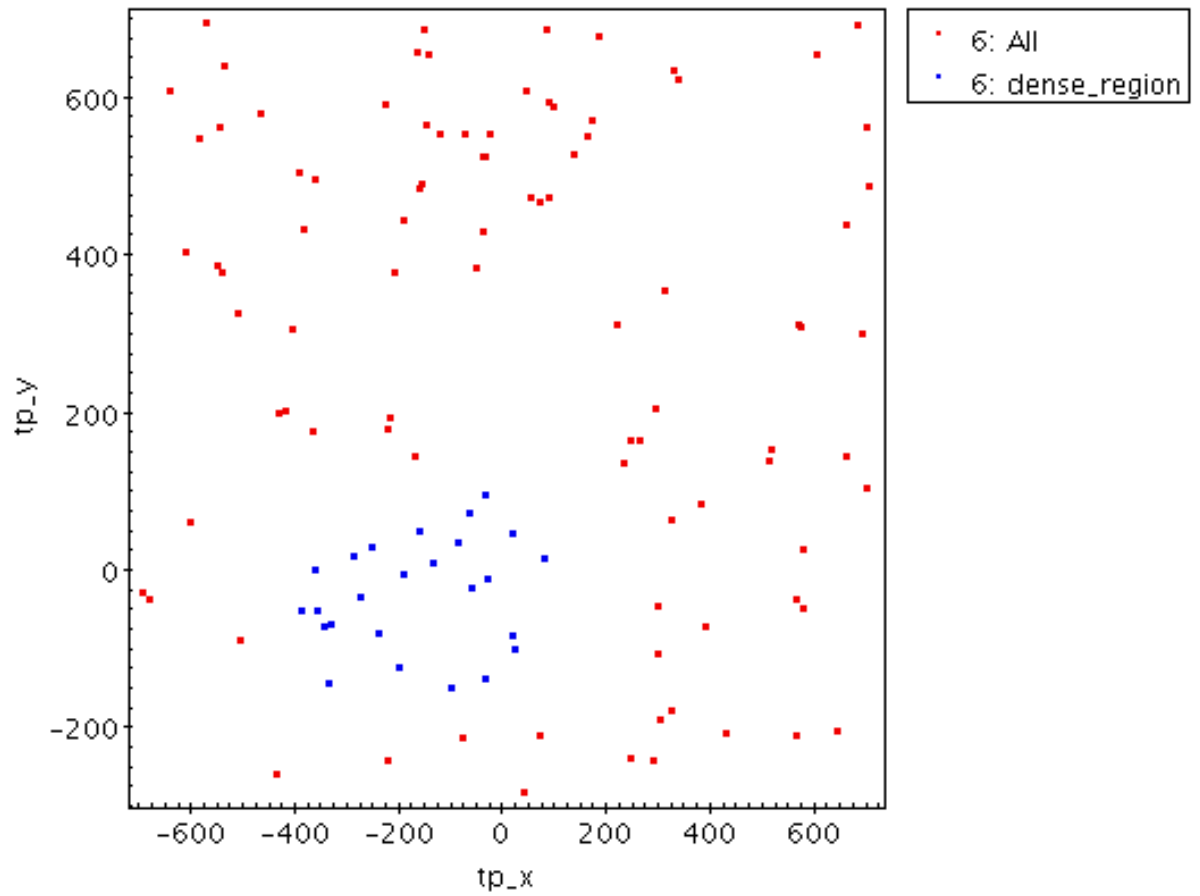


Figure 4.14. TOPCAT plot of the absorbers in the MgII field from Figure 4.13. The small selection containing blue points is showing the absorbers in the ‘clumpy’, overdense region.

CHAPTER 4

area of $1.37 \times 10^6 \text{ Mpc}^2$ giving an average density of $85.7 \times 10^{-6} \text{ Mpc}^{-2}$. Then, assuming Poisson distribution, and assuming also that the probes are roughly uniformly selected, the expected number of absorbers for the small rectangle selection is calculated and compared with the actual number of absorbers in the small rectangle selection. The overdense region produces a 4.81σ significance, implying that this result is physical and significant. However, it should be noted that the rectangular selection was a subjective selection, open to human bias, so slight variations in this result are to be expected had the selection been made differently.

The absorbers contained within the selected region of overdensity have been included in the histogram of absorbers across redshift to see if there is any correlation between the distribution of overall absorbers and distribution of absorbers in the dense region across redshift; see Figure 4.15. The absorbers in the dense region follow the rise and fall of the overall absorbers in the field. There appear to be two main sheets of overdensity with a small void at the central redshift $z = 1.27$. Thus, it is assumed that since the supercluster candidate documented by S12 is likely contained within the absorbers of the large structure in MgII, and this structure spans a redshift with two main peaks and a small central void, then the distribution of absorbers in the supercluster candidate will also, likely, follow this same pattern. Probing the inner structure of supercluster candidates with high-accuracy spectroscopic redshifts is a benefit of using the MgII method for studying LSS in the Universe.

Using the shuffling algorithm described in Section 3.4.1 can provide a level of confidence to the likelihood of observed structures or overdensities as one can compare how frequently large overdensities are produced by randomising. The obvious limitation to this method is that one has to subjectively define what looks like a structure or an overdensity. However, as this method is not being used quantitatively, it is reasonably effective to investigate how frequently large structures appear

CHAPTER 4

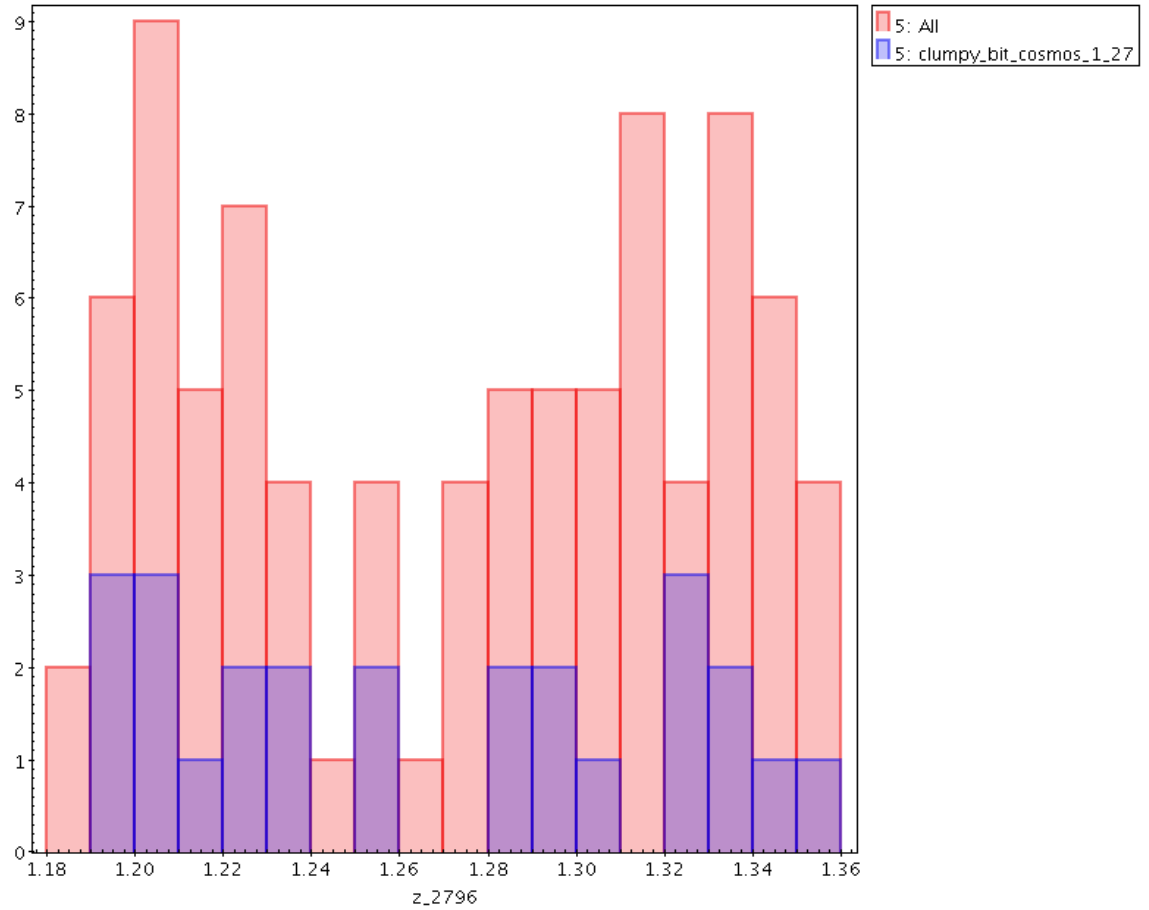


Figure 4.15. Histogram of the number of absorbers as a function of redshift for the MgII image centred on the COSMOS field at $z = 1.27 \pm 0.08$ in the ZM-comb database (from Figure 4.13) with a bin size of 0.005. Red bars: all absorbers. Blue bars: absorbers contained within the selection.

CHAPTER 4

in the shuffled fields by eye. It may also be important to note that the shuffling algorithm can often struggle to fully erase features if they are very strong. Additionally, the shuffling algorithm is only applied on two parameters: RA and Dec. As this method for analysis is only a simple, qualitative investigation, we do not find it imperative to amend this minor shortcoming of the algorithm immediately. In the future I plan to use an algorithm that can be more thorough and quantitative. In addition to the small shortcoming in the shuffling algorithm, using the paired databases (ZM-field-all) will increase the likelihood of a feature surviving the shuffling algorithm as the background probes are reduced but the ones in real structures will remain. The shuffling algorithm was looped 100 times on the field centred on the COSMOS field extending 16 deg in RA and 10 deg in Dec using ZM-field-all. Out of 100 plots there was one such plot, number 59, that reproduced a feature of similar calibre to the structure in target 4, this is seen in Figure 4.16. The rectangle selection method of calculating significance in overdensities is used on number 59 of the shuffle plots to calculate the significance of the number of absorbers in the small, dense area, compared with the number of absorbers across the whole field; the result is a 4.91σ significance. In addition, there were another eight images (nine in total) thought to produce features that were somewhat interesting. These tend to be small dense regions or reasonably well-connected filaments. However, by eye these are not as significant as the real structure or as the feature produced in number 59 of the shuffled plots. Bootstrapping methods are a technique used to understand sample data relative to the re-sampled data. In the case here, where a shuffling algorithm is used as the bootstrapping technique, only one image out of one hundred contained a feature similar to the structure in Target 4. The shuffling algorithm almost completely erases any sign of the large structure in target 4 suggesting that this structure is in fact real, and not the result of some error in the MgII method. The shuffling has therefore given confidence to the physical reality of the structure

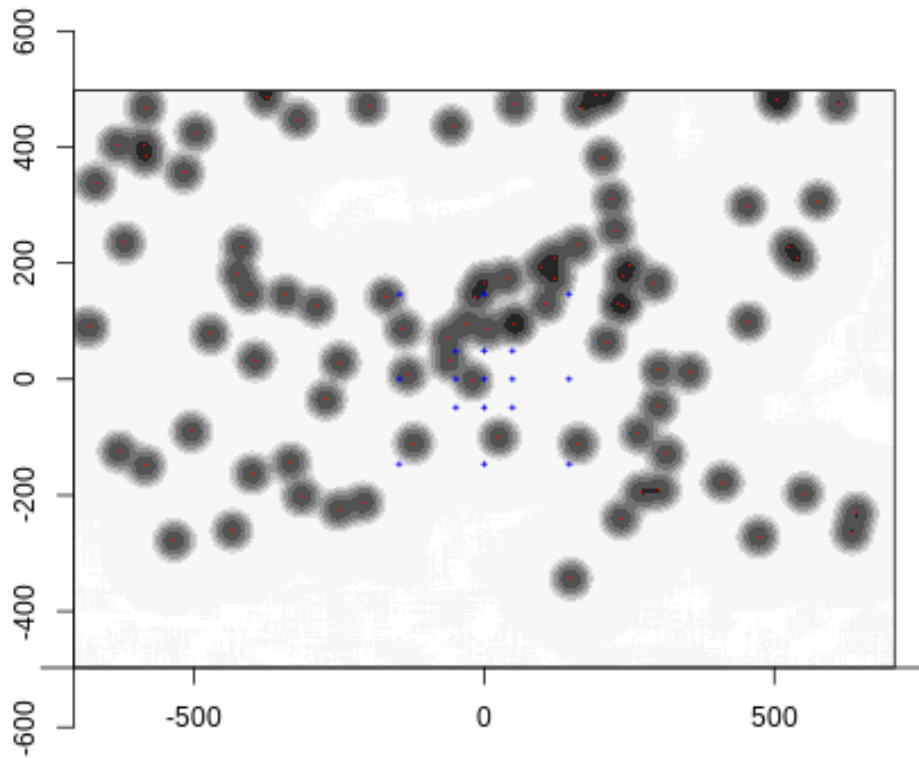


Figure 4.16. Number 59 of the shuffled plots. The lower region of the field, where the SDSS begins to run out of data, will not be affected by the shuffling algorithm since the algorithm changes the position of the MgII absorbers (as a unit if there are more than one along the LOS) to a different, existing QSO. Red dots represent the MgII absorbers and grey contours are increasing by a factor of two and represent the density distribution of the MgII absorbers which are smoothed using a Gaussian kernel (16 Mpc). Blue dotted squares outline a reference grid. Axes are in units of Mpc scaled to the present epoch. By eye, the chain of MgII absorbers starting from the centre of the field and travelling north-east appears to be something of interest. There is also a very prominent void north of the blue, dotted reference grid.

CHAPTER 4

in Target 4, although, care must be taken as it is previously mentioned that there are limitations to the shuffling algorithm used here.

To conclude Target 2 we find that the MgII method detects the supercluster candidate documented by S12. The MgII detection leads to a potential LSS to the westerly side of the COSMOS field reaching up to a minimum of ~ 400 Mpc in its longest length. It is likely that this overdensity is real since the combined databases emphasise the overdensity, as opposed to erasing absorbers in this region, and the shuffling struggles to produce images remotely similar to the real image. The overdensity detection is seen in all three databases (ZM-comb, R-comb and ZM-field-all) that were tested, improving the confidence in the detection of a LSS at this location. The methods used to test the LSS, while fairly simple, produce a 4.81σ detection in the overdensity calculation and only 1 out of 100 shuffled fields could produce an overdensity of similar order of size. The MgII method has probed the inner substructure of the absorbers in the wider field around the supercluster candidate by S12 and found that it spans a redshift range ~ 0.12 . Also, it was shown that the absorbers in the rectangle selection of the overdense region displayed a bimodal distribution, following the overall trend. Therefore it is probable that the absorbers in the S12 supercluster candidate span a greater redshift range than previously thought from S12.

4.3 Target 3: Supercluster at $z = 0.9$

The results for a high redshift supercluster in the Observations of Redshift Evolution in Large Scale Environments (ORELSE) survey are presented by Gal et al. (2008). The supercluster, Cl 1604, is one of the largest observed structures at redshift $z \sim 0.9$, containing many spectroscopically confirmed galaxies. Gal et al. (2008)

CHAPTER 4

(hereafter G08) provide accurate spectroscopic redshift measurements for 1138 objects in a field spanning $\sim 0.08 \text{ deg}^2$, making use of the data that is already available combined with new data from the Deep Imaging Multi-Object Spectrograph observations. Of the 1138 objects observed, 413 objects belong to the supercluster. Spectroscopic results allow intricate analysis of the supercluster. Additionally, a three-dimensional map is produced and allows velocity dispersion measurements to be made for a small number of member groups and clusters. The paper will be summarised in this Section followed by an analysis of the supercluster using the MgII method.

Background

Cl 1604 has been a targeted area of analysis by many authors, Gunn et al. (1986), Oke et al. (1995), Postman et al. (1998), Lubin et al. (2000), Faber et al. (2003) and more, making it one of the most well-studied structures at redshift $z \sim 0.9$. G08 make use of the imaging data presented by Lubin et al. (2000) and Gal et al. (2005), and provide further improvements on the photometric results and the density maps.

The photometric data presented by G08 made use of the Carnegie Observatories Spectroscopic Multi-slit and Imaging Camera (COSMIC), Kells et al. (1998), and the Large Format Camera (LFC) on the 5 m Palomar telescope; observations were made in the Cousins R and Gunn i' bands on COSMIC and Sloan $r'i'z'$ bands on the LFC. The photometric measurements were repeated on each instrument to provide confidence in the source detections. Sources detected in both the original and repeated measurements were included in a master catalogue which took preference in the measurement that provides the lowest photometric error. The sources were also cross-correlated with the SDSS catalogue to provide confidence in the position measurements. The final, combined database comprised detections from the master catalogues of COSMIC and LFC. Note, there was preference given to measurements detected using the LFC over COSMIC since it covered a larger area and includes

CHAPTER 4

photometric z' measurements.

The next step was to produce a density map of the galaxy selection. Member galaxy selection was made based on the following colour and magnitude constraints:

$$1.0 \leq (r' - i') \leq 1.4$$

$$0.6 \leq (i' - z') \leq 1.0$$

$$20.5 \leq i' \leq 23.5$$

The colour and magnitude limitations were chosen such that large numbers of member galaxies of the supercluster were selected, maximising the contrast of the supercluster in the presence of foreground and background galaxies. A total of 722 objects were selected using the described colour and magnitude constraints out of a catalogue originally containing $\sim 12\,000$ objects. The selected galaxies were plotted on a density map using a kernel smoothing scale of $0.75 h_{70}^{-1}$ Mpc per $10''$, and shown in Figure 4.17.

To classify real groups and clusters in the density map, G08 run the SExtractor (Source Extractor) software by Bertin & Arnouts (1996) on the smoothed density map of colour-selected galaxies. There were 10 cluster and group candidates detected using this method. Note, the nature of the galaxy group and cluster candidates are low-mass and therefore much harder to detect. This was a choice made by G08 so as to observe the finer details of the structure of Cl 1604 but unfortunately it leads to a higher false-detection rate. G08 perform additional analysis on the group and cluster candidates to estimate the number of false detections and take into consideration this flaw when analysing Cl 1604.

Spectroscopic analysis was then performed on the supercluster using five different data sets. Refer to Table 4.2 for the details on each of the five data sets. All of the data from each of the five data sets were combined into one final, master spectroscopic catalogue. Preference was given to the DEIMOS results in cases

CHAPTER 4

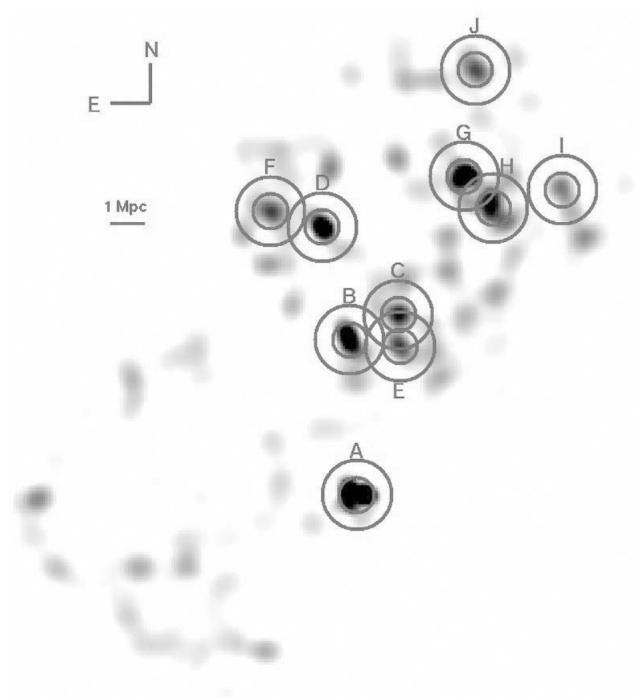


Figure 4.17. Figure taken from G08. Density map of the colour-selected member galaxies of Cl 1604. Circles of radius 0.5 and $1.0 h_{70}^{-1}$ mark the cluster and group candidates.

CHAPTER 4

	Spectrograph	Telescope	Date of Observations
1	LRIS	Keck I & II	Late 1990s
2	LRIS	Keck I & II	2000
3	DEIMOS	Keck II	2003
4	DEIMOS	Keck II	2005 - 2006
5	DEIMOS	Keck II	2006

Table 4.2. Summary of the five data sets used for the spectroscopic analysis on Cl 1604. For additional information on the data sets see the following papers: (1) Oke et al. (1998); (3) Gal & Lubin (2004); (4) Gal et al. (2005); (5) Kocevski et al. (2009).

where both LRIS and DEIMOS observed the same object since the DEIMOS results have improved redshift measurements and also tend to have higher signal-to-noise ratio. The final catalogue contains 1671 unique objects of which: 1215 are extragalactic objects (1148 confirmed), 140 are stars, 427 are in the redshift range of the supercluster $0.84 \leq z \leq 0.96$, and 417 belonging to the supercluster have resolved, non-overlapping object photometry.

Redshift and velocity dispersion measurements are based on the SExtractor calculated cluster centres. However, as seen in Figure 4.17, almost all of the cluster candidates overlap each other making it difficult to truly define the parameters of each cluster. G08 used a histogram to plot the redshift of the objects in Cl 1604, so that an initial selection of redshift peaks could be selected corresponding to the cluster candidates. A broad velocity dispersion was then calculated based on the redshift spread around the median redshift for each cluster candidate. There was one

CHAPTER 4

exception to this: cluster candidate E appears to be a combination of components belonging to cluster candidate B and C, so no velocity dispersion was calculated for E. Further investigation of the velocity dispersion dependence on the galaxy colour revealed different results for different cluster candidates. For instance, cluster A showed a 3σ difference when calculating the velocity dispersion with the full sample of 32 galaxies compared with the sub-sample of 18 red galaxies. However, cluster B showed a less than 1σ overestimate when calculating the velocity dispersion with the full sample of 32 galaxies compared with the sub-sample of 12 red galaxies. For all cluster candidates however, it is seen that the full sample which includes the blue galaxies tends to lead to an overestimation of the velocity dispersion. In the case of Cluster A, G08 suggest that this particular cluster may be a more well-established cluster that has had more time to fully virialise making the velocity dispersion of the red galaxies much more different from any new, infalling blue galaxies. Whereas for cluster B it may be that this cluster candidate is relatively young, not had time to fully virialise, and is still undergoing collapse and merger processes. It appears that the velocity dispersion does not only depend on the colour of galaxies selected, but also on the stage of cluster evolution. Follow-up observations will need to be made to understand more clearly how cluster evolution affects the bias in calculating velocity dispersions with red galaxies.

G08 perform three-dimensional analysis of the supercluster. During this process there were complications when trying to determine the position of the galaxy in redshift due to peculiar velocities. The authors choose to assume the redshift measurements calculated for each galaxy directly reflect the galaxy's position in the structure. The supercluster spans a face-on length of 13 Mpc between clusters A and J, while the redshift depth extends to 100 Mpc, present epoch, see Figures 4.18 and 4.19.

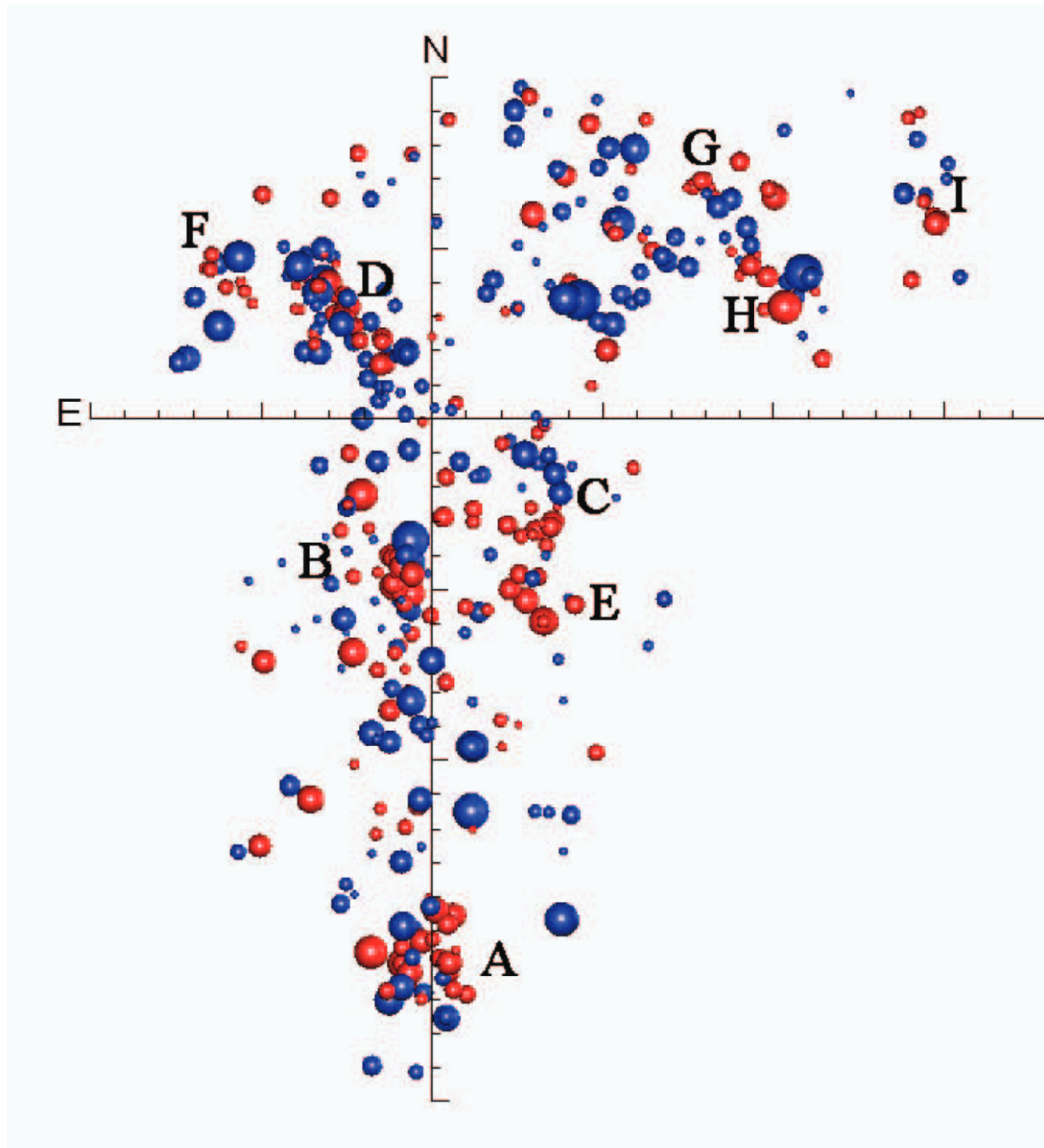


Figure 4.18. Face-on view of Cl 1604 taken from G08. Red and blue spheres represent the red and blue galaxies respectively and the size of the spheres is scaled to represent the observed luminosity of the galaxies. The plot spans approximately 13 Mpc from north to south.

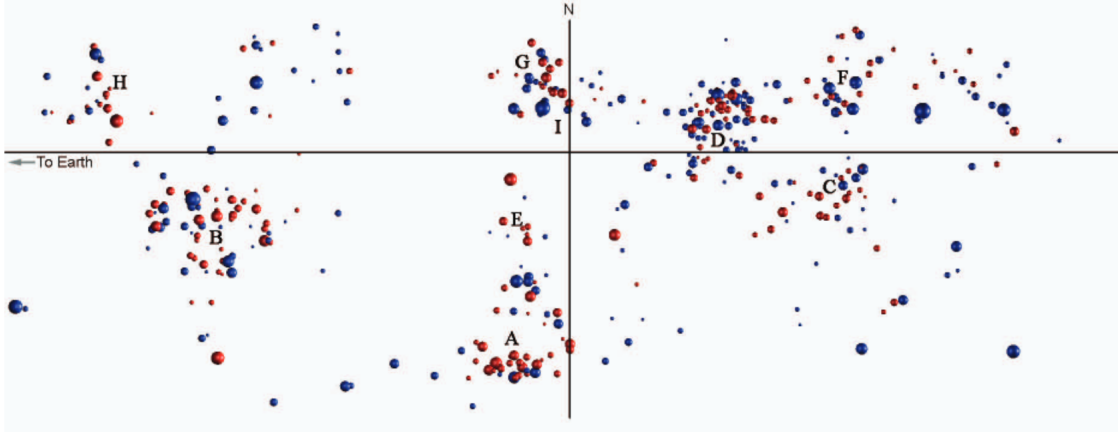


Figure 4.19. Side-on view of Cl 1604 taken from G08. Red and blue spheres represent the red and blue galaxies respectively and the size of the spheres is scaled to represent the observed luminosity of the galaxies. The plot spans approximately 100 Mpc along the horizontal axis depicting the line of sight.

MgII Analysis

The MgII analysis here is centred on Cluster C (RA= 241.03 and Dec = 43.263) from G08 as it appears to be on one of the more centrally located cluster candidates in the supercluster. The first MgII image is produced using ZM-comb in a redshift interval $z = 0.9 \pm 0.1$ and the image is smoothed using a Gaussian kernel (15 Mpc), see Figure 4.20 The centre field coordinates and smoothing radius will remain the same throughout unless stated otherwise. While there does not seem to be an absolute detection in the centre of the field corresponding to the supercluster, there is a detection of MgII absorbers around the centre point. In fact, a closer inspection of the centre point in the right-hand panel of Figure 4.20 reveals that there are no available background probes. This case is therefore a little more ambiguous than the previous targets.

Figure 4.21 shows the MgII plot centred on the supercluster at a reduced redshift thickness $z = 0.9 \pm 0.053$ produced using ZM-comb. Notice now that any structure

CHAPTER 4

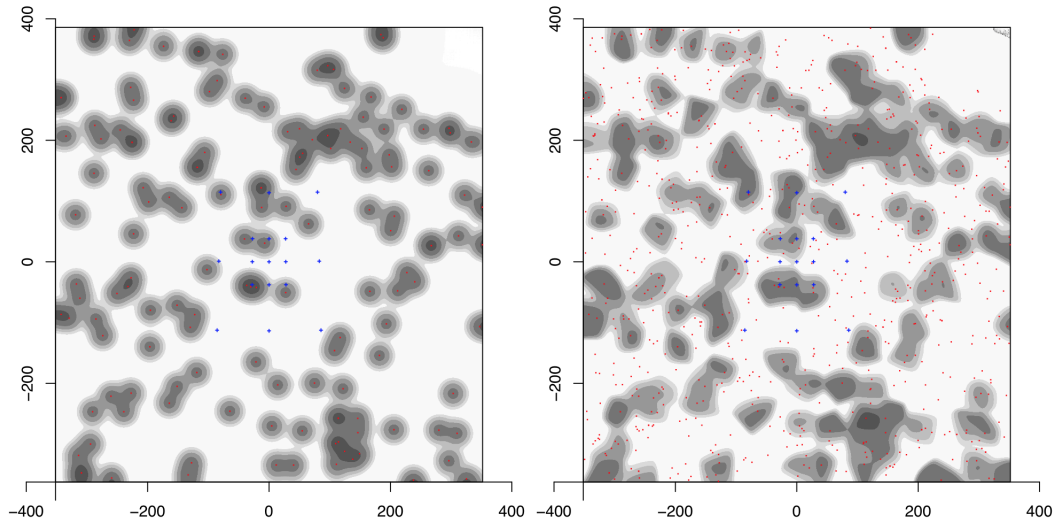


Figure 4.20. MgII image centred on Cluster C from G08 at redshift $z = 0.9 \pm 0.1$ produced using the ZM-comb database and smoothed using a Gaussian kernel (15 Mpc). Blue dotted squares in both images represent a reference grid and grey contours are increasing by a factor of two. Axes are in units of Mpc scaled to the present epoch. Left panel: grey contours and red dots represent the MgII absorbers (possibility of more than one along the LOS). Right panel: red dots represent the available background probes and grey contours represent the MgII absorbers smoothed and flat-fielded. A few MgII absorbers have been detected that are located around the centre coordinates.

CHAPTER 4

originally located at the top of the small dotted blue square has now been erased by comparison with Figure 4.20. However, the MgII absorbers located at the bottom of the small dotted blue square are still detected in the smaller redshift slice. It may be possible that the MgII detection near the bottom of the small, blue dotted square is in association with the supercluster. The same cannot be said about the MgII detection near the top of the small, blue dotted square in Figure 4.20 because the absorbers do not survive the redshift slice reduction in Figure 4.21.

Using the definition of very strong MgII absorption adopted throughout this thesis (Section 2.2), Figure 4.22 shows the very strong MgII absorbers in the field centred on G08 Cl C (from Figure 4.17 at redshift $z = 0.9 \pm 0.053$). The absorbers near the bottom of the small, blue dotted square survive the additional cut of MgII absorbers with equivalent width $W_\lambda \geq 1.0$. While it cannot be said that strong MgII absorption leads to more certainty on the association it has with the target in question, it does provide some confidence that the MgII absorbers are more likely to be real. Therefore it is important to highlight that the absorbers near the centre of the field have a stronger equivalent width.

The combined databases often can provide confidence that the absorbers detected are real, not just spurious detections. For this reason the MgII image centred on the G08 supercluster at redshift 0.9 ± 0.053 is created using ZM-field-all which is the combined database from both independent authors, Z&M and R16, see Figure 4.23. Again, the absorbers located at the bottom of the small, blue dotted square survive the cut of absorbers by using ZM-field-all which only has absorbers in common to both independent authors. This is important because now it has been shown that the absorbers that are of interest – the absorbers located at the bottom of the small, blue dotted square that may be in association with the G08 supercluster – appear in both cuts of data of strong absorbers and then in the combined databases. The confidence that the absorbers of interest are real is high; however, this does not

CHAPTER 4

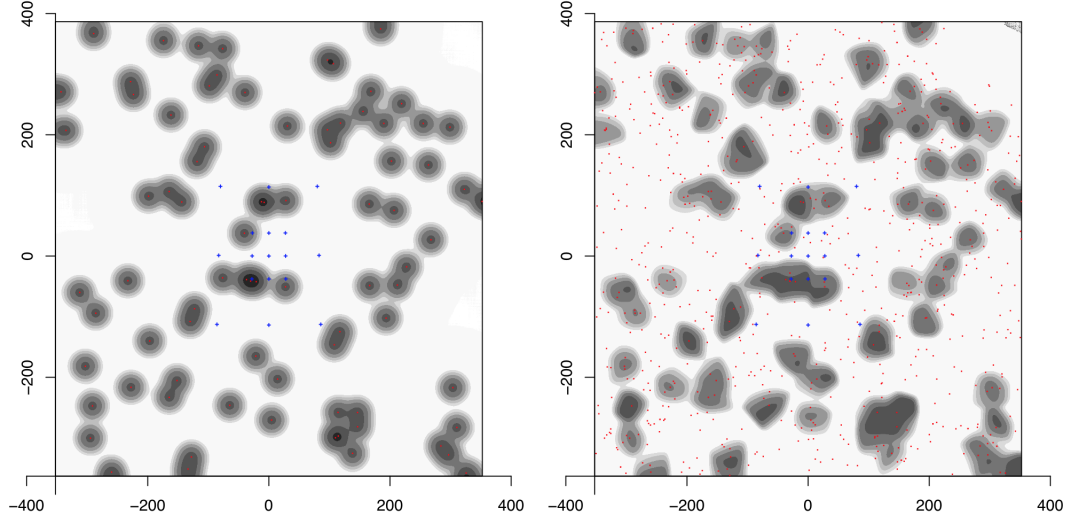


Figure 4.21. MgII images centred on Cluster C from G08 at redshift $z = 0.9 \pm 0.053$, corresponding to a redshift thickness of ~ 282 Mpc in the present epoch, produced using the ZM-comb database and smoothed using a Gaussian kernel (15 Mpc). Blue dotted squares in both images represent a reference grid and grey contours are increasing by a factor of two. Axes are in units of Mpc scaled to the present epoch. Left panel: grey contours and red dots represent the MgII absorbers (possibility of more than one along the LOS). Right panel: red dots represent the available background probes and grey contours represent the MgII absorbers smoothed and flat-fielded. The MgII absorbers located around the centre coordinates are still present even in the reduced redshift slice.

CHAPTER 4

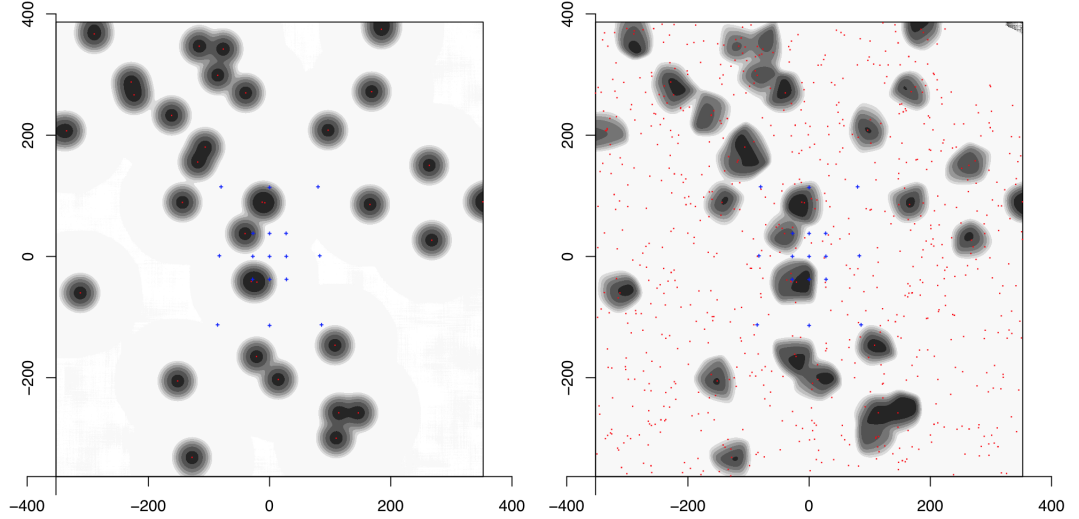


Figure 4.22. Very strong MgII absorbers ($W_\lambda > 1.0$ for the $\lambda\lambda 2796$ line) in the field centred on Cluster C from G08 at redshift $z = 0.9 \pm 0.053$, corresponding to a redshift thickness of ~ 282 Mpc in the present epoch, produced using the ZM-comb database and smoothed using a Gaussian kernel (15 Mpc). Blue dotted squares in both images represent a reference grid and grey contours are increasing by a factor of two. Axes are in units of Mpc scaled to the present epoch. Left panel: grey contours and red dots represent the MgII absorbers (possibility of more than one along the LOS). Right panel: red dots represent the available background probes and grey contours represent the MgII absorbers smoothed and flat-fielded. A few of the MgII absorbers survive the equivalent width cut.

CHAPTER 4

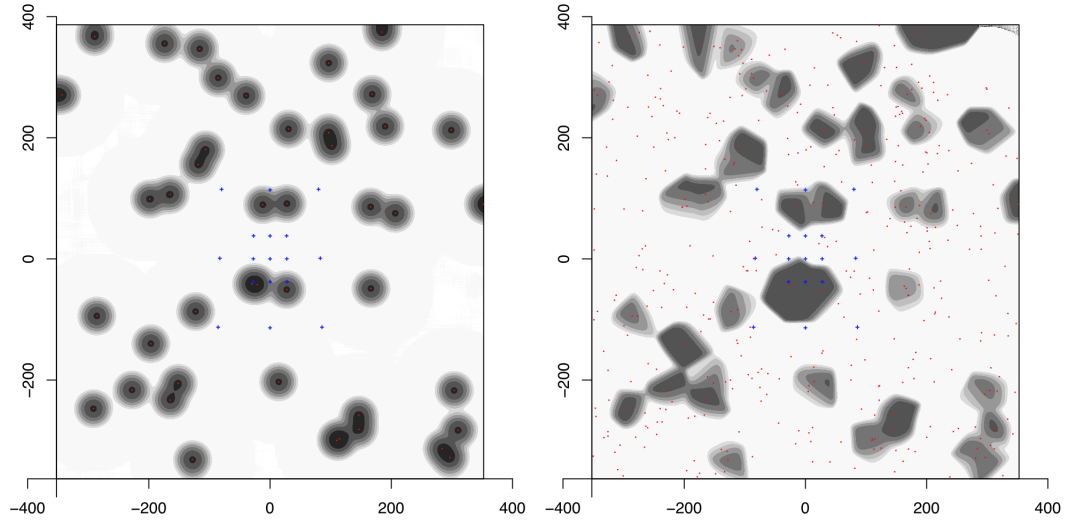


Figure 4.23. MgII images centred on Cluster C from G08 at redshift $z = 0.9 \pm 0.053$, corresponding to a redshift thickness of ~ 282 Mpc in the present epoch, produced using the ZM-field-all database and smoothed using a Gaussian Kernel (15 Mpc). Blue dotted squares in both images represent a reference grid and grey contours are increasing by a factor of two. Axes are in units of Mpc scaled to the present epoch. Left panel: grey contours and red dots represent the MgII absorbers (possibility of more than one along the LOS). Right panel: Red dots represent the available background probes and grey contours represent the MgII absorbers smoothed and flat-fielded. A few of the MgII absorbers are still detected in the paired, combined database.

CHAPTER 4

prove that these absorbers are in association with the supercluster. Whether the absorbers on the periphery of the centre point in the MgII field are in association with the supercluster, Cl 1604, will remain somewhat ambiguous as there are no probes available in the central point of the MgII field that can be used to detect the MgII absorbers.

The null detection in the very central point highlights the difficulty of observing smaller structures when there are no background probes available. It does seem that, had there been the background probes available, a detection would have been made since the surrounding areas (below in particular) highlight a MgII detection. The scale on which the G08 supercluster extends is only of the order of tens of Mpc, whereas the MgII method produces images that cover hundreds of Mpc; the supercluster will not even extend beyond the small dotted square. Therefore, in general, when the background probes are lacking in the very specific point where they are needed, it is difficult to say with certainty whether (1) there are MgII absorbers that have not had chance to be detected due to the lack of probes or (2) there really are no MgII absorbers in association with the target in question. In this case there are MgII absorbers very close to the centre field coordinates which gives some reason to believe that the MgII absorbers located at the bottom of the centre point are in association with the G08 supercluster.

Before concluding this Section, it is worth pointing out the dense region of MgII absorbers located in the top-right quarter of the MgII image in Figure 4.20 and 4.21. However, this dense region of absorbers does not survive either of the data cuts in Figures 4.22 and 4.23. It seems that this particular dense region of absorbers may potentially be made up of some spurious absorbers or perhaps just weak absorbers, since both cuts of data are biased against weak absorbers. As mentioned earlier, having strong absorbers does not necessarily mean they are certain and real, therefore, having weak absorbers does not necessarily imply that they are mistakes

or less real. However, it is likely easier to mistake a MgII absorber when it has a smaller equivalent width than if it has a large equivalent width. Additionally, the dense region of absorbers does not survive the combined databases which also reduces confidence that they truly are real absorbers.

4.4 Target 4: Lynx Field at $z = 1.26$

Two rich clusters, RXJ 0848.9+4452 and RXJ 0848.6+4453, from the ROSAT Deep Cluster Survey, located in the Lynx field at redshifts $z = 1.26$ and $z = 1.27$ respectively, are documented by Stanford et al. (1997) and Rosati et al. (1999). In this Section I will review two papers, Ohta et al. (2003) and Nakata et al. (2005), that find evidence for potential supercluster-type structures located in the Lynx field which are believed to be in association with the two known clusters. Then, I will move on to the MgII analysis to see if there is a signal that may also highlight the structures discussed in these papers.

Background

In Ohta et al. (2003) (hereafter O-03) there are six X-ray sources within the 2 – 7 keV energy band detected in the Advanced Satellite for Cosmology and Astrophysics (ASCA) Lynx Deep Survey. Five of the six X-ray sources are identified with AGN/QSO and three of these QSOs are found to be located at redshifts $z \sim 1.3$. Additionally, two more X-ray sources were detected in the 0.2 – 2 keV energy band. O-03 find that the separations between the X-ray sources and the known clusters are between 7 – 18 Mpc at present epoch, which implies that there could be an association between the clusters and X-ray sources.

O-03 used the data from the Burke et al. (1991) observations which used the Solid-State Image Spectrometer instrument (SIS) concentrated on a roughly square region of sky spanning a total area of 530 arcmin². To avoid confusion of deep X-ray

CHAPTER 4

sources with known soft X-ray sources, the ROSAT data (from which the which the two known clusters in the Lynx field were discovered) are used to determine the positions of already known X-ray sources. A method of image fitting described by Ueda et al. (1999) is adopted to determine an initial list of the unknown X-ray sources in the analysis field; the image fitting method is repeated after the initial candidates are detected to search for any final residuals from X-ray sources. The images are analysed in three energy bands; $0.7 - 7.0$ keV, $0.7 - 2.0$ keV and $2.0 - 7.0$ keV. Using this method, two new X-ray sources are detected by ASCA that were not in the ROSAT database. Six of the X-ray sources had significance greater than 3.5σ in the $2.0 - 7.0$ keV energy band and were therefore classified as the hard-band-selected sample. Three of the X-ray sources overlapped with the Chandra FOV and allowed O-03 to take advantage of the archival data and perform spectral analysis of these three sources.

Once the X-ray source candidate list had been finalised, the next step was to determine the optical counterparts. O-03 used the Kiso 1.05 m Schmidt telescope with a Tek 1024×1024 CCD to obtain optical measurements of the hard-band-selected X-ray sources and then performed follow-up observations in the NIR I_C band using the University of Hawaii 88 inch telescope with a Tek 2048×2048 CCD. Optical spectroscopy was also performed on the hard-band-selected X-ray sources using the Gold Camera spectrograph on the Kitt Peak National Observatory (KPNO) 2.1m telescope. Follow-up spectroscopic measurements were made on the UH 88 inch telescope with the Intermediate-dispersion Spectrograph and Imaging System (ISIS) to increase the S/N of the spectra and improve the redshift measurements of the optical sources. The spectroscopic observations showed AGN-like emission lines corresponding to each of the X-ray sources; three of the sources showed emission lines corresponding to QSOs in the redshift range $z = 1.260 - 1.286$.

CHAPTER 4

For a FOV of size like the one investigated by O-03, the expected number of hard-band X-ray sources based on work done by Ueda et al. (2003) is 0.03. This suggests that the three X-ray sources found at redshifts $z \sim 1.3$ are significantly overdense. See Figure 4.24 for the distribution of X-ray sources and QSOs in the field containing the two known clusters. Also, the X-ray sources seem to be situated very close to the two known clusters suggesting they are in association with each other. The three QSOs seem to lie on the outskirts of the clusters which has previously been noted by Tanaka et al. (2001) and Haines et al. (2001) as potentially a feature of galaxy clustering and QSOs. However, further investigation of the relationship between QSOs and galaxy clustering, especially at these redshifts, is needed to confirm whether it is a general property or a random occurrence.

In Nakata et al. (2005) (hereafter N05) the presence of a potential supercluster made up of several groups of galaxies around the two known clusters, RXJ 0848.9+4452 and RXJ 0848.6+4453, located in the Lynx field at redshift $z \sim 1.27$ is reported. Photometric Redshift techniques reveal the galaxy groups to be mostly red and consistent with passively evolving galaxies. Here I will briefly outline some of the instruments used and methods applied in N05.

The Suprime-Cam on the 8.2 m Subaru telescope is used to obtain deep and panoramic multicolour-imaging in the visible and NIR bands, $VRi'z'$. Of these four imaging bands, i' proved to give the deepest image and was therefore used to determine the initial sample. The total FOV covered a region $26.4' \times 24.1'$ with a resolution of $0.2''$ per pixel. The initial sample of objects is identified under the condition that there are five or more connected pixels in the image with counts above 2.8σ .

A photo- z technique was used to subtract the foreground and background galaxies in order to enhance the contrast of the galaxies in the analysis field. Galaxies with high confidence redshift estimates using the photo- z technique that fall within

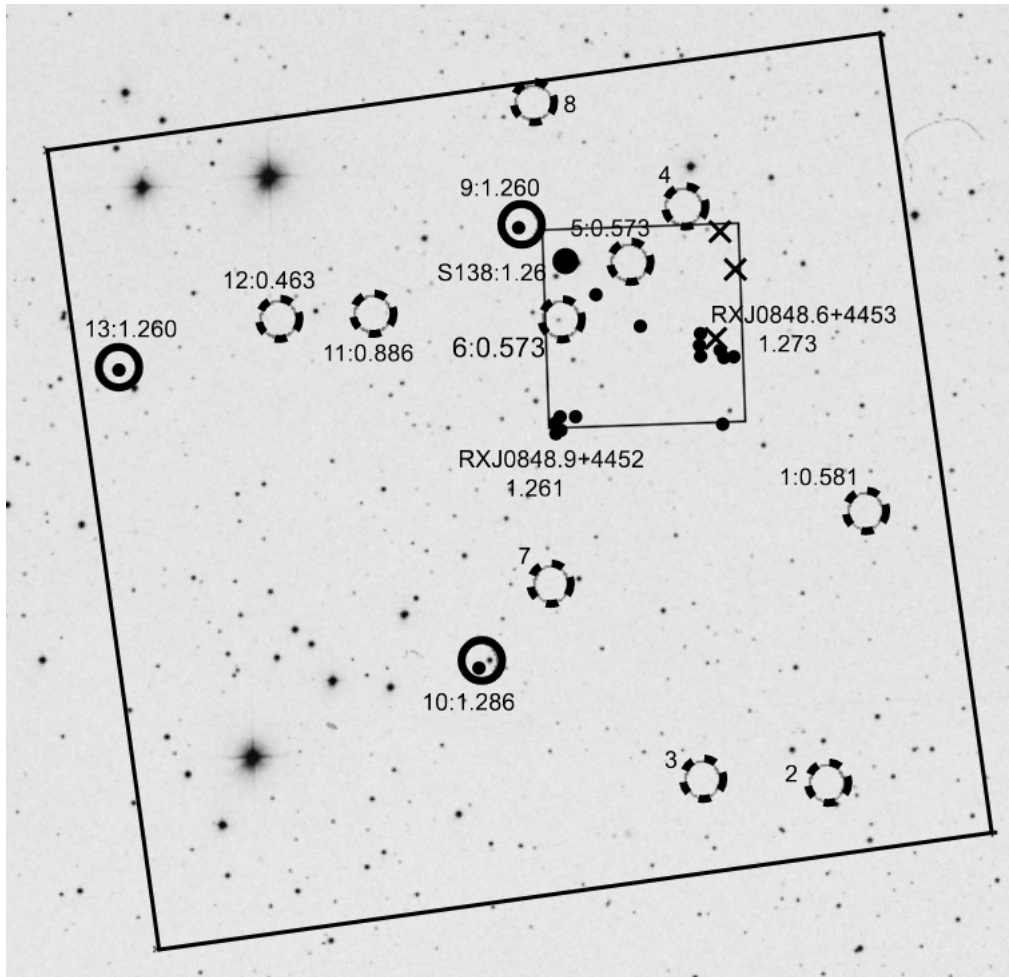


Figure 4.24. Figure taken from O-03. The labelling system refers to the target ID number followed by a colon and the redshift of the target. The image shows the distribution of the X-ray sources (dashed circles) and the QSOs (bold circles with dot in the middle showing the optical identification), along with the spectroscopically confirmed galaxies in the two known clusters (small dots), early type galaxies at redshift $z = 1.26$ (large dots) and red objects (crosses). The large square (~ 20 arcmin²) is the field analysed in O-03 and the small square indicates the FOV of the SPICES Deep JK_S survey by Maxfield et al. (2002). The image is orientated with north at the top and east on the left.

CHAPTER 4

the redshift interval $1.00 \leq z \leq 1.35$ were selected as plausible members of groups to be contained within the supercluster at redshift 1.27. Note: the reason for the asymmetric redshift interval around $z = 1.27$ is because N05 found that when their photometric results were compared with spectroscopic results, there was a general bias for underestimating the redshift due to misidentifying blue galaxies as red galaxies at lower redshifts. In total there were 2229 selected galaxy candidates that were identified using the photo-z technique that fell in the redshift range $1.00 \leq z \leq 1.35$. Additional photometric measurements were made in the K' band using the NIR camera CISCO on the Subaru Telescope to provide better accuracies and confidence in the redshift measurements of the galaxy candidates. N05 find that a sample of redshift measurements from the VRi' bands agree well with the redshift estimates once K' band measurements are included for the red galaxies. However, for the blue galaxies it was found that the NRi' measurements generally underestimated the redshift estimates of the galaxy sample. This was not seen as a major problem since the sample of 2229 galaxy candidates was mostly dominated by red galaxies.

Figure 4.25 shows the spatial distribution of the 2229 galaxy candidates and labels the galaxy group candidates. The contours are generated using the 10 nearest neighbours corresponding to 2, 3, 4 and 5 standard deviations based on a random distribution. Seven galaxy group candidates were detected as having a local surface density greater than 5σ . N05 repeat their method on a sample of galaxies from the Subaru Deep Field to increase confidence in their method and results and find that only two local densities exceed the 5σ level, whereas in the Lynx field there are nine such overdensities. Finally, a small investigation into the density distribution of the galaxies in the groups as a function of distance from the centre of the group reveal the expected profile based on the King law profile (this was for all of the clusters except gr6). The N05 chain of galaxy groups that are believed to form a supercluster in association with the two known galaxy clusters are estimated to extend to a size

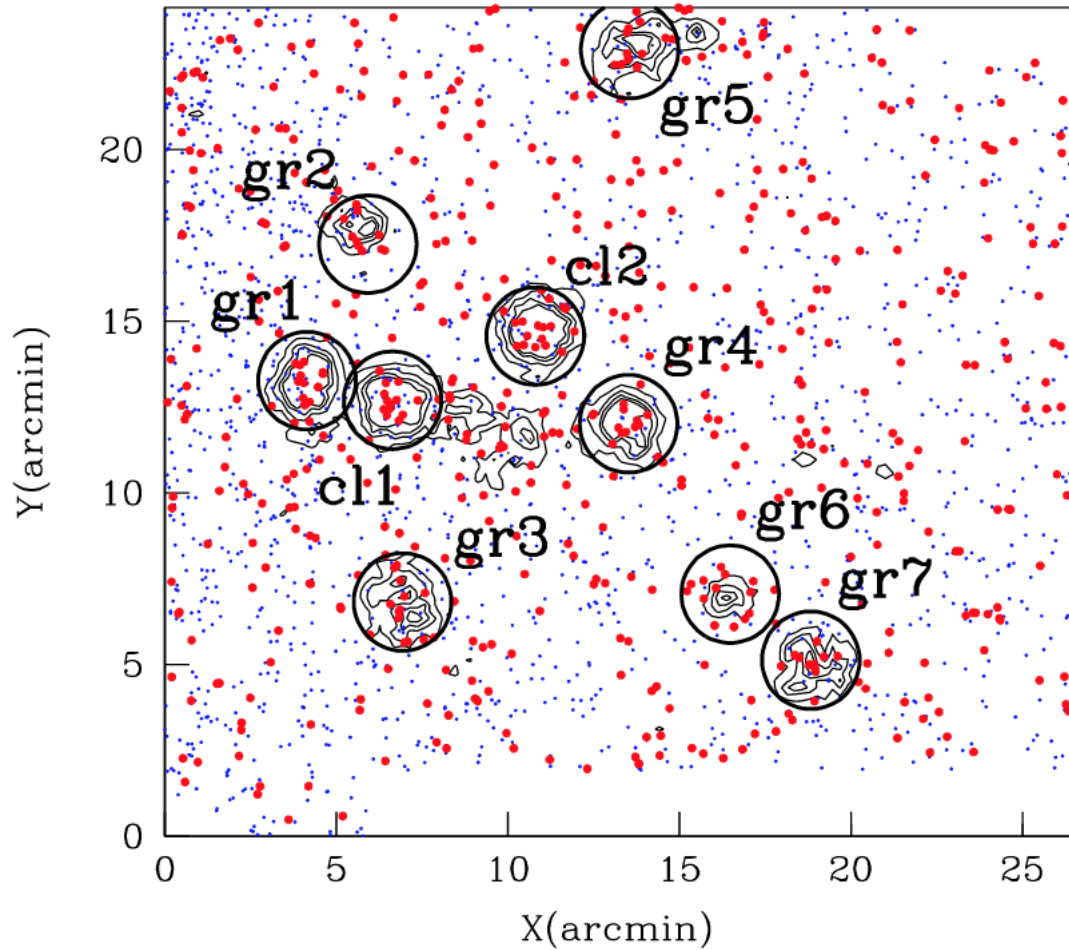


Figure 4.25. Figure taken from N05. Distribution of the red and blue galaxy candidates (indicated by large red dots and small blue dots respectively) in the Lynx field containing the two known clusters labelled c11 and c12. Seven galaxy group candidates are circled and labelled which span approximately $20'$ or ~ 23 Mpc at present epoch. (Contours mark the confidence levels at 2, 3, 4, and 5σ . Image is orientated with north at the top and east on the left.

CHAPTER 4

of 13 Mpc.

MgII Analysis

The MgII absorbers in the field centred on the midpoint (RA 132.19°, Dec 44.88°) between the two known clusters in the Lynx field, RXJ0848.6+4453 and RXJ0848.9+4452 at redshift $z = 1.27$ and $z = 1.26$ respectively – Stanford et al. (1997), Rosati et al. (1999) – highlight a structure in the centre of the field, see Figure 4.26. The left panel shows the absorbers with red dots and the grey density contours represent the absorbers smoothed with a Gaussian kernel ($\sigma = 15$ Mpc). The right panel is the flat-fielded image, i.e., here the grey density contours are a result of the MgII absorber density at that point and the available background probes in the vicinity. The absorbers in the centre of the field in the left panel of Figure 4.26 seem to travel down towards the bottom corner of the smaller blue dotted square. However, once the distribution of background probes has been considered, the flat-fielded image in the panel on the right seems to change the image slightly so that the absorbers appear to curve to the bottom of the smaller blue dotted square and lift back up travelling slightly north-east. In O-03 the detected X-ray sources are almost all to the east of the two known clusters in Figure 4.24 suggesting the detected MgII absorbers are highlighting the mass associated with these X-ray clusters. Although the scales are quite different, that is to say, O-03 measures the X-ray sources in a $20' \times 20'$ FOV whilst the MgII image spans at least 6.7° at this redshift and centre coordinates, the job of the MgII method is to indicate LSS. The absorbers pass through the centre of the MgII field and also mark out a structure moving in the eastward direction which therefore suggest that the absorbers detected in the MgII image are potentially in association with the X-ray sources, but more importantly, appear to extend the X-ray cluster to a 50 – 100 Mpc structure. A similar argument can be made for the structure of galaxy groups/clusters documented by N05. In Figure 4.25, there are three galaxy group candidates that are situated on the east

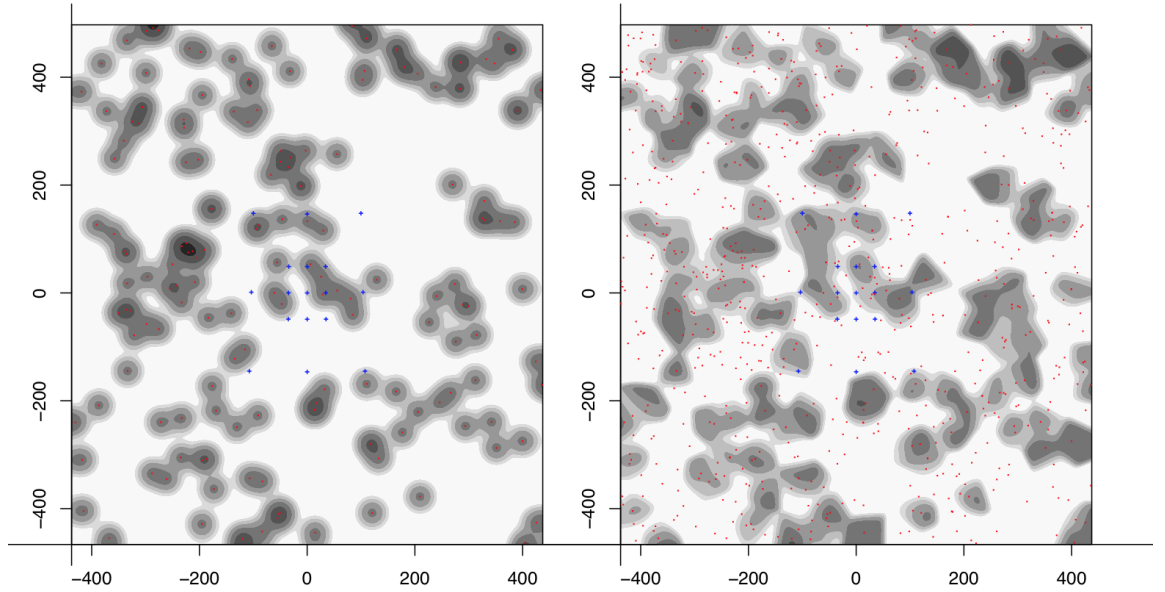


Figure 4.26. MgII absorbers in the field centred on the Lynx field at the midpoint between the two known clusters at redshift $z = 1.27 \pm 0.1$ using ZM-comb and smoothed with a Gaussian kernel (15 Mpc). Blue dotted squares in both images represent a reference grid and grey contours are increasing by a factor of two. Axes are in units of Mpc scaled to the present epoch. Left panel: grey contours and red dots represent the density distribution of the MgII absorbers (could be more than one along the LOS). Right panel: red dots represent the available background probes, grey contours represent the density distribution of the flat-fielded MgII absorbers. There is a detection of MgII absorbers in the centre coordinates.

CHAPTER 4

of the two known galaxy clusters' midpoint, which may be in association with the MgII absorbers detected in the small, blue dotted reference grid in Figure 4.28. The other four galaxy group candidates that are located to the south-west of the two known clusters does not seem to be detected by the MgII. However, again it must be pointed out that the FOV of the N05 galaxy group field is significantly smaller ($26.4' \times 24.1'$) than the FOV of the MgII image. Therefore the absorbers associated with the galaxy groups are not necessarily going to directly overlap the galaxy groups. In particular, one must note that the gaps between available background probes probably exceeds the scales at which galaxy clustering occurs, which is why MgII is used to highlight LSS and not the small-scale structure between.

A closer inspection of the distribution of background probes in the field centred on the Lynx field at redshift $z = 1.27$ revealed that the background probes at this location seem particularly uneven. Figure 4.27 shows the density distribution of the available background probes in the field. There is a large hole in the top-right quarter of the field and a dark-grey dense area to the left of the centre point. Large differences in local density of available background probes will have quite a significant effect on not only the MgII absorption detection, but also the void detection, which highlights the importance of additional databases and increased FOV coverage. The availability of background probes across the sky has been discussed throughout this thesis, in particular in Section 3.3 where the TOPCAT image reveal the varied distribution of QSOs in each of the databases.

For the next step in MgII analysis the redshift thickness in the image is reduced to correspond to roughly 282 Mpc at present epoch, see Figure 4.28. So far, I have looked at the MgII image centred around $z = 1.27 \pm 0.1$ which is a fairly large slice of sky to observe and corresponds roughly to 435 Mpc at present epoch. The MgII image centred on the Lynx field in the redshift interval 1.27 ± 0.08 which roughly corresponds to a redshift thickness of 282 Mpc appears to retain the structure that is

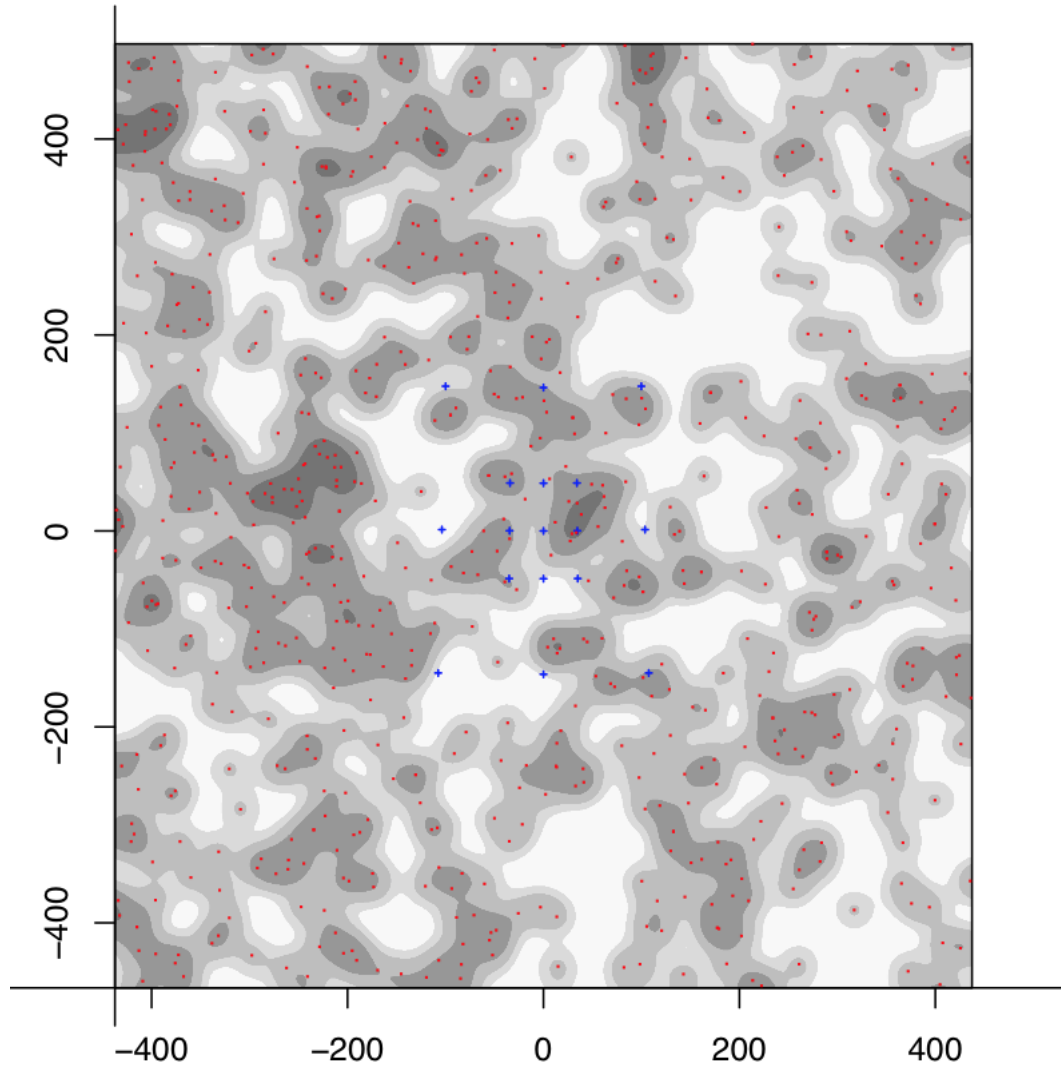


Figure 4.27. Density image of the available background probes in the MgII field centred on the Lynx field at redshift $z = 1.27$. Axes are in units of Mpc scaled to the present epoch. This density image demonstrates the non-uniformity in the available background probes.

CHAPTER 4

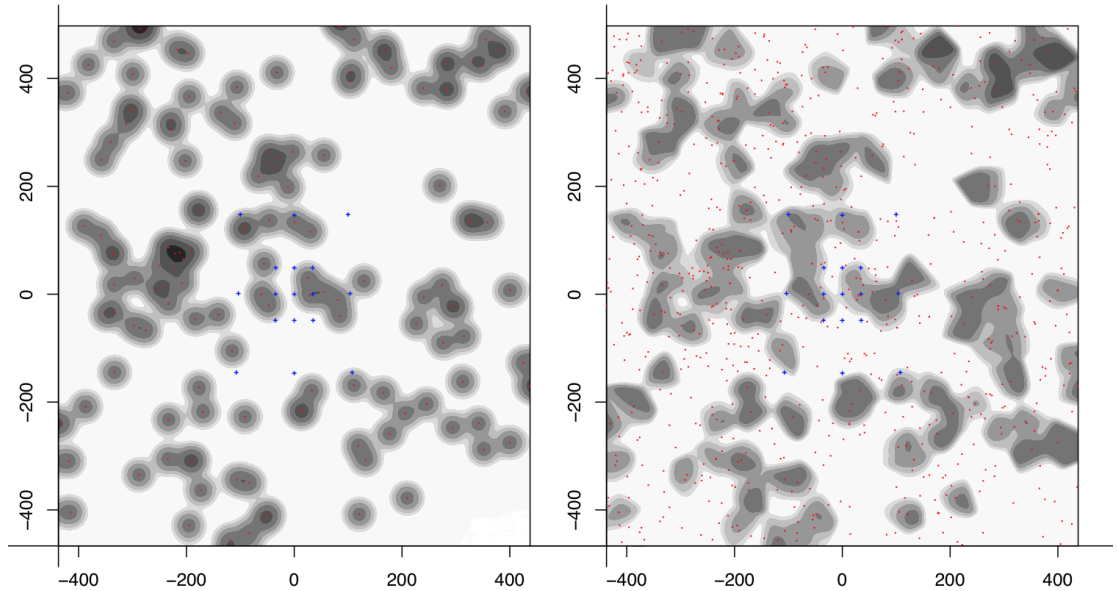


Figure 4.28. MgII absorbers in the field centred on the Lynx field at the midpoint between the two known clusters at redshift $z = 1.27 \pm 0.08$, corresponding to a redshift thickness of 282 Mpc in the present epoch. MgII absorbers plotted using the ZM-comb database and smoothed with a Gaussian kernel (15 Mpc). Blue dotted squares in both images represent a reference grid and grey contours are increasing by a factor of two. Axes are in units of Mpc scaled to the present epoch. Left panel: grey contours and red dots represent the density distribution of the MgII absorbers (could be more than one along the LOS). Right panel: red dots represent the available background probes, grey contours represent the density distribution of the flat-fielded MgII absorbers. There is a detection of MgII absorbers in the centre coordinates.

CHAPTER 4

located in the centre of the field travelling east; this now gives confidence that these absorbers are in association with the the X-ray sources in O-03 and the galaxy group candidates in N05, rather than absorbers that happened to be centred on the same coordinates but at a different redshift. Furthermore, the majority of the absorbers in the MgII field with the larger redshift slice also seem to be detected in the smaller redshift range which could be a result of having a particularly dense field. As a side note, this is the second structure that has been assessed at redshift $z = 1.27$ and with the inclusion of the HLQG and the CC-LQG, Clowes et al. (2013), Clowes & Campusano (1991), this makes four structures in total that happened to fall at the same redshift without any bias to searching for structures at this particular redshift. This is a curious observation that has just mildly piqued an interest for further investigation for a later time.

An investigation of the strength of absorbers in the MgII field centred on the Lynx field at redshift $z = 1.27 \pm 0.08$ highlights almost all of the absorbers in the equivalent width range corresponding to medium and strong MgII absorption, $W_\lambda \geq 0.3$, see Figure 4.29. The physical meaning of detecting strong absorbers over weak absorbers has been discussed in brief in Section 2.2, although it is not yet fully understood whether there is an association with galaxy morphology and strength of absorbers. In addition, most of the absorbers in the databases have equivalent widths greater 0.3 \AA . Further work could include an investigation of whether the MgII absorption method can shed light on any association there may be with galaxy morphology. However, in order to make any connection between MgII absorption and galaxy morphology, accurate optical spectroscopic measurements of high redshift galaxies would be needed and this requires very large telescopes and many hours of telescope time. Reducing the equivalent width condition further to those absorbers with $W_\lambda \geq 1.0$ yields a small portion of the absorbers in the MgII field, but in particular, the absorbers in the centre of the field which are believed

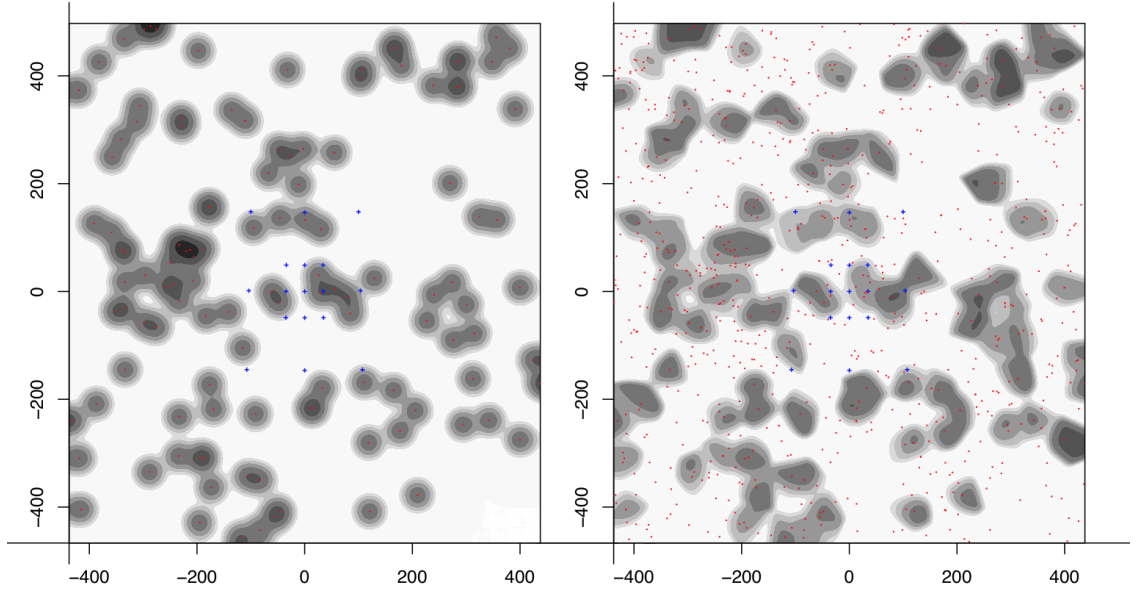


Figure 4.29. MgII absorbers with equivalent width $W_\lambda \geq 0.3$ in the field centred on the Lynx field at the midpoint between the two known clusters at redshift $z = 1.27 \pm 0.08$. MgII absorbers are plotted using the ZM-comb database and smoothed with a Gaussian kernel (15 Mpc). Blue dotted squares mark out a reference grid and grey contours are increasing by a factor of two. Axes are in units of Mpc scaled to the present epoch. Left panel: grey contours and red dots represent the MgII absorbers (could be more than one along the LOS). Right panel: red dots represent the available background probes, grey contours represent flat-fielded MgII absorbers. Many of the MgII absorbers are still present in the equivalent width cut.

CHAPTER 4

to be in association with the X-ray sources and/or galaxy group candidates still remain, see Figure 4.30. There is an increased level of confidence associated with strong absorbers for the fact that it is easier to mistake a weak absorber than it is a strong one, but this is only a qualitative judgement. Additionally, there may be reasons to believe that a strong absorber will arise closer to the centre of galaxy halo, as suggested by Churchill et al. (2005) and perhaps this is what the MgII detection is showing.

The MgII analysis of the Lynx field at redshift $z = 1.27$ shows a detection in the centre of the field that extends in a small curve to the east on scales of $\sim 50 - 100$ Mpc. After reducing the redshift thickness to 282 Mpc in present epoch scales the MgII detection did not seem to reduce very much, suggesting that this particular field may be more compact along the redshift axis. I have hinted that this may even be a special feature of redshift $z = 1.27$ since there are various documented structures at this redshift interval, Clowes & Campusano (1991), Clowes et al. (2013) and S12. Applying the condition in the MgII analysis to plot only those absorbers that have equivalent width stronger than $W_\lambda \geq 0.3$ revealed that almost all of the absorbers in the field can be classified as medium or strong. Furthermore, the important absorbers at the centre of the redshift survive an additional condition to plot only those absorbers with equivalent width greater than $W_\lambda \geq 1.0$, revealing that the absorbers in the centre of the field, the ones believed to be in association with the two known clusters, the X-ray sources and/or the chain of galaxy group candidates, are particularly strong absorbers. Perhaps this is due to the location of the absorber in reference to the distance from the galaxy halo centre, or maybe it is an indication of galaxy morphology, which could be investigated further in the future.

One final note: there is a very strong signal of MgII absorbers located to the left of the large blue dotted square in Figure 4.26 and Figure 4.28. It would be interesting

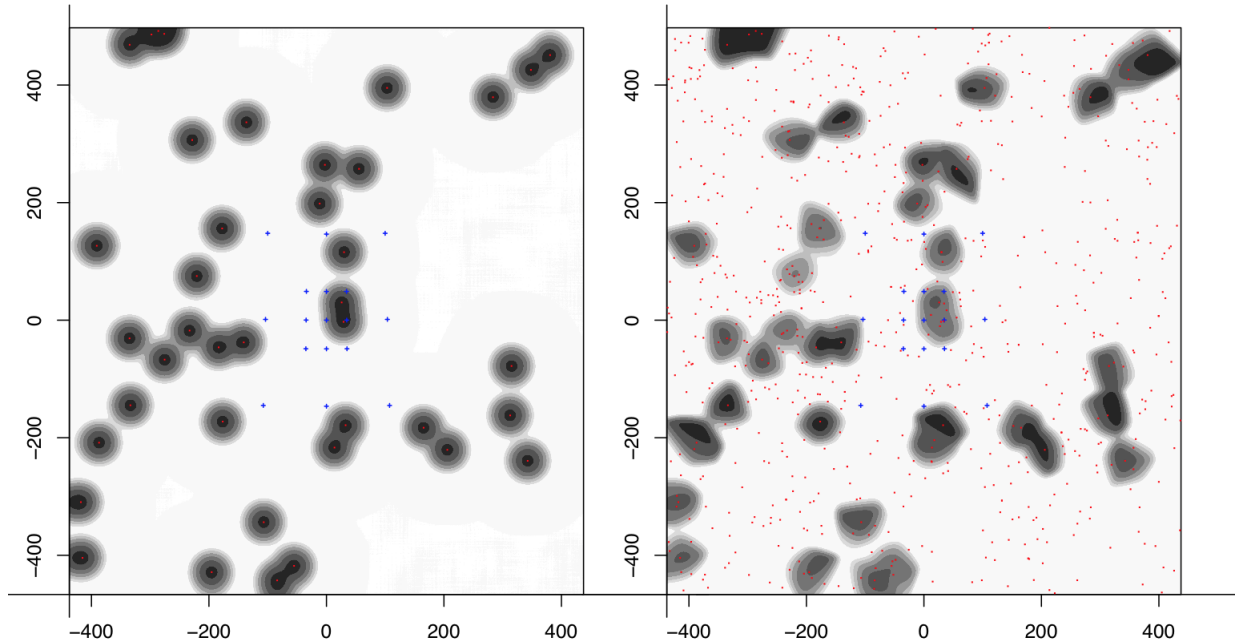


Figure 4.30. MgII absorbers with equivalent width $W_\lambda \geq 1.0$ in the field centred on the Lynx field at the midpoint between the two known clusters at redshift $z = 1.27 \pm 0.08$. MgII absorbers are plotted using the ZM-comb database and smoothed using a Gaussian kernel (15 Mpc). Blue dotted squares mark out a reference grid and grey contours are increasing by a factor of two. Axes are in units of Mpc scaled to the present epoch. Left panel: grey contours and red dots represent the MgII absorbers (could be more than one along the LOS). Right panel: red dots represent the available background probes, grey contours represent flat-fielded MgII absorbers. The MgII absorbers, slightly off from the centre coordinates, are detected in the very strong equivalent width cut.

to do further analysis on this feature since it may indicate a large structure or supercluster. However, one can see that in Figure 4.27 the available background probes corresponding to the strong signal of MgII absorbers to the left of the large blue dotted square also appears overdense, which would have to be considered a bias when performing any analysis.

4.5 Target 5: SZ Cluster at $z = 0.763$

In this Section I investigate one particular high-redshift SZ cluster presented by Burenin et al. (2018) (hereafter referred to as B18). The cluster comprises three galaxies with an average spectroscopic redshift of $z = 0.763$, and with a strongly gravitationally lensed background galaxy detected in the optical images corresponding to this cluster at a redshift of $z = 4.262$. An overview of the B18 paper is outlined in brief in this Chapter and a description of the cluster, as according to B18, will be included. Finally, I will present the MgII analysis.

Background

The second Planck catalogue of Sunyaev-Zeldovich sources 2015 (PSZ2) contains 1653 objects, of which 1203 have already been associated with galaxy clusters, Planck Collaboration et al. (2016), B18. Only massive galaxy clusters with mass $M \gtrsim 5 \times 10^{14} M_{\odot}$ at redshift $z \gtrsim 0.5$ can be detected in PSZ2. The unidentified sources in this catalogue most likely comprise galaxy clusters at high redshift, but due to difficulty in observing high redshift galaxies optically, the Planck catalogue has much lower completeness at high redshifts $z \gtrsim 0.7$. Galaxy clusters below redshift $z = 0.7$ have reasonable coverage from various catalogues and other sky surveys. B18 makes use of the data available from the WISE all-sky survey, Pan-STARRS and their own optical measurements from a collection of telescopes to identify the high redshift galaxy clusters in PSZ2.

CHAPTER 4

Images from WISE data are cleaned of known stars (positions of which are provided by SDSS data) and then the images are smoothed such that the image depicts only the objects in galaxy clusters that have not been identified yet. This allows for the first selection of galaxy clusters which can be observed up to redshift $z \sim 1 - 2$ using this technique. B18 then uses the data from Pan-STARRS1 survey and their own measurements taken from a collection of different telescopes (see Table 4.3) to provide a deeper examination of the galaxy clusters in optical and NIR. Of the 18 galaxy clusters investigated by B18, seven proved to be in association with SZ sources at high redshifts. Optical and NIR measurements provide a detailed view of the clusters, and the brightest galaxies in the clusters are used to calculate spectroscopic redshifts.

Telescope	Size (m)	Instruments	Location
Russian-Turkish	1.5	TFOSC	Bakyrlytepe (Turkey)
Calar Alto	3.5	MOSCOA	Sierra de Los Filabre (Spain)
SAO RAS	6	SCORPIO/SCORPIO2	Zelenchuksky District (Russia)

Table 4.3. Table of information for the telescopes and instruments used in obtaining optical information on the B18 cluster candidates.

The cluster candidate discussed in this Section, PSZ2 G069.39+68.05, was first identified with a distant galaxy cluster in the extended Planck SZ galaxy cluster catalogue, Burenin (2017) (hereafter B17). Figure 4.31 shows the WISE and optical image of the B18 cluster candidate. The WISE image has been smoothed on a $24''$ radius which corresponds to approximately 180 kpc at redshift $z = 0.8$. The optical image comprises three images taken in the SDSS *irg* filters, where the *ri* images were obtained using their own observations at a variety of telescopes listed

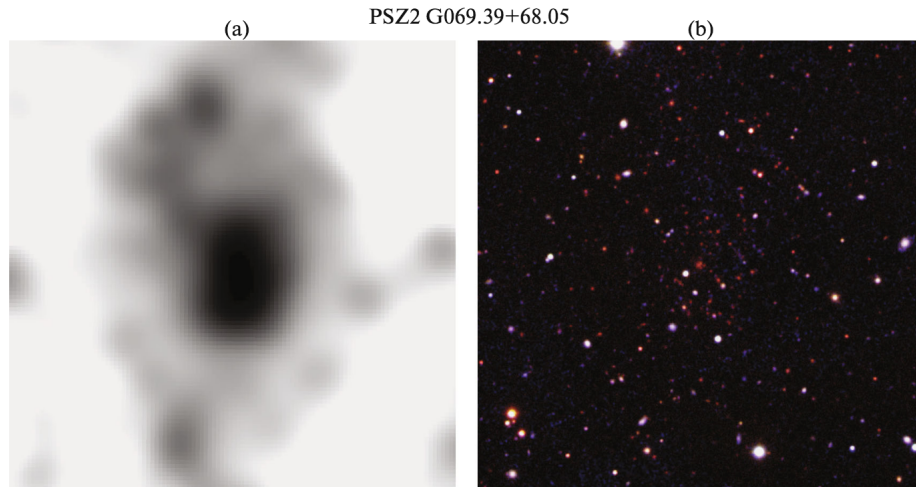


Figure 4.31. B18 cluster candidate, G069.39+68.05, WISE image (left) and optical image from various observations (right) at redshift $z = 0.763$. Image size $5' \times 5'$. Figure from B18. Authors did not specify north and east directions.

in Table 4.3, and the g filter image was taken from the SDSS data. The image size for both WISE and the optical is $5' \times 5'$. Based on Figure 4.31 in the left-hand panel (WISE image) the cluster is centrally concentrated with a nearly circular shape. The lower density regions (lighter grey) can be seen extending the cluster in the vertical direction almost extending across the whole image, which at a redshift of $z = 0.763$ corresponds to a physical size at present epoch of 3.96 Mpc.

Spectroscopy is performed on the brightest galaxy in this cluster candidate and a spectroscopic redshift measurement is made based on the detected H and K lines. The measured redshift is $z = 0.763 \pm \sim 0.001 - 0.003$, see Figure 4.32.

One final interesting feature to note about PSZ2 G069.39+68.05 is that there is a gravitationally lensed galaxy detected in the centre of the B18 cluster candidate that extends up to $7''$. The lensed galaxy in the cluster candidate can be seen in the optical image as a very faint arc in Figure 4.33 pointed out by the arrow labelled ‘L’. The lensed galaxy is calculated to be at a redshift of $z = 4.262$ based on the spectroscopic measurements of the arc.

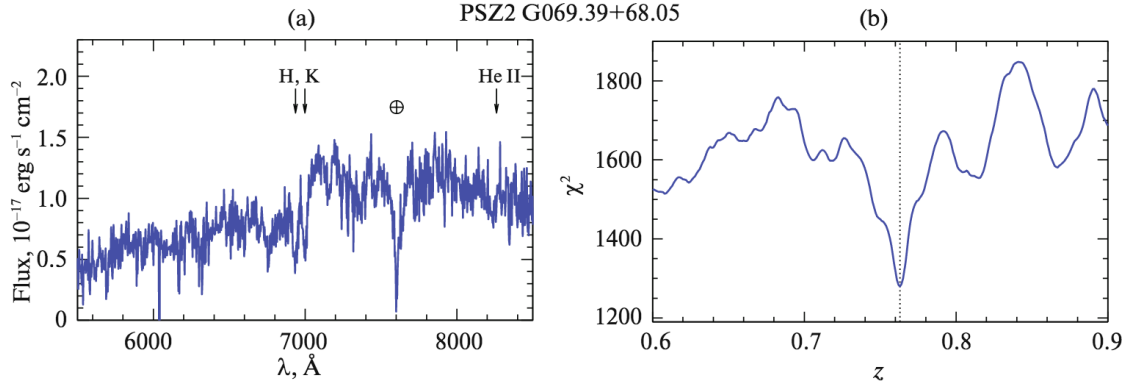


Figure 4.32. Spectra of the brightest galaxy in the B18 cluster candidate PSZ2 G069.39+68.05. The indicated spectral features are used to measure the spectroscopic redshift. Figure from B18.

MgII Analysis

The first step to analysing the targets in MgII is to plot the MgII absorbers in the field centred on the cluster candidate with a redshift thickness of $\Delta z = \pm 0.1$ and a FOV spanning 16 deg in the tangent-plane x (tp-x) coordinates and 10 deg in the tangent-plane y (tp-y) coordinates using ZM-comb. This first test usually gives an indication to what, if anything, there is in the general field surrounding the cluster candidate. For the B18 cluster candidate this produces a rather interesting dense stripe travelling east to west passing through the field centre, see the left-hand panel in Figure 4.34. At redshift $z = 0.763$, a redshift thickness of $\Delta z = \pm 0.1$ corresponds to a present epoch proper distance of 576.554 Mpc. The redshift thickness is reduced to ~ 282 Mpc in the second MgII test to see if the interesting dense stripe survives the reduction in absorbers, see the right hand panel in Figure 4.34. The dense stripe of absorbers travelling east to west appears to mostly survive the redshift thickness reduction and extends up to approximately 500 Mpc. However, in the left-hand panel of Figure 4.34 the stripe extends across the whole MgII image, > 600 Mpc. The fact that the MgII absorbers no longer extend across the whole field once the redshift thickness is reduced could simply be a result of having a large

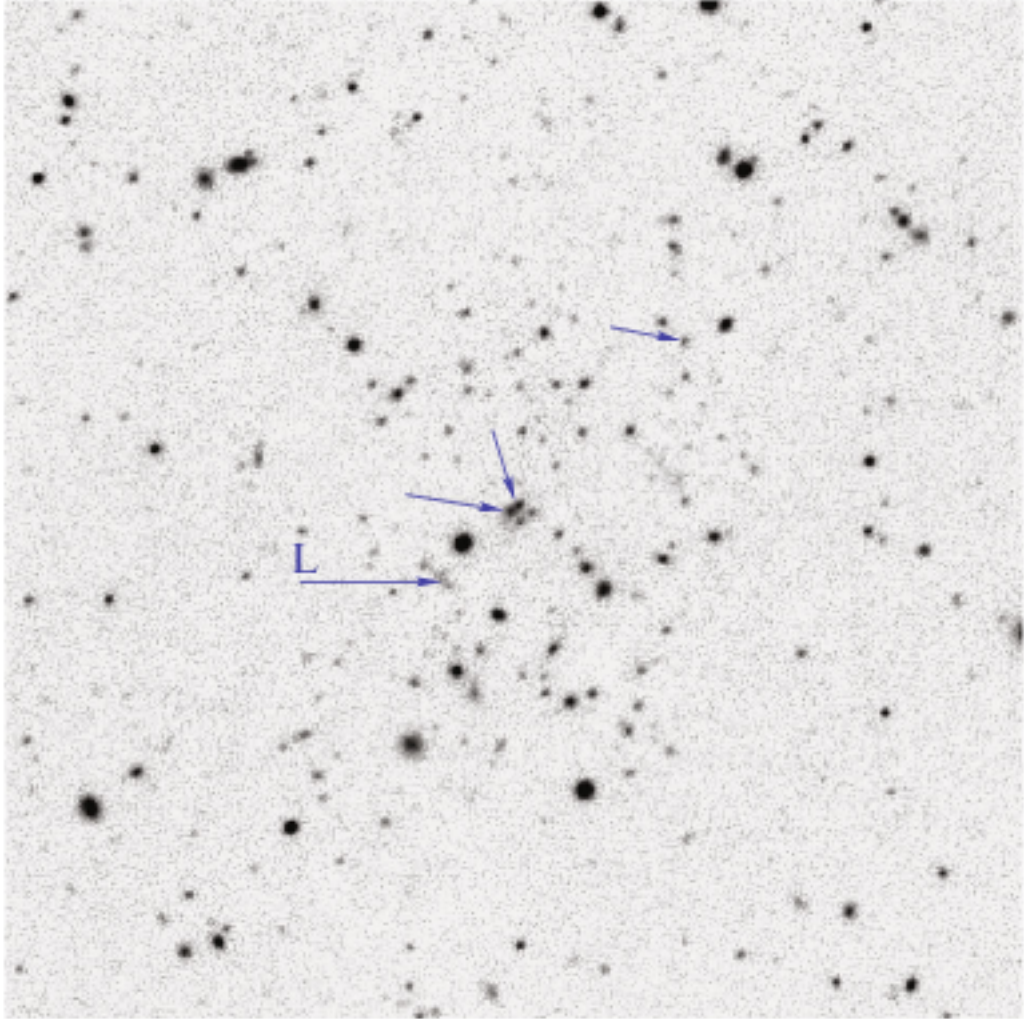


Figure 4.33. Optical image of the B18 cluster candidate. The unlabelled arrows point to the galaxies with spectroscopic measurements and the arrow labelled ‘L’ points to the very faint arc corresponding to a lensed galaxy at redshift $z = 4.262$. This image is centred on the B18 cluster candidate and is $3' \times 3'$. Authors did not specify north and east directions.

CHAPTER 4

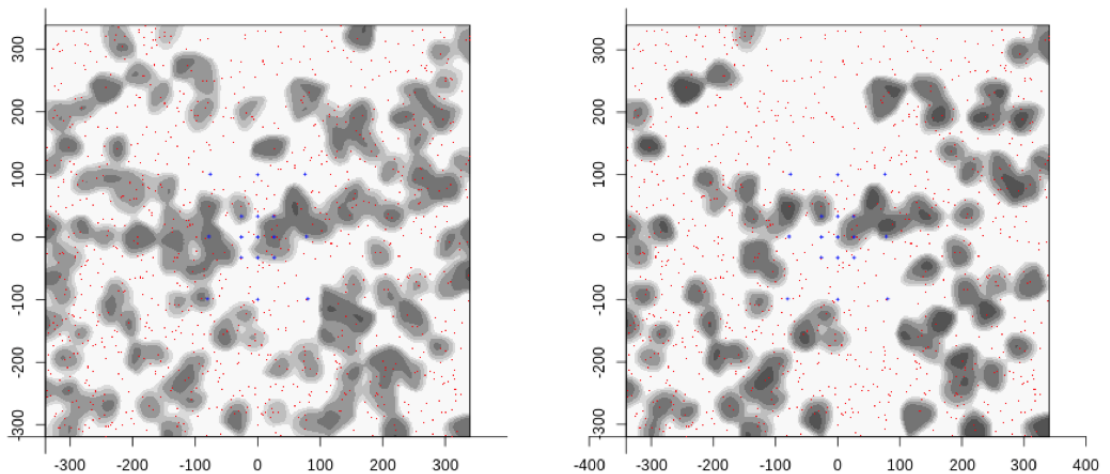


Figure 4.34. MgII images centred on the B18 cluster candidate created using ZM-comb and smoothed using a Gaussian kernel (11 Mpc). Grey contours represent the flat-fielded density values of the MgII absorbers, increasing by a factor of two. Red dots represent the background QSOs and the blue dotted squares outline a reference grid defined in Section 3.4. Axes are measured in proper size Mpc scaled to the present epoch. Left panel: MgII image in the redshift interval $z = 0.763 \pm 0.1$. Right panel: MgII image in the redshift interval $z = 0.763 \pm 0.049$, corresponding to a redshift thickness of 282 Mpc in the present epoch. In both plots there is an intriguing arc of absorbers travelling across the width of the image.

CHAPTER 4

spread of absorbers across redshift (i.e., MgII absorbers closely linked in tp-x and tp-y coordinates but spread out along the redshift axis). Alternatively, it could imply that the dense stripe region could peak at a different central redshift.

Here we investigate whether there is a peak redshift for this particular dense stripe. This was done by stepping through overlapping redshift slices by 50% between $z = 0.665 \pm 0.049$ to $z = 0.861 \pm 0.049$ in the field centred on the B18 Cluster candidate in tp-x and tp-y coordinates, with the usual FOV size, see Figure 4.35. All four plots from Figure 4.35 and the right-hand panel of Figure 4.34 are visually compared, and it is found that the dense stripe feature is most prominent in the central redshift $z = 0.812$ (bottom, left-hand panel of Figure 4.35). In this image the feature can be more accurately described as a giant arc as it extends across the entire image in a curved, arc shape; hereafter referred to as the ‘Giant Arc’. It is quite possible that this arc extends further since it appears that the image cuts into the edges of the arc. Therefore, in order to view the full arc, the image FOV size must be increased. This was done by doubling the tp-x and tp-y offsets, and then tripling them, see Figure 4.36. Note, doubling and tripling the tp-x and tp-y offsets is not strictly the same as doubling and tripling the entire FOV since the MgII images are plotted in tangent-plane coordinates and the RA and Dec coordinates are plotted on a sphere. That is to say, a certain level of warping is introduced once the absorbers are plotted on the tangent-plane, see Section 3.4. The Giant Arc can now be viewed in its full extent from the MgII images in the larger FOV. In these images the Giant Arc appears to extend up to 1 Gpc. Provided this arc is real, this then exceeds the size of most of the LSS known in the literature and is comparable to the largest structures known in the Universe, Gott et al. (2005), Clowes et al. (2013), Balázs et al. (2015). The techniques to assess the reality of such a structure in MgII have not yet been created, but so far a set of preliminary methods for MgII analysis have been built, which are used in this thesis. Later I will discuss the Giant

CHAPTER 4

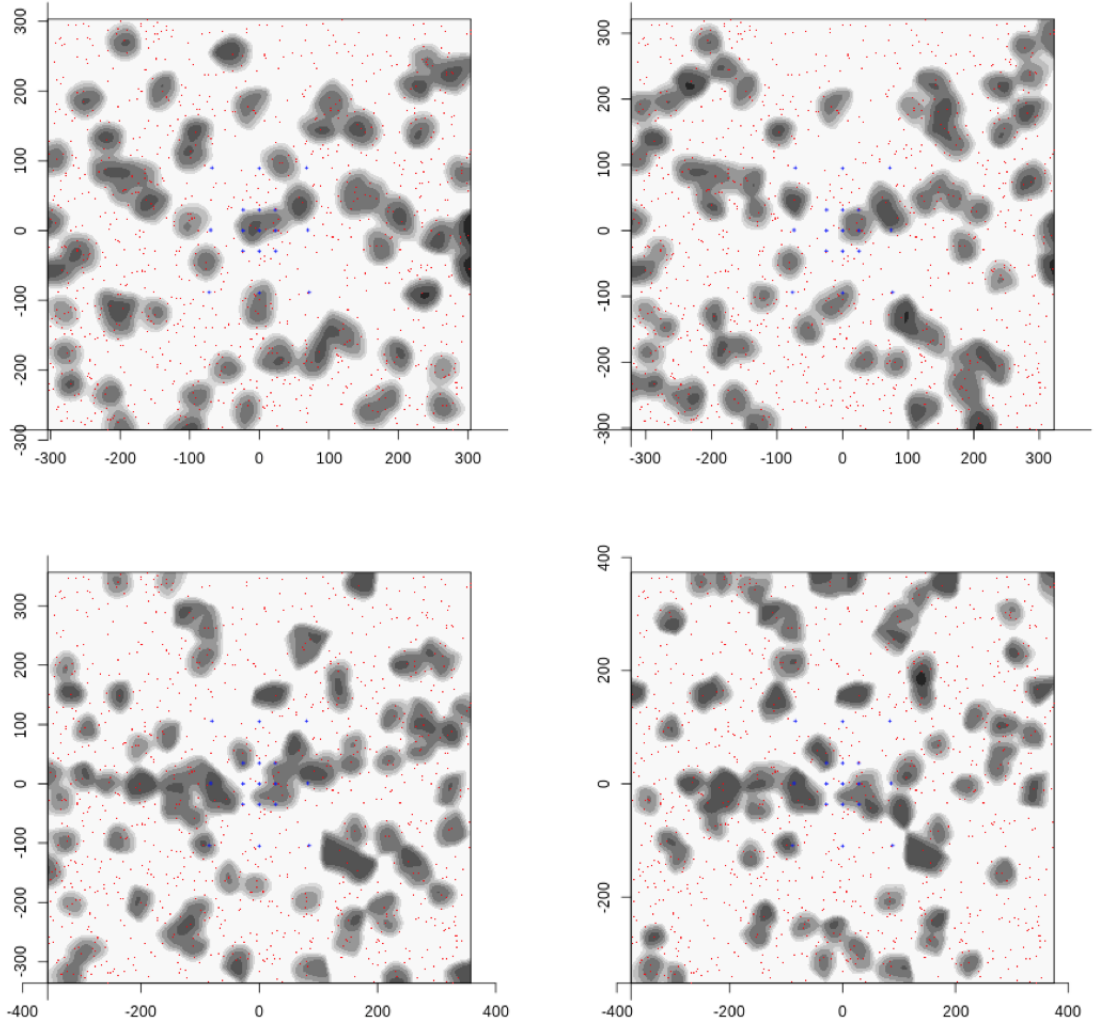


Figure 4.35. MgII images centred on the B18 cluster candidate created using ZM-comb and smoothed using a Gaussian kernel (11 Mpc). Grey contours represent the flat-fielded density values of the MgII absorbers, increasing by a factor of two. Red dots represent the background QSOs and the blue dotted squares outline a reference grid. Axes are measured in proper size Mpc scaled to the present epoch. Top left panel: B18 cluster candidate in the redshift interval $z = 0.665 \pm 0.049$. Top right panel: B18 cluster candidate in the redshift interval $z = 0.714 \pm 0.049$. Bottom left panel: B18 cluster candidate in the redshift interval $z = 0.812 \pm 0.049$. Bottom right panel: B18 cluster candidate in the redshift interval $z = 0.861 \pm 0.049$.

CHAPTER 4

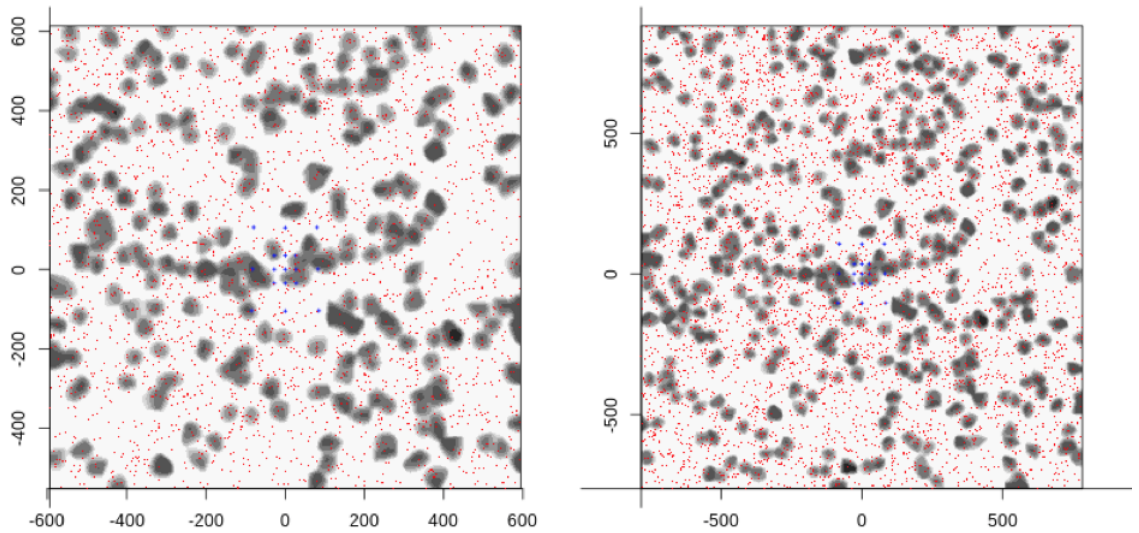


Figure 4.36. MgII images centred on the Giant Arc in the redshift interval $z = 0.812 \pm 0.049$ created using ZM-comb and smoothed with a Gaussian kernel (11 Mpc). Grey contours represent the flat-fielded MgII absorbers, increasing by a factor of two. Red dots represent the background QSOs and blue dotted squares outline a reference grid defined in Section 3.4. Axes are measured in Mpc scaled to the present epoch. The RA and Dec offsets have been doubled (left) and tripled (right) to see the full extent of the Giant Arc.

CHAPTER 4

Arc, and the plans for future work, in Chapter 5.

The paired-combined databases (R-field-all and ZM-field-all) can be used to assert confidence in the absorbers in the field of the Giant Arc. This is because the paired-combined databases select only those absorbers that are in common to the two independent MgII detection algorithms, Z&M and R16. Figure 4.37 shows the MgII image of the Giant Arc in the paired-combined database. Notice that the absorbers in the Giant Arc itself are not erased, but in fact they now stand out more against the background of reduced absorbers. This indicates that the absorbers in the arc are more likely to be real and the absorbers around the arc may be noise from spurious detections. The Giant Arc still extends up to 1 Gpc in present epoch values which is remarkable for a structure at high redshift. The length and connectivity of the absorbers is impressive to the eye and may even raise some questions for Cosmology. So far the standard model seems to suggest that LSS on large enough scales is homogeneous and isotropic; however, a giant arc extending up to 1Gpc in length would suggest that the Universe is not quite so homogeneous on large scales. Additionally, the Giant Arc is at a redshift when the Universe was approximately half its current age, meaning much less time for evolution and gravitational collapse. The Sloan Great Wall (SGW) is about half the size of the Giant Arc and at a redshift of $z = 0.073$, Gott et al. (2005); it is long and curved rather much like the Giant Arc, therefore, perhaps the Giant Arc is a precursor to a structure like the SGW. More rigorous and objective testing will need to be run on this structure as it is particularly striking. In addition, the implications of this Giant Arc for Cosmology will be explored.

The confinement of the Giant Arc in redshift was tested by incrementally decreasing the thickness of the redshift slice and observing at which point the Giant Arc was no longer visible. It was found that the LHS of the arc is much more confined in the z -axis than the RHS as the LHS survived the redshift reduction up to

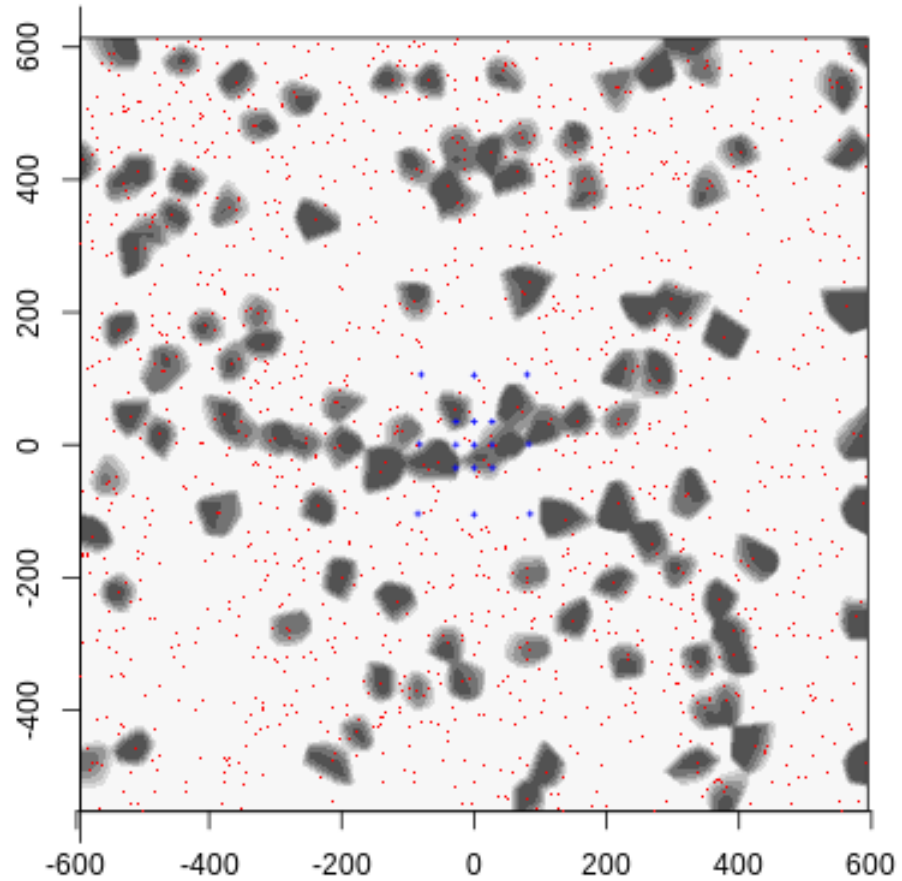


Figure 4.37. MgII image centred on the Giant Arc in the redshift interval $z = 0.812 \pm 0.049$ created using ZM-field-all and smoothed using a Gaussian kernel (11 Mpc). Grey contours represent the flat-fielded MgII absorbers, increasing by a factor of two. Red dots represent the background QSOs and blue dotted squares outline a reference grid defined in Section 3.4. Axes are measured in proper size Mpc scaled to the present epoch. The Giant Arc is still present even in the reduced, paired, combined database.

CHAPTER 4

$\Delta z = \pm 0.01$ corresponding to a redshift thickness ~ 56 Mpc at present epoch, see left-hand panel of Figure 4.38. However, the RHS of the arc was almost immediately erased below a redshift thickness of 282 Mpc (present epoch). This suggests that, while the Giant Arc appears to be quite symmetrical at the face-on-view, it is asymmetrical if one were to look at the Giant Arc at the redshift-RA plane-of-view. This could imply that the left half of the Giant Arc is evolving faster than the right half. Furthermore, the centre of the arc (slightly more left than right) managed to withstand a reduction to $\Delta z = \pm 0.005$ corresponding to a redshift thickness of ~ 28 Mpc at present epoch, see right-hand panel of Figure 4.38. In due course we aim to use a three-dimensional visualisation software for the MgII method that will allow the structure along the z-axis to be examined, as well as the structure face on. However, at present, simply using varying thicknesses of the redshift slice and altering the central redshift is enough to gain an idea of the three-dimensional structure of the MgII absorbers. In two-dimensions the Giant Arc is remarkably symmetrical, however, this is not the case in three-dimensions. It is curious as to how one side of this structure is seemingly much more ‘evolved’ and compact than the other (note, in the review of S12 in Chapter 4, it is suggested that lower redshift structures are more dense due to evolution and gravitational collapse); this feature can be explored further in due course to try to understand what processes are involved in producing the Giant Arc.

The strong absorbers ($W_\lambda > 0.6$) in the Giant Arc field are investigated, and it is found that the strong absorbers favour the LHS of the arc, see Figure 4.39. It is particularly interesting when one notes that not only the strong absorbers favour the LHS of the Giant Arc, but the absorbers on this half are also much more confined in redshift. This warrants further investigation of whether there is a trend for the denser regions of MgII absorbers to be made up preferentially of strong absorbers. Furthermore, perhaps there is not only a correlation, but potentially one causing

CHAPTER 4

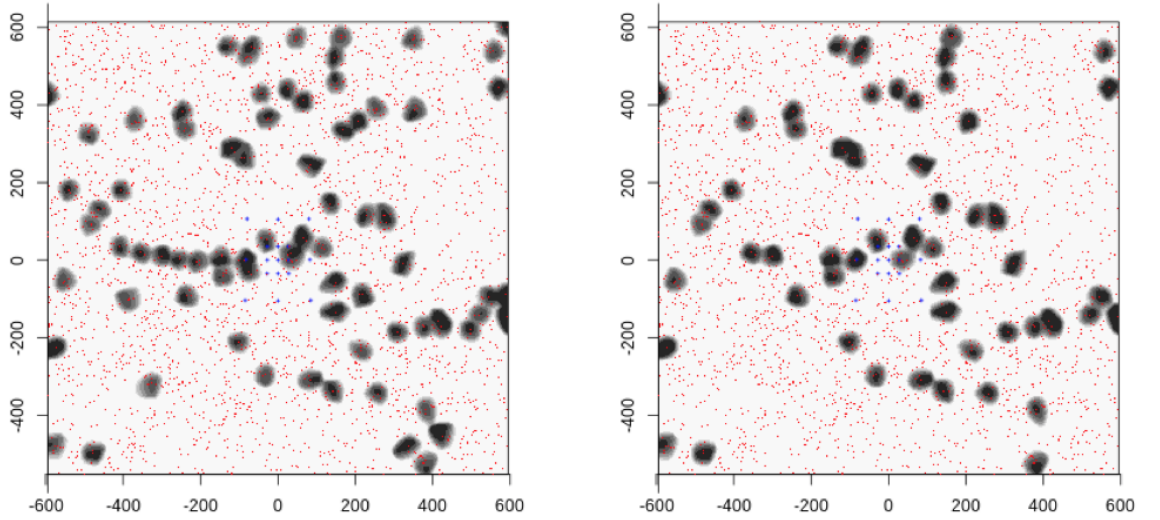


Figure 4.38. MgII images centred on the Giant Arc, in a FOV with double the usual RA and Dec offsets, created using the ZM-comb database and smoothed with a Gaussian kernel (11 Mpc). Grey contours represent the density distribution of the MgII absorbers, increasing by a factor of two, flat-fielded and smoothed. Red dots represent the background QSOs and blue dotted squares, smaller and larger, outline a reference grid. Axes in present epoch, Mpc values. Left: MgII image in the redshift interval $z = 0.812 \pm 0.01$. Right: MgII image in the redshift interval $z = 0.812 \pm 0.005$. The right-hand side of the Giant Arc disappears before the left-hand side indicating that the left-hand side of the Giant Arc is more refined in redshift.

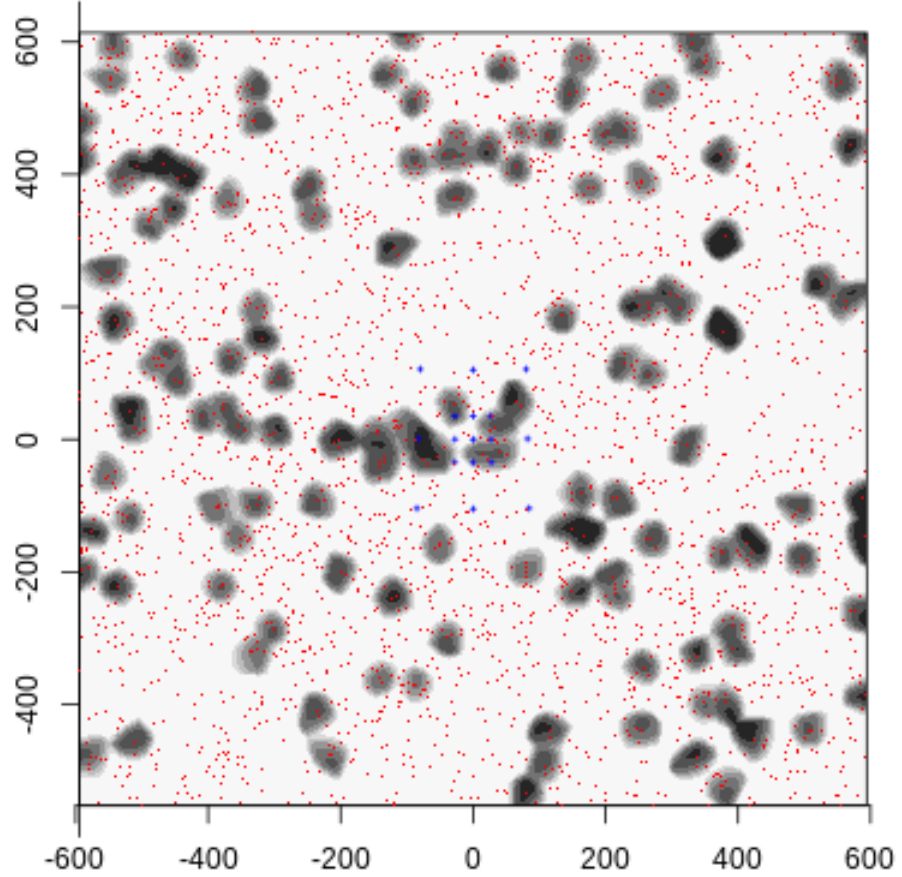


Figure 4.39. Strong MgII absorbers ($W_\lambda > 0.6$) centred on the Giant Arc, with double the usual RA and Dec offsets, in the redshift interval $z = 0.812 \pm 0.049$ created using ZM-comb and smoothed using a Gaussian kernel (11 Mpc). Grey contours represent the flat-fielded MgII absorbers, with contours increasing by a factor or two. Red dots represent the background QSOs and blue dotted squares outline a reference grid defined in Section 3.4. Axes are measured in proper size Mpc scaled to the present epoch. The left-hand side of the Giant Arc mostly comprises strong MgII absorbers, whereas the right-hand side comprises of either medium or weak absorbers. It is interesting to note that the well refined side of the Giant Arc in redshift is the same side as that with the strong absorbers.

CHAPTER 4

the other; for instance, it could be envisioned to some extent that denser regions of MgII lead to stronger absorbers. In Figure 2.7 in Section 2.2 of this thesis, a diagram taken from Churchill et al. (2005) shows how the distance from the centre of a galaxy may affect the different classes of absorbers. Here, I will make similar suggestion, albeit tentatively, that the strength of absorbers may be correlated to the density environment, i.e., the higher density environments lead to strong MgII absorption. There may be many other factors affecting the apparent correlation to dense environments and strong MgII absorbers (such as, the Z&M databases have a generally high proportion of strong absorbers in their databases), but further investigation could introduce another avenue for the potential of MgII in Cosmology.

Noticing that the Giant Arc feature appears almost horizontal in the MgII image presents the opportunity to calculate the frequency of absorbers as they vary across tp-y coordinates. Figure 4.40 was produced by dividing the Giant Arc field (with triple offset values) into bins of size 22 Mpc that span the tp-y coordinates. The histogram plots the number of absorbers in each bin. The most protruding peak is slightly to the right of the centre value, which directly corresponds to the Giant Arc feature. The significance of the largest peak corresponding to the Giant Arc compared with the mean value of absorbers in the histogram of the whole field produces a 3.32σ significance. Importantly, one must remember that this is only an initial estimate of the true overdensity and one must also note the limitations of this particular model. For instance, the model does not consider that the Giant Arc is not completely horizontal; in fact, this assumption is an over-simplification that would lead to an underestimation since the Giant Arc feature is clearly curved and the absorbers on the edges will not be included in the central histogram peak. Additionally, the Giant Arc does not extend to the edges of the MgII image in the right-hand panel of Figure 4.36; this will most likely produce another underestimation since the edges of the Giant Arc will be at a lower density than the arc itself,

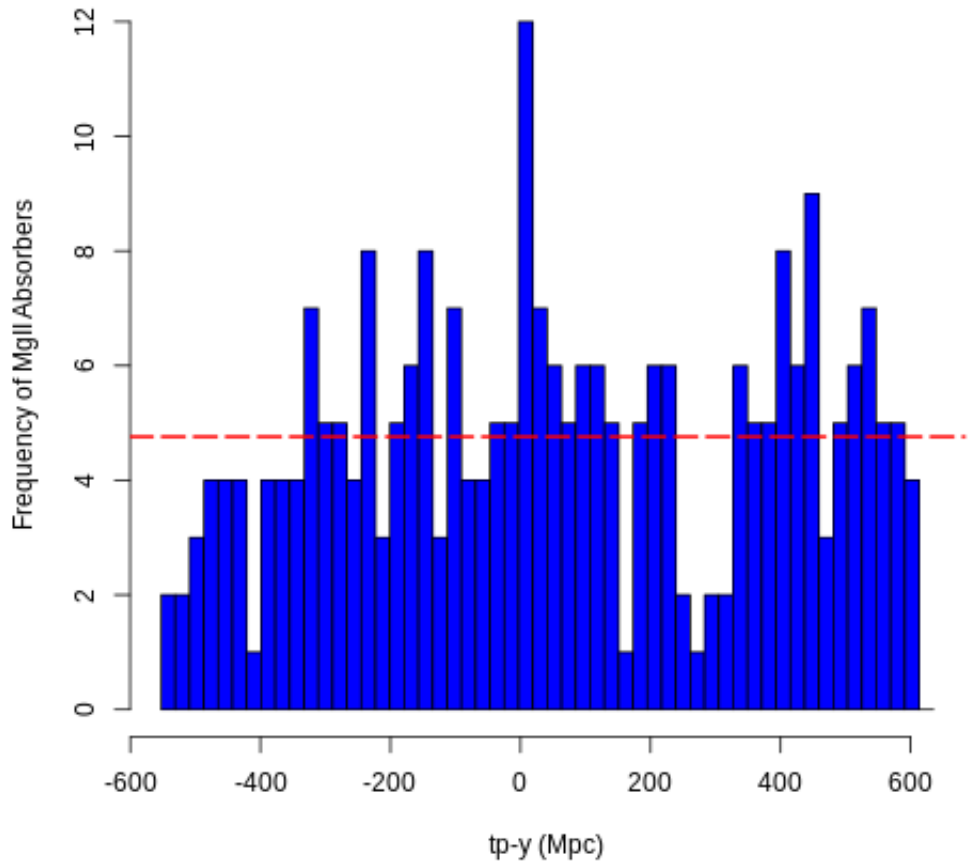


Figure 4.40. Histogram of the frequency of absorbers across tp - y coordinates in the left-hand panel of Figure 4.36 (MgII image centred on Giant Arc with offset values increased by a factor of two and created using ZM-comb) restricted to `tp_in = TRUE`. The histogram has a bin size of 22 Mpc corresponding to the 2σ diameter of a single absorber in the MgII image once the smoothing scale has been applied. The calculated mean frequency is plotted over the histogram by a red, dashed line at 4.80. The large peak, just right of the zero value, corresponds to the Giant Arc.

CHAPTER 4

reducing the overall density of that particular bin in the histogram. Another limitation of using a histogram is that the range of frequency values is dependent on the binning size selected; this then has the effect of either emphasising or masking frequency peaks in the data. In this calculation the histogram was split into approximately 55 bins, corresponding to a bin size of 22 Mpc which is the 2σ diameter of a single absorber in the MgII image once the smoothing scale has been applied. An inevitable feature of the MgII method at this time is that the available background probes fluctuate across the whole sky. Therefore, the available background probes may potentially be responsible for the frequency peak in the histogram of absorbers. In this case, it can be easily shown that the central frequency peak of absorbers in the histogram does not correspond to some artefact in the probes by simply checking the histogram of the number of background probes divided into bins of size 22 Mpc that span the tp-y coordinates in the Giant Arc field. In Figure 4.41 there is no protruding peak that aligns with the Giant Arc, so the problem of whether the Giant Arc feature is an artefact of the background probes can be eliminated.

As mentioned earlier, the histogram method of analysis for the Giant Arc introduces an excess of low-density absorbers by including the edges of the MgII image which the Giant Arc does not reach. A solution to this problem would be to make a rectangular selection around the Giant Arc and assess the overdensity in this selection compared with the density of the whole field. TOPCAT (version 4.6-3), Taylor (2005), is used to make the rectangular selection around the Giant Arc, see Figure 4.42 for the selection that was made. From here the area, number of absorbers and overall density of absorbers per Mpc^2 were calculated for both the rectangle selection and the whole field, see Table 4.4. The expected density in the Giant Arc compared with the actual density in the Giant Arc produces a 4.19σ significance. Additionally, to rule out whether the overdensity in the MgII absorbers is a consequence of an overdensity in the background QSOs, the same rectangular selection method was

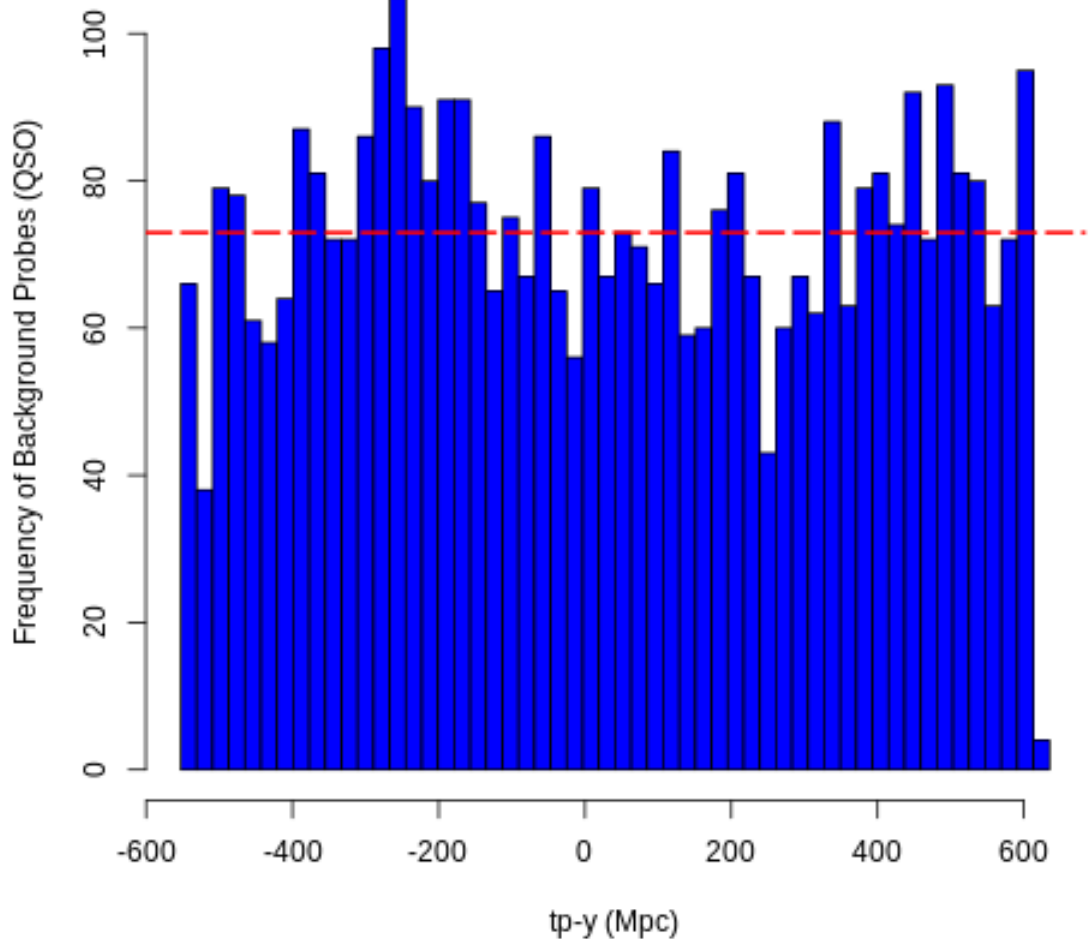


Figure 4.41. Histogram of the frequency of available background probes across $tp-y$ coordinates in the left-hand panel of Figure 4.36 (MgII image centred on Giant Arc with offset values doubled and created using ZM-comb) restricted to $tp_in = \text{TRUE}$. The histogram has a bin size of 22 Mpc corresponding to the 2σ diameter of a single absorber in the MgII image once the smoothing scale has been applied. The red dashed line represents the mean frequency at 73.0. There is no sign of a large peak, just right of the zero value, that would otherwise correspond to the Giant Arc. This indicates that the MgII absorbers in the Giant Arc are not a result of a large peak of available background QSOs lining up with the Giant Arc.

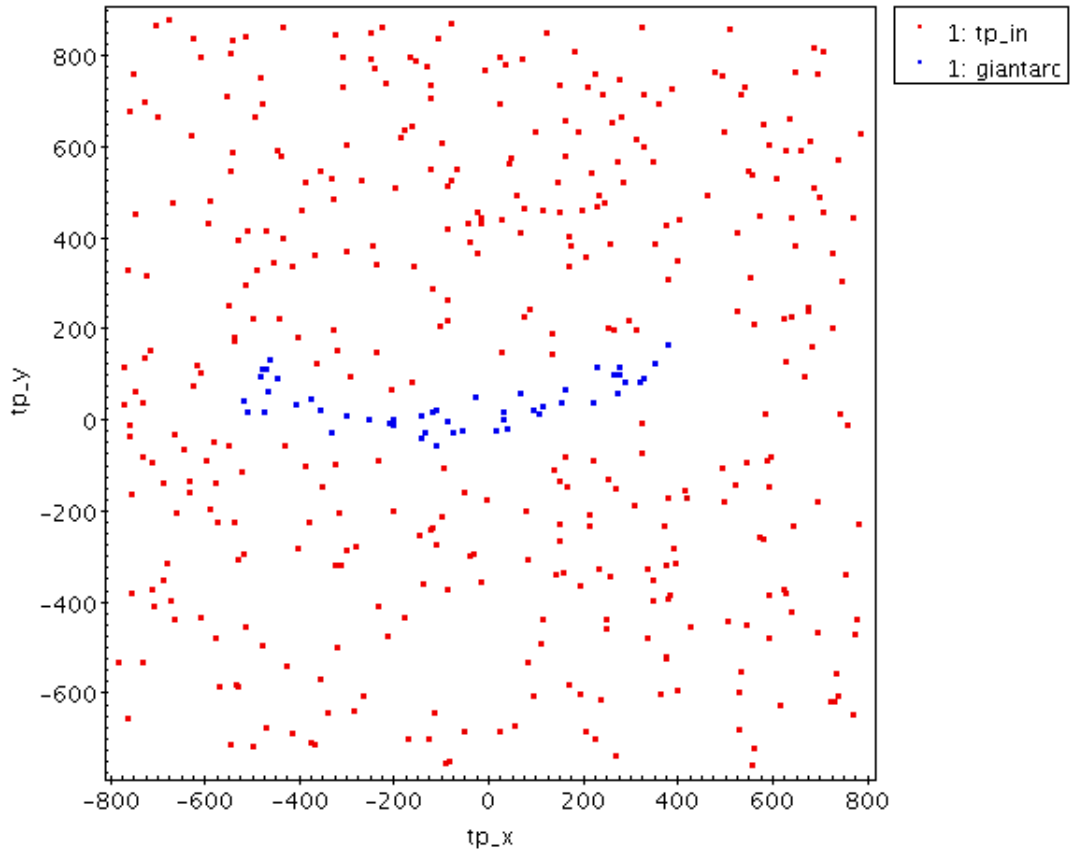


Figure 4.42. TOPCAT (version 4.6-3) image of the MgII absorbers in the field containing the Giant Arc. Blue points represent the MgII absorbers belonging to the Giant Arc, selected by eye, and red points represent all the other MgII absorbers in the field.

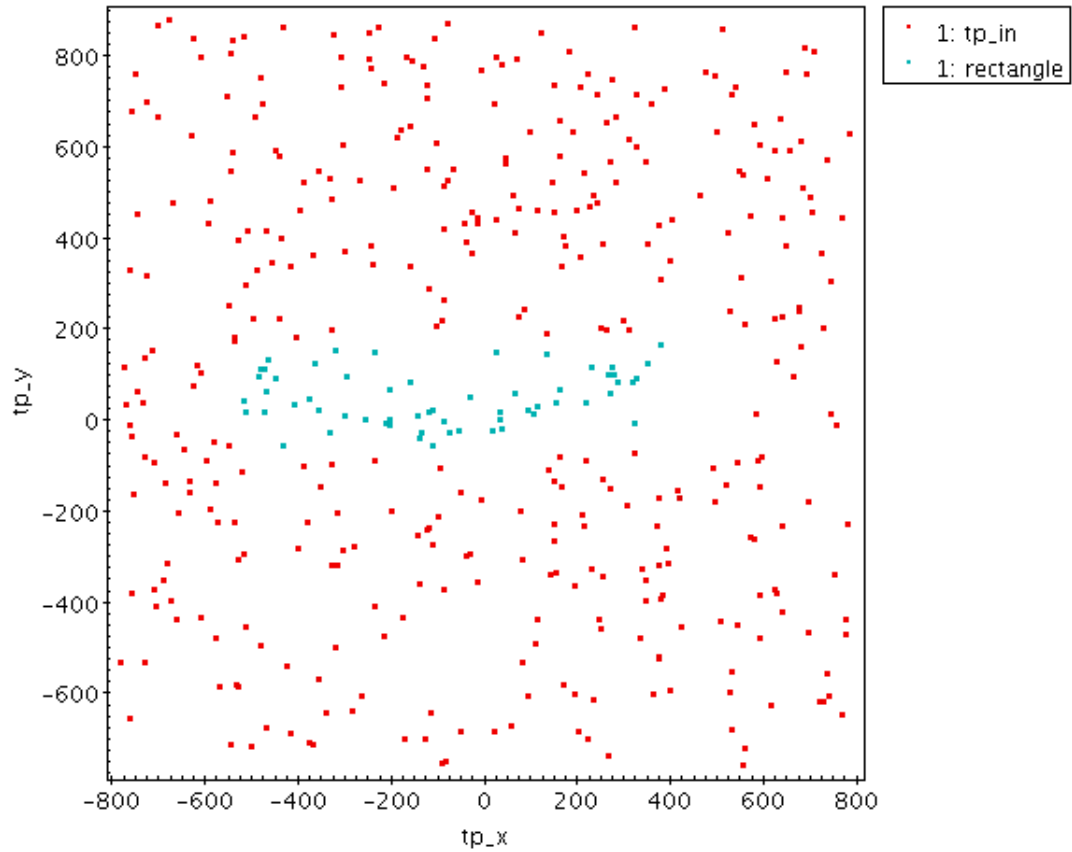


Figure 4.43. TOPCAT (version 4.6-3) image of the MgII absorbers in the field containing the Giant Arc. Turquoise points represent *all* the absorbers contained within the rectangle selection encompassing the Giant Arc and red points are all the other MgII absorbers in the field.

CHAPTER 4

Field	Area (Mpc ²)	No. of Abs.	Dens. (Mpc ⁻²)
Whole Field	2553667	442	0.0001730844
Rectangle	198892.4	49	0.0002966428

Table 4.4. Statistical comparisons of the whole field and rectangular selection of absorbers in the field containing the Giant Arc.

tested on the background QSOs; this produced a 1.01σ significance. It is clear now after two simple methods of analysis that the Giant Arc is almost certainly a real and important discovery. Despite the fact that the methods are simple, there are two results that exceed the 3σ level. To represent the significance of the Giant Arc feature properly, the parameters of the arc would need to be defined objectively, and then calculate the number of absorbers in this unique volume. A similar method could be carried out to that which was done in assessing the Huge-LQG, Clowes et al. (2013). Secondly, a model has been chosen to fit what is seen, i.e., assigning statistics after the event has happened, which is then incorporating a subjective element to the statistical analysis. Finally, as mentioned previously, the rectangular selection model does not consider how the available background probes affect the distribution of intervening MgII. One solution that is currently being explored is to use the pixels in the flat-fielded MgII images, as these pixels give the density values of the absorbers with the number of available background probes taken into consideration; this will be discussed further in Chapter 5.

In conclusion to Target 5 of this thesis I have presented an impressive extension of an SZ cluster which exceeds the ~ 370 Mpc scale of homogeneity, see the following references: Yadav et al. (2005), Sarkar et al. (2009), Yadav et al. (2010), Laurent et al. (2016), Ntelis et al. (2017), and Gonçalves et al. (2018). The LSS centred on the

CHAPTER 4

SZ cluster reaches up to 1Gpc in its longest length and arches almost symmetrically. It is one of the largest structures observed in the Universe comparable to the Huge-LQG, Clowes et al. (2013). The Giant Arc seems particularly dense and confined along the redshift axis on the LHS and appears to disperse at the RHS. Additionally, the strong absorbers favour the LHS of the arc and it has been suggested that these two factors may be linked and worth further investigation. Two simple statistical methods of analysis were performed on the Giant Arc and produced significance above the 3σ level. Therefore, it is recognised that the Giant Arc is almost certainly an awesome discovery worthy of publication (Lopez et al. 2019 in preparation).

4.6 Target 6: Galaxy Cluster associated with LQG at $z = 1.1$

Throughout this thesis it has been demonstrated that the MgII method can be used to locate high redshift galaxy clusters with accurate spectroscopic redshifts. This has been done by collecting a small sample of previously documented cluster and supercluster candidates and analysing the images that are produced from the MgII method. Often photometric redshift measurements can lead to large error bars of the order $\Delta z = \pm 0.08 (1 + z)$ according to a study done by Fernández-Soto et al. (2001). Note, this study was done for photometric redshifts measured in seven different bands. In this Chapter, an example of a photometric galaxy cluster documented by Tanaka et al. (2001) at a redshift $z = 1.1$ which is believed to be in association with five of the 23 QSOs in a LQG found by Crampton et al. (1989) in the 1338 + 27 field is investigated. Firstly, a brief overview of both papers – Crampton et al. (1989) and Tanaka et al. (2001) – will be presented.

CHAPTER 4

Background

Crampton et al. (1989) (hereafter C89) used the Multiple Mirror Telescope (MMT) in Arizona to produce a catalogue of 248 QSO candidates with spectroscopic redshifts out of a sample of 270 QSOs. The primary aim was to observe QSO clustering in isolated groups; previous works had indicated that there could be clustering of QSOs on small scales which may be a property of QSOs in general, Crampton et al. (1987), Iovino & Shaver (1988) and Shanks et al. (1988). In C89 the authors observe a sample of QSOs in a small field, ID 1338+27 field, and find that in general there is no significant clustering amongst the QSOs. However, one particular group of 23 QSOs were found to lie in the same redshift interval, $1.0 < z < 1.2$, suggesting that they had some association with each other, see Figure 4.44. The LQG was investigated further and C89 discover that the overdensity signal produced by the 23 QSOs cannot be replicated by a simulation, implying that the apparent clustering between 23 QSOs within the same field and redshift slice is a significant and rare result. The authors believed that there would likely be some galaxy clustering in association with the LQG that should be further investigated.

Tanaka et al. (2001) (hereafter T01) investigate the highest density region in field 1338+27, which is small area containing five of the 23 QSOs from C89 located in the north-east, see Figure 4.45. The RA and Dec of the central point of the five QSOs is approximately 204.5° and 28.1° . T01 observe the small rectangular area with two different scan regions; scan A encompasses four of the five QSOs and scan B includes only one of the QSOs so that it can be used as a comparison field. The two scan regions are measured in the *I* and *R* bands using the SPICAM at the Apache Point Observatory. Note, only two passbands are used in T01, which implies larger photometric redshift errors than stated by Fernández-Soto et al. (2001). Each scan moves at approximately $3''$ a second; totalling 96 seconds per object then each observation was repeated five times in each band. The primary objective for T01

CHAPTER 4

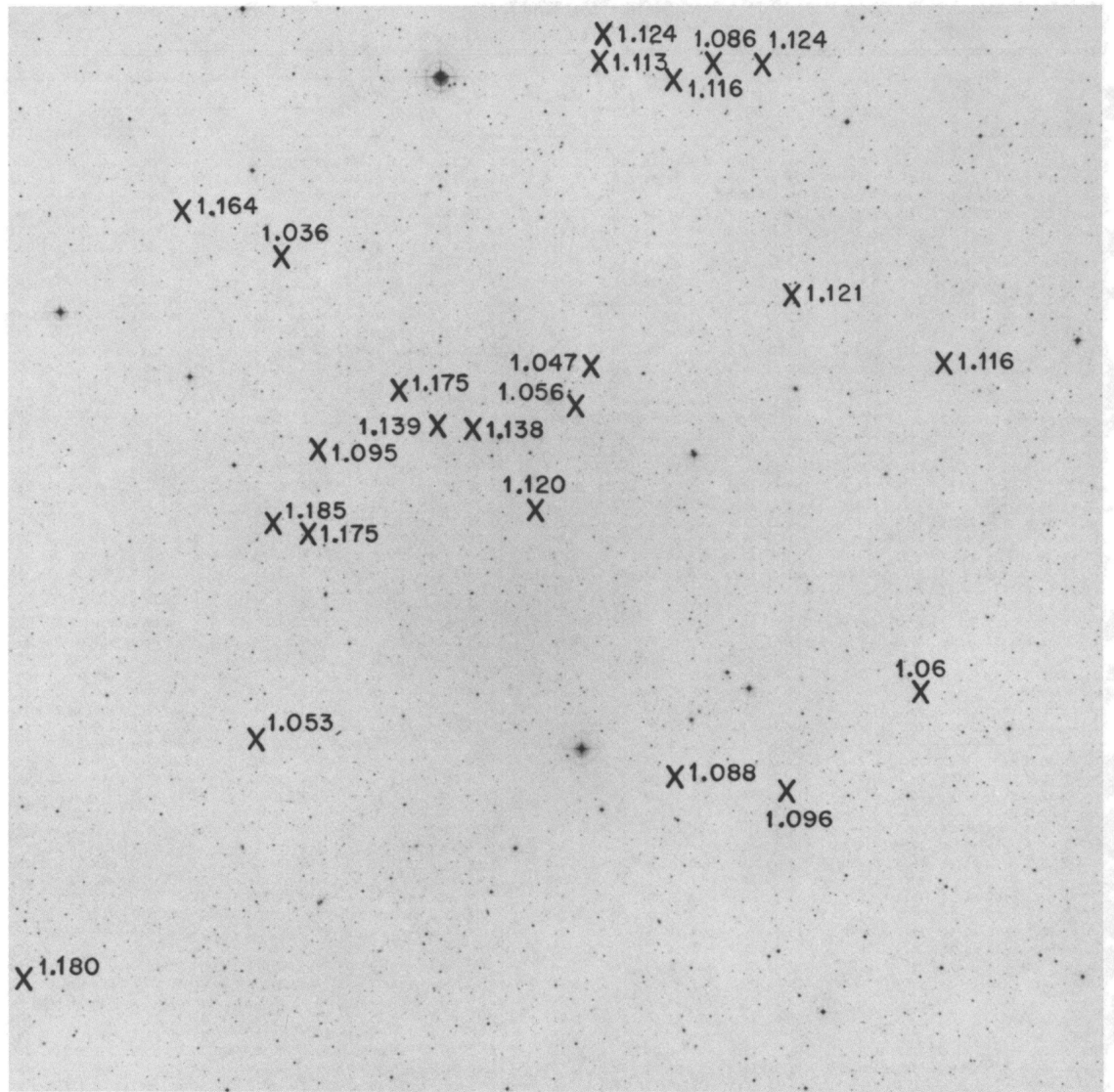


Figure 4.44. Image taken from C89. Projection of the 23 QSOs on the sky (east is left and north is top) on a field that spans approximately $2.2^\circ \times 2.2^\circ$.

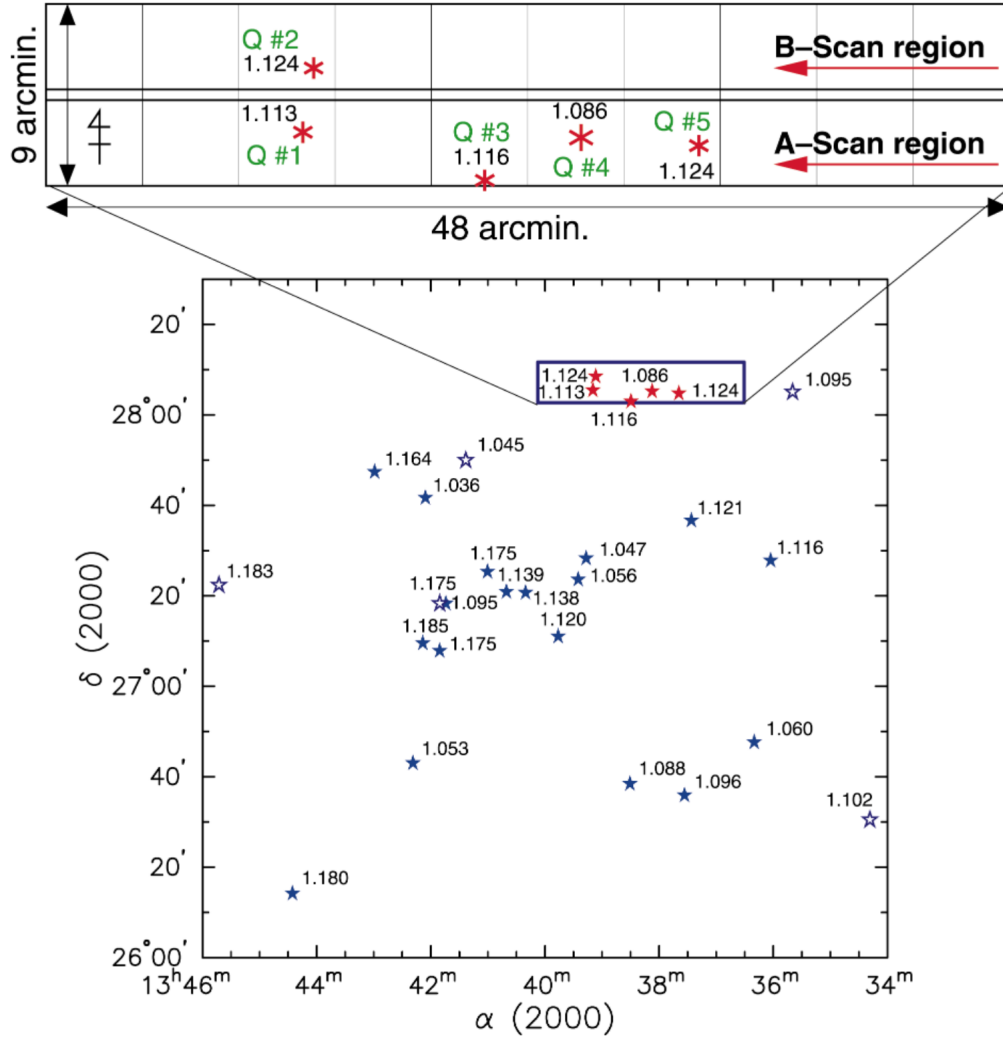


Figure 4.45. Image from T01. Field 1338+27 with a small rectangle encompassing the selection of five QSOs that are investigated in T01. The small rectangle was observed using two separate scan regions; scan A includes four of the five QSOs and scan B includes only one so that it can be used as a comparison field.

CHAPTER 4

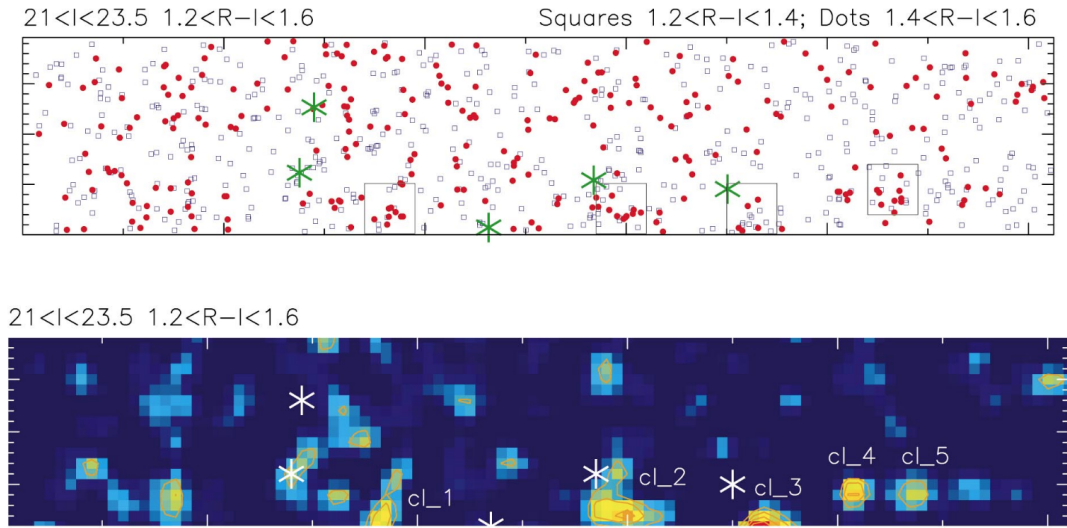


Figure 4.46. Image from T01. Top panel: position of the galaxies in scan region A. Red dots indicate the galaxies with $1.2 < R - I < 1.4$ and squares indicate the galaxies with $1.4 < R - I < 1.6$. Green asterisks mark the QSOs and the small inset squares mark out areas which were used in further analysis. Bottom panel: Contour map of the density amplitude of galaxies in scan region A. Contour lines indicate the 2σ , 3σ and 4σ levels. Five potential galaxy clusters are marked on this map.

was to investigate the differences between scan A and scan B and determine whether there is any significant galaxy clustering in association with the QSOs.

The galaxy candidates detected in both scan regions were analysed in colour and magnitude to determine their photometric redshift measurements. Additionally, a threshold limit was set such that the galaxies being selected had magnitudes $I > 22$ and a colour between $1.2 < R - I < 1.6$, which ensures a selection of cluster galaxies at redshift $z \sim 1.1$. At first T01 plot the results of the galaxies that fell within the threshold limits on a map against the QSOs and no clear correlation or association was evident. However, the density map of galaxy candidates proved to be much more aligned with the QSO group, see Figure 4.46. The galaxy cluster candidates with significance above 2.5σ are marked on the lower panel of Figure 4.46. The most

CHAPTER 4

prominent overdensity at cl_2 is actually a galaxy cluster previously documented by Yamada et al. (1997) and Tanaka et al. (2000) thought to be located at the redshift $z = 1.1$. Upon further investigations into the colour and magnitude distribution of the galaxy cluster candidates, it was found the cl_4 was much brighter and bluer than the other four galaxy cluster candidates. This suggests that this galaxy cluster is in fact located at a lower redshift, perhaps at about $z = 0.7$. However, bluer and brighter galaxies may be an indicator of star forming galaxies and therefore can be located at higher redshifts. For the sake of reducing uncertainty, T01 exclude these brighter and bluer galaxies. Table 4.5 gives information on the number of red galaxies in each of the cluster candidates (now excluding cl_4 altogether) and an estimate to the number of Abell galaxies (star forming blue galaxies) expected based on the Hill & Lilly (1991) Abell richness, see T01 for further information. T01

Cluster ID	No. Gal. (red)	No. Abell
cl_1	8 ± 3	< 0
cl_2	10 ± 5	0
cl_3	14 ± 5	1
cl_5	11 ± 5	0

Table 4.5. Number of red galaxies (second column) and expected number of star-forming blue galaxies (third column) of each of the identified galaxy clusters in Tanaka et al. (2001).

then investigated the luminosity function of the red galaxy cluster candidates and find that when compared with the Virgo cluster, the data in each cluster fits well

CHAPTER 4

with what is generally expected for clusters comprising passively evolving galaxies with ages ~ 3.5 Gyr and at a redshift of 1.1. Finally, T01 find that the two-point correlation function for the galaxy clusters produces a strong clustering signal. However, when the red galaxies are removed from this study, the clustering signal becomes much weaker, implying that the large clustering signal is a result of the galaxy cluster candidates under investigation.

In conclusion, T01 finds that there is a strong galaxy clustering in association with the high density QSO region in the field 1338+27 at $z = 1.1$. Two scan regions, one containing four of the five QSOs, and the other a comparison field, indicate that the former scan region contains strong clustering of galaxies. The photometric measurements were made in two pass bands, R and I , and using various methods of analysis T01 show that the galaxy clusters comprise passively evolving, red galaxies. The bright, blue galaxies were excluded from the analysis as it is unclear whether they are star forming regions or located at a lower redshift range. The rest of this Section will be to test the T01 galaxy clusters region via the MgII method.

MgII Analysis

A first glance of the T01 galaxy clusters in MgII absorbers yields a single absorber in the central coordinates, see Figure 4.47. This is not an expected or substantial MgII signal given that there should be a galaxy cluster lying in the centre of the MgII image. Perhaps this is the fault of the MgII method, however, at this point it has been repeatedly demonstrated that the MgII does highlight the underlying mass distribution and it is unlikely that the lack of signal corresponding to the galaxy cluster is a fault of the MgII method. Another consideration to make is that of the sky lines; in Section 4.1 the MgII method seemingly failed to detect the supercluster candidate in the COSMOS field at redshift 1.12. It was then discussed that this could be a result of night sky emission lines masking the MgII signal, see Section 3.2, potentially combined with the low completeness at 6000 \AA (or a MgII absorber

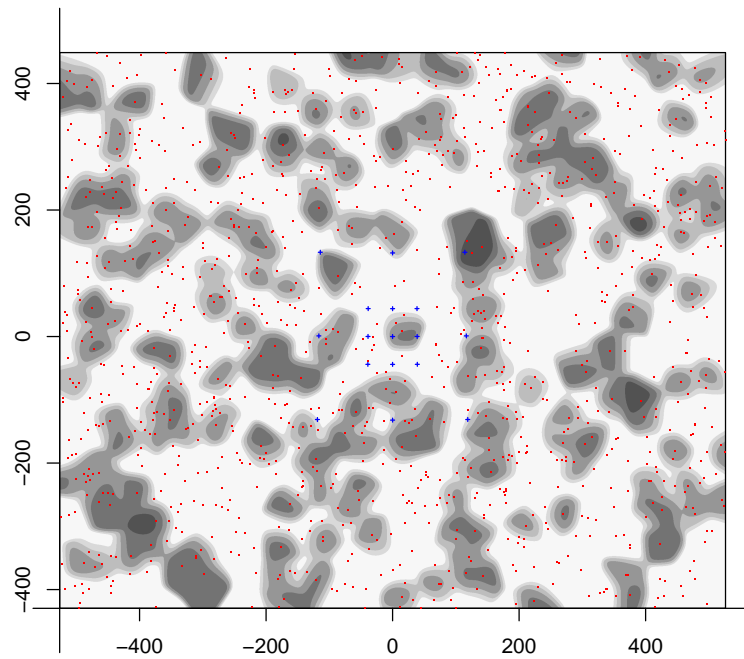


Figure 4.47. MgII image centred on the T01 galaxy clusters in the redshift interval $z = 1.1 \pm 0.1$ created using ZM-comb. Grey contours represent the flat-fielded MgII absorbers, increasing by a factor of two, with both the MgII absorbers and background probes smoothed using a Gaussian kernel (14 Mpc). Red dots represent the available background probes and the blue dotted squares outline a reference grid described in Section 3.4. Axes are measured in proper size, present epoch Mpc.

CHAPTER 4

at redshift $z = 1.1$) due to the red-blue spectrograph transition that make observing MgII absorbers at redshift $z = 1.1$ particularly challenging. In Figure 4.47 there are clearly many absorbers in the image, but none that coincide with the centre point. A third consideration that may explain the absence of MgII absorbers at the T01 galaxy clusters centre is the original redshift measurement could be slightly off from the true value. A study done by Fernández-Soto et al. (2001) suggests that photometric redshift measurements may be off up to $\Delta z = 0.08 (1 + z)$ which for redshift $z = 1.1$, this incorporates a minimum error bar of $\Delta z = 0.168$. Additionally, T01 only uses two passband measurements to calculate the redshift of their galaxy cluster, so the Δz would be subsequently worse.

For the next part of the MgII analysis my aim is to see whether the T01 galaxy clusters is centred on a different redshift. This will be achieved by stepping through reasonably broad, neighbouring redshift slices: 0.9, 1.0, 1.2, 1.3 ($\Delta z = \pm 0.1$), Figure 4.48. Note, the smoothing scale is changed depending on the redshift centre, this is explained in Section 3.4.

From all five of the redshift slices, only the top left panel in Figure 4.48 appears to show any sign of associated structure in MgII. Here it is suggested, with caution, that the T01 galaxy clusters documented at redshift $z = 1.1$ is in fact located in the redshift range $z = 0.9 \pm 0.1$. This seems reasonably plausible given the errors on photometric redshift measurements and along with the fact that there is no significant MgII clustering in any of the redshifts between $1.0 \leq z \leq 1.2$, with perhaps $z = 1.3$ showing a slight hint of a MgII overdensity.

The ‘stepping through redshift’ method is used again to further investigate the redshift $z = 0.9 \pm 0.1$, only with a smaller redshift interval, $\Delta z = 0.053$. This selected redshift thickness roughly corresponds to the chosen 282 Mpc (present epoch) thickness that is used throughout this thesis. Three smaller redshift slices around the central redshift $z = 0.9$ each display some form of MgII clustering, see Figure

CHAPTER 4

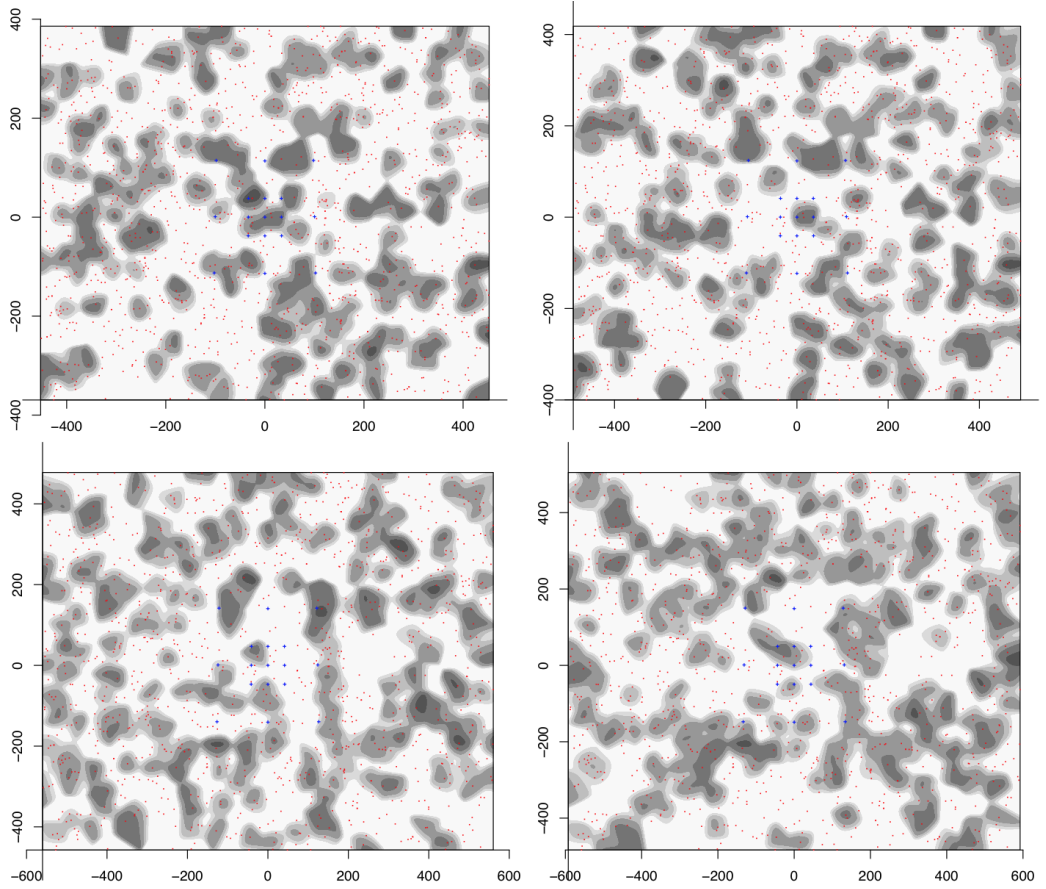


Figure 4.48. MgII images centred on the T01 galaxy clusters created using ZM-comb. Grey contours represent the flat-fielded MgII absorbers, with the density in each contour level increasing by a factor of two. Red dots represent the available background probes and the blue dotted squares outline a reference grid described in Section 3.4. Axes are measured in proper size, present epoch Mpc. Top left: T01 galaxy cluster coordinates in the redshift interval $z = 0.9 \pm 0.1$ smoothed with a 12 Mpc Gaussian kernel. Top right: T01 galaxy cluster coordinates in the redshift interval 1.0 ± 0.1 smoothed with a 13 Mpc Gaussian kernel. Bottom left: T01 galaxy cluster coordinates in the redshift interval $z = 1.2 \pm 0.1$ smoothed with a 15 Mpc Gaussian kernel. Bottom right: T01 galaxy cluster coordinates in the redshift interval $z = 1.3 \pm 0.1$ smoothed with a 16 Mpc Gaussian kernel. The top left panel appears to be the only plot with significant MgII detection in the centre coordinates.

CHAPTER 4

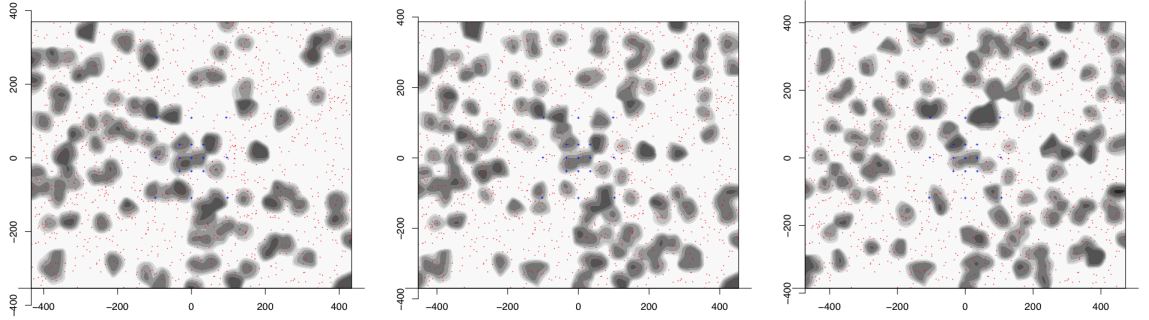


Figure 4.49. MgII images centred on the T01 galaxy clusters in a smaller redshift range. Grey contours represent the flat-fielded MgII absorbers, each contour level increasing by a factor of two, with both the MgII absorbers and background probes smoothed using a Gaussian kernel (12 Mpc). Red dots represent the available background probes and the blue dotted squares outline a reference grid described in Section 3.4. Axes are measured in proper size, present epoch Mpc Left panel: MgII image centred on the redshift 0.85 ± 0.053 . Middle panel: MgII image centred on the redshift 0.90 ± 0.053 . Right panel: MgII image centred on the redshift 0.95 ± 0.053 . The middle and right-hand panel both contain a similar shaped structure in the centre of field indicating they could be part of the same structure.

4.49 Interestingly, the centre MgII absorbers in the middle and right-hand panel of Figure 4.49 contain a similar shaped structure of absorbers. Perhaps this then means that these absorbers are part of the same structure. Since each of the three smaller redshift slices around $z = 0.9$ contain some form of clustering it is difficult to say for certain which, if any, of these are associated with the T01 galaxy clusters.

Due to the multiple clustering of MgII absorbers at different small redshift slices around $z = 0.9$ it is difficult to say for certain where the T01 galaxy clusters is actually located. Despite redshift $z = 1.1$ being a difficult redshift to observe in MgII due to the low completeness, there is MgII clustering found at a slightly lower redshift which seems to suggest that the T01 redshift measurement was overestimated. It could be the case that the MgII method has not been able to pick up the

CHAPTER 4

signal at the specific location of the T01 galaxy clusters, but this cannot be certain. Another note to make is that the MgII method is particularly useful for LSS on the whole which means that observing individual smaller galaxy clusters is a little more complicated. Additionally, it may be of importance to note that in the original analysis of the T01 galaxy clusters, one galaxy was omitted from further study as it appeared much brighter and bluer than the other galaxies. T01 roughly estimated this particular galaxy to be at a redshift $z = 0.7$. If this photometric measurement is also off (or underestimated) then it could be that all five galaxies in the original T01 galaxy clusters selection are part of the same structure at redshift $z = 0.9$. This particular idea is fairly ambitious but amplifies the point that photometric redshift measurements do incorporate this unfortunate trait of large errors. Finally, the T01 paper has been used as evidence in many papers for high-redshift examples of QSOs lying on the peripheries of clusters, Williger et al. (2002), O-03, Haines et al. (2004), Alonso et al. (2008) and Clowes et al. (2012). However, it now seems that this may not be the case anymore, since the MgII analysis provides evidence that the T01 galaxy clusters may not actually lie at the redshift $z = 1.1$.

Once the MgII method has been further refined – a 3D visualisation included, understanding the effect of uneven distribution of background probes, etc – this particular galaxy cluster, and more like these, can be investigated with the MgII method. The MgII method allows measurements of faint galaxies with accurate spectroscopic redshifts so it will be interesting to begin refining structures with photometric redshifts by providing more accurate spectroscopic redshift measurements.

To conclude Chapter 4, I have presented the MgII analysis for six target clusters/superclusters. Four of the six targets showed a detection in MgII. One target led to a null detection, and reasons for this were discussed. The final target was used to test whether MgII can provide more accurate redshift measurements of previously documented photometric clusters, and to test the relation of a LQG to clusters.

Chapter 5

Discussion

In this thesis I have presented a new method of observing the LSS of the universe at high redshift, non-biased to luminosity. The method works by relying on background QSOs as probes to highlight low ionised gas around galaxies. The faint galaxies at high redshifts would usually go unseen as the telescopes available today are not powerful enough to detect them, or require too much telescope time. However, even if the telescopes available today were powerful enough to detect faint, high redshift galaxies, it would be near impossible to detect the galaxies that are detected via the MgII method (MgII galaxies), because the galaxies detected using MgII are inevitably aligned close to a background QSO (the MgII galaxies are detected using background QSOs). The angular separation between a MgII galaxy and the corresponding background QSO decreases at high redshifts. Therefore, observing MgII galaxies at high redshifts becomes extremely difficult as the background QSO essentially ‘drowns out’ the light emitted from a galaxy. In addition, high redshift galaxies are already difficult to detect due to their low luminosities. Highlighting the low mass galaxies at high redshifts is important for understanding the formation of the early universe. So far many efforts have been made to measure low redshift galaxies and high redshift QSOs and other AGNs. However, observing high redshift galaxies is a difficult task as it requires lots of telescope time and powerful telescopes

CHAPTER 5

to observe faint objects. The reasons above are why the MgII method has the potential to be a powerful tool for cosmology. I will now outline the findings in this thesis and conclude with future plans for the MgII method.

In all but one of the selected target clusters/superclusters, there was a detection made in MgII. The exception was for the first target which was found to have a null detection. Reasons for this were discussed such as the difficulty of observing structures at redshift $z = 1.1$ because of complications with sky lines as well as the reduced sensitivity in the SDSS spectrographs at this redshift. This being said, there was a strong arc of absorbers wrapping over the top of the small, central reference grid. Based on the results from the succeeding targets I now believe that the original S12 supercluster candidate documented at redshift $z = 1.12$ is located at a slightly different redshift. Also, the arc of absorbers wrapping over the top of the small reference grid may be another interesting structure, highlighting the cosmic web, but not actually in association with the S12 supercluster candidate at redshift $z = 1.12$. Photometric measurements are generally less accurate than spectroscopic measurements, meaning that it is feasible that S12 may have incorrectly calculated the central redshift of this particular structure. Targets 2, 3, 4, and 5 all made MgII detections believed to be in association with the target in question. Each detection led to further extension in MgII implying that the detected structures in the literature could be larger than is currently known. One example which demonstrates this point particularly well is Target 5. Here a dense arc of MgII absorbers was found stretching up to 1 Gpc and showing strong connectivity – the “Giant Arc”. Simple statistical tests were performed on the Giant Arc indicating up to 4.2σ significance. A structure of such size, and at a redshift where the universe is approximately half its age, raises some questions about the meaning of its existence in our current standard model of cosmology. Additionally, other questions can be asked such as: how did it form; how will it evolve; are there any other structures similar to the

CHAPTER 5

Giant Arc in length, connectivity and thinness; and does this structure challenge the standard model? A paper in preparation, Lopez et al. 2019, will aim to try and answer some of these questions, but firstly some improvements to the MgII method must be made and any shortcomings of the method must be noted.

When the MgII images are produced, the MgII absorbers along with the available background probes can be represented on the same image. However, the term “available background probes” is misleading as it can suggest that they are all the quasars in the background that have been searched for MgII absorption features in their spectra; this is not true. In fact, a number of background probes are missing since the QSO spectra that had no MgII absorption features in them were omitted from the MgII databases and only the QSOs with MgII absorption features in them were kept. Therefore the “available background probes” in the MgII images are in fact QSOs which at some point have at least one MgII absorption feature detected. This opens a few problems for the analysis of the MgII images. For example, flat-fielding the MgII absorbers based on the number of background probes is not truly represented if some of the potential background probes are omitted. Also, at times during the analysis of some structures, I mention the availability of background probes, either in the sense that the lack of background probes makes a structure interesting, or, the abundance of available background probes makes a structure less significant. As well, the same can be said for analysing voids in MgII, so if all of the potential available background probes were present and a void still appears then this can be more interesting and more useful for analysis. The shuffling software will benefit from the inclusion of all of the potential available background probes as well since the MgII absorbers would have greater shuffling potential. In general, including all of the inspected QSO spectra in the MgII databases will be useful in many aspects of MgII analysis. A new MgII database is in preparation, Clowes & Lopez 2019, which will include of all the QSO data as well as provide a

CHAPTER 5

third independent MgII database.

A shortcoming of the MgII method is that so far almost all of the analysis is done by eye or in some qualitative manner. For the purpose of this thesis, a qualitative assessment has provided a reasonable conclusion that MgII has the ability to detect the LSS. However, for further assessment, such as for the Giant Arc, an objective means of assessing the MgII images is necessary. Since the MgII absorbers in the images are fundamentally relying on the availability of background probes, simple minimal spanning tree (MST) algorithms, or Voronoi Tessellation (VT) cannot be applied in this case. However, the flat-fielding process in the software creates a MgII density image which has taken into account the density image of the background probes. That is, algorithms for detecting structures, filaments or dense regions, can be applied to the pixels in the images as opposed to the individual MgII absorbers. The filament-finder algorithms would have to account for minor gaps, and give priority to the pixels with high density values in them. In a study presented by Telfer et al. (2015) on detecting sand dunes on Mars, a filament-finder algorithm was used to automatically detect the lines in the sand dunes. A similar method could be adopted for the MgII images. Further to this, a method of detecting whether a MgII image should be tested for filaments or large, dense regions will be investigated as this will eliminate the need for subjective decisions.

The aim of this thesis was to assess the potential of intervening MgII absorbers in cosmology and so far I have showed that the potential for intervening MgII absorbers in LSS is promising. However, using intervening MgII absorbers is such a fast, effective method for observing LSS that it could be used to scan large areas of sky and use automated systems to flag MgII images with interesting or significant structures. Having the opportunity to observe LSS across approximately one third of the entire sky (SDSS footprint) up to redshifts $z \sim 2.2$ is a major advantage for moving forward in cosmology.

CHAPTER 5

In addition to observing LSS, the MgII method will be used to assess the correlation of secondary perturbations of CMB temperature to regions of high and low density in the LSS via the Integrated Sachs-Wolfe (ISW) effect. Work such as this has already been explored, see for example Fosalba et al. (2003), Granett et al. (2008) and Szapudi et al. (2015).

I have shown that using intervening MgII absorbers can be used to highlight LSS in the universe. Additionally, I mention how MgII could be used in cosmology such as finding correlations between LSS and the CMB and running large sky surveys to flag other significant structures that exist in the universe. The current shortcomings of the MgII method as it stands now have been noted and suggested improvements have been made. In addition, I have presented one particular, serendipitous finding – the Giant Arc in the sky – which raises some important questions for cosmology and which will be published in a paper to follow, Lopez et al. 2019.

Bibliography

- Alonso, M. V., Coldwell, G. V., Söchting, I., et al. 2008, *Mon. Not. Roy. Astron. Soc.*, 385, 2254
- Balázs, L. G., Bagoly, Z., Hakkila, J. E., et al. 2015, *Mon. Not. Roy. Astron. Soc.*, 452, 2236
- Baldry, I. K., Robotham, A. S. G., Hill, D. T., et al. 2010, *Mon. Not. Roy. Astron. Soc.*, 404, 86
- Barnes, L. A., Garel, T., & Kacprzak, G. G. 2014, *Pub. Astron. Soc. Pac.*, 126, 969
- Bates, B., Bradley, D. J., McKeith, C. D., et al. 1970, in IAU Symposium, Vol. 36, Ultraviolet Stellar Spectra and Related Ground-Based Observations, ed. R. Muller, L. Houziaux, & H. E. Butler, 274
- Bertin, E. & Arnouts, S. 1996, *Astron. Astrophys. Suppl.*, 117, 393
- Burenin, R. A. 2017, *Astron. Letters* , 43, 507
- Burenin, R. A., Bikmaev, I. F., Khamitov, I. M., et al. 2018, *Astron. Letters* , 44, 297
- Burke, B. E., Mountain, R. W., Harrison, D. C., et al. 1991, *IEEE Tans. Electron Devices* , 38, 1069

- Churchill, C. W., Kacprzak, G. G., & Steidel, C. C. 2005, in IAU Colloq. 199: Probing Galaxies through Quasar Absorption Lines, ed. P. Williams, C.-G. Shu, & B. Menard, 24–41
- Clowes, R. G. & Campusano, L. E. 1991, *Mon. Not. Roy. Astron. Soc.*, 249, 218
- Clowes, R. G., Campusano, L. E., Graham, M. J., & Söchting, I. K. 2012, *Mon. Not. Roy. Astron. Soc.*, 419, 556
- Clowes, R. G., Harris, K. A., Raghunathan, S., et al. 2013, *Mon. Not. Roy. Astron. Soc.*, 429, 2910
- Codoreanu, A., Ryan-Weber, E. V., Crighton, N. H. M., et al. 2017, *Mon. Not. Roy. Astron. Soc.*, 472, 1023
- Crampton, D., Cowley, A. P., & Hartwick, F. D. A. 1987, *Astrophys. J.*, 314, 129
- Crampton, D., Cowley, A. P., & Hartwick, F. D. A. 1989, *Astrophys. J.*, 345, 59
- Dutta, R., Srianand, R., Gupta, N., & Joshi, R. 2017, *Mon. Not. Roy. Astron. Soc.*, 468, 1029
- Einasto, M., Liivamägi, L. J., Tago, E., et al. 2011, *Astron. Astrophys.*, 532, A5
- Evans, J. L., Churchill, C. W., Murphy, M. T., Nielsen, N. M., & Klimek, E. S. 2013, *Astrophys. J.*, 768, 3
- Faber, S. M., Phillips, A. C., Kibrick, R. I., et al. 2003, in Society of Photo-Optical Instrumentation Engineers (SPIE) Conference Series, Vol. 4841, *Proc. SPIE Int. Soc. Opt. Eng.*, ed. M. Iye & A. F. M. Moorwood, 1657–1669
- Fernández-Soto, A., Lanzetta, K. M., Chen, H.-W., Pascarelle, S. M., & Yahata, N. 2001, *Astrophys. J. Supple.*, 135, 41

- Fosalba, P., Gaztañaga, E., & Castander, F. J. 2003, *Astrophys. J. Letters*, 597, L89
- Gal, R. R., Lemaux, B. C., Lubin, L. M., Kocevski, D., & Squires, G. K. 2008, *Astrophys. J.*, 684, 933
- Gal, R. R. & Lubin, L. M. 2004, *Astrophys. J. Letters*, 607, L1
- Gal, R. R., Lubin, L. M., & Squires, G. K. 2005, *Astron. J.*, 129, 1827
- Gonçalves, R. S., Carvalho, G. C., Bengaly, C. A. P., Carvalho, J. C., & Alcaniz, J. S. 2018, *Mon. Not. Roy. Astron. Soc.*, 481, 5270
- Gott, III, J. R., Jurić, M., Schlegel, D., et al. 2005, *Astrophys. J.*, 624, 463
- Granett, B. R., Neyrinck, M. C., & Szapudi, I. 2008, *Astrophys. J. Letters*, 683, L99
- Gunn, J. E., Hoessel, J. G., & Oke, J. B. 1986, *Astrophys. J.*, 306, 30
- Guzzo, L., Cassata, P., Finoguenov, A., et al. 2007, *Astrophys. J. Supple.*, 172, 254
- Haines, C. P., Campusano, L. E., & Clowes, R. G. 2004, *Astron. Astrophys.*, 421, 157
- Haines, C. P., Clowes, R. G., Campusano, L. E., & Adamson, A. J. 2001, *Mon. Not. Roy. Astron. Soc.*, 323, 688
- Harwit, M. 2006, *Astrophysical Concepts*, Fourth Edition (Springer)
- Hewett, P. C. & Wild, V. 2010, *Mon. Not. Roy. Astron. Soc.*, 405, 2302
- Hill, G. J. & Lilly, S. J. 1991, *Astrophys. J.*, 367, 1
- Ilbert, O., Capak, P., Salvato, M., et al. 2009, *Astrophys. J.*, 690, 1236

- Iovino, A., Petropoulou, V., Scodreggio, M., et al. 2016, *Astron. Astrophys.*, 592, A78
- Iovino, A. & Shaver, P. 1988, in Pub. A.S.P. Conf. Series, No. 2, Vol. 2, Proc. Workshop on Optical Surveys for Quasars (*Pub. Astron. Soc. Pac.*)
- Kacprzak, G. G., Churchill, C. W., Steidel, C. C., & Murphy, M. T. 2008, *Astron. J.*, 135, 922
- Kells, W., Dressler, A., Sivaramakrishnan, A., et al. 1998, *Pub. Astron. Soc. Pac.*, 110, 1487
- Kocevski, D. D., Lubin, L. M., Gal, R., et al. 2009, *Astrophys. J.*, 690, 295
- Kochanek, C. S., Eisenstein, D. J., Cool, R. J., et al. 2012, *Astrophys. J. Supple.*, 200, 8
- Laurent, P., Le Goff, J.-M., Burtin, E., et al. 2016, *J. Cosmo. Astroparticle Phys.*
- Law, D. R., Cherinka, B., Yan, R., et al. 2016, *Astron. J.*, 152, 83
- Lubin, L. M., Brunner, R., Metzger, M. R., Postman, M., & Oke, J. B. 2000, *Astrophys. J. Letters*, 531, L5
- Lynch, R., Charlton, J., Kim, T. S., & Carswell, R. 2004, in *American Astron. Soc. Meeting Abstracts*, Vol. 205, 145
- Massey, P. & Foltz, C. B. 2000, *Pub. Astron. Soc. Pac.*, 112, 566
- Massey, P., Gronwall, C., & Pilachowski, C. A. 1990, *Pub. Astron. Soc. Pac.*, 102, 1046
- Maxfield, L., Spinrad, H., Stern, D., Dey, A., & Dickinson, M. 2002, *Astron. J.*, 123, 2321

- Nakata, F., Kodama, T., Shimasaku, K., et al. 2005, *Mon. Not. Roy. Astron. Soc.*, 357, 1357
- Ntelis, P., Hamilton, J.-C., Le Goff, J.-M., et al. 2017, *J. Cosmo. Astroparticle Phys.*, 2017, 019
- Ohta, K., Akiyama, M., Ueda, Y., et al. 2003, *Astrophys. J.*, 598, 210
- Oke, J. B., Cohen, J. G., Carr, M., et al. 1995, *Pub. Astron. Soc. Pac.*, 107, 375
- Oke, J. B., Postman, M., & Lubin, L. M. 1998, *Astron. J.*, 116, 549
- Pâris, I., Petitjean, P., Aubourg, É., et al. 2018, *Astron. Astrophys.*, 613, A51
- Pâris, I., Petitjean, P., Ross, N. P., et al. 2017, *Astron. Astrophys.*, 597, A79
- Pilachowski, C. A., Africano, J. L., Goodrich, B. D., & Binkert, W. S. 1989, *Pub. Astron. Soc. Pac.*, 101, 707
- Planck Collaboration, Ade, P. A. R., Aghanim, N., et al. 2016, *Astron. Astrophys.*, 594, A27
- Postman, M., Lubin, L. M., & Oke, J. B. 1998, *Astron. J.*, 116, 560
- R Core Team. 2019, R: A Language and Environment for Statistical Computing, R Foundation for Statistical Computing, Vienna, Austria
- Raghunathan, S., Clowes, R. G., Campusano, L. E., et al. 2016, *Mon. Not. Roy. Astron. Soc.*, 463, 2640
- Rosati, P., Stanford, S. A., Eisenhardt, P. R., et al. 1999, *Astron. J.*, 118, 76
- Sarkar, P., Yadav, J., Pandey, B., & Bharadwaj, S. 2009, *Mon. Not. Roy. Astron. Soc.*, 399, L128
- Schneider, D. P., Richards, G. T., Hall, P. B., et al. 2010, *Astron. J.*, 139, 2360

- Scoville, N., Aussel, H., Benson, A., et al. 2007, *Astrophys. J. Supple.*, 172, 150
- Shanks, T., Boyle, B. J., & Peterson, B. A. 1988, in Pub. A.S.P. Conf. Series, Vol. 2, *Proc. Workshop on Optical Surveys for Quasars*
- Söchting, I. K., Coldwell, G. V., Clowes, R. G., Campusano, L. E., & Graham, M. J. 2012, *Mon. Not. Roy. Astron. Soc.*, 423, 2436
- Spitzer, L. 1978, *Physical Processes in the Interstellar Medium*
- Stanford, S. A., Elston, R., Eisenhardt, P. R., et al. 1997, *Astron. J.*, 114, 2232
- Steidel, C. C. & Sargent, W. L. W. 1992, *Astrophys. J. Supple.*, 80, 1
- Szapudi, I., Kovács, A., Granett, B. R., et al. 2015, *Mon. Not. Roy. Astron. Soc.*, 450, 288
- Tanaka, I., Yamada, T., Aragón-Salamanca, A., et al. 2000, *Astrophys. J.*, 528, 123
- Tanaka, I., Yamada, T., Turner, E. L., & Suto, Y. 2001, *Astrophys. J.*, 547, 521
- Taylor, M. B. 2005, in *Astronomical Society of the Pacific Conference Series*, Vol. 347, *Astronomical Data Analysis Software and Systems XIV*, ed. P. Shopbell, M. Britton, & R. Ebert, 29
- Telfer, M. W., Fyfe, R. M., & Lewin, S. 2015, *Aeolian Research*, 19, 215
- Tennyson, J. 2005, *Astronomical Spectroscopy* (Imperial College Press)
- Ueda, Y., Akiyama, M., Ohta, K., & Miyaji, T. 2003, *Astrophys. J.*, 598, 886
- Ueda, Y., Takahashi, T., Inoue, H., et al. 1999, *Astrophys. J.*, 518, 656
- Williger, G. M., Campusano, L. E., Clowes, R. G., & Graham, M. J. 2002, *Astrophys. J.*, 578, 708

- Yadav, J., Bharadwaj, S., Pandey, B., & Seshadri, T. R. 2005, *Mon. Not. Roy. Astron. Soc.*, 364, 601
- Yadav, J. K., Bagla, J. S., & Khandai, N. 2010, *Mon. Not. Roy. Astron. Soc.*, 405, 2009
- Yamada, T., Tanaka, I., Aragón-Salamanca, A., et al. 1997, *Astrophys. J. Letters*, 487, L125
- Yee, H. K. C., Morris, S. L., Lin, H., et al. 2000, *Astrophys. J. Supple.*, 129, 475
- Zhu, G. & Ménard, B. 2013, *Astrophys. J.*, 770, 130